UNIVERSITY OF CALIFORNIA
SANTA CRUZ

GAS RETENTION AND ACCUMULATION IN STELLAR CLUSTERS AND GALAXIES: IMPLICATIONS FOR STAR FORMATION AND BLACK HOLE ACCRETION

A dissertation submitted in partial satisfaction of the
requirements for the degree of

Doctor of Philosophy

in

ASTRONOMY & ASTROPHYSICS

by

Jill Naiman

June 2014

The Dissertation of Jill Naiman
is approved:

_____
Professor Enrico Ramirez-Ruiz, Chair

_____
Professor Douglas N. C. Lin

_____
Professor Elena D'Onghia

_____
Dean Tyrus Miller
Vice Provost and Dean of Graduate Studies

Table of Contents

List of Figures

List of Tables

Abstract

Gas Retention and Accumulation in Stellar Clusters and Galaxies: Implications for Star Formation and Black Hole Accretion

by

Jill Naiman

Star formation cannot proceed without the existence of an extensive gas reservoir. In particular, the supply of gas to form stars in dwarf galaxies and star clusters requires overcoming a variety of difficulties - namely, the effectiveness of different feedback mechanisms in removing gas from these shallow gravitational potentials. In addition, the supply of external gas to these systems is determined by the large scale galactic structure in which they reside. This thesis employs computational hydrodynamics coupled with physically realistic subgrid feedback prescriptions to resolve the interplay between the small scale feedback mechanisms and larger scale gas flows to determine the amount of gas a shallow potential can accumulate.

First, we consider the flow of gas external to dwarf galaxies and star clusters into their cores as a generalized accretion process. Second, we explore the enhancement of gas accretion rates onto the compact members of young star clusters when the flow of external gas into the cluster cores is large. Third, we discuss how external gas flows initiated by the presence of a massive nuclear star cluster can enhance central massive black hole accretion rates during galaxy mergers. Fourth, we change our focus to exploring internal stellar wind retention in proto-globular clusters as a mechanism to supply gas for multiple episodes of star formation.

Finally, the implications of stellar wind retention on the current gas reservoir in globular clusters is discussed.

To my mother and father, who instilled in me the importance of dedication and hard work when pursuing your passions.

But also, that sometimes its best to wing it.

Acknowledgments

My graduate career would never have blossomed into the great future career opportunities I have without the enthusiastic advisement of Enrico Ramirez-Ruiz and the wisdom of Douglas Lin. In addition, the mentorship of Elena D'Onghia, Rebecca Bernstein and Chung-Pei Ma have created a fantastically supportive environment for me during my graduate studies.

I am ever thankful for Enrico's advise in matters of both science and public outreach. His enthusiasm for scientific inquiry and connecting underrepresented populations with science motivated me to be a better person in both realms. His ability to meet any hurdles I might face on the often parlous path of graduate school with a touch of grace and good sense of humor was greatly appreciated in some of the tougher moments.

I would also like to thank the incredible undergraduate students I've had the opportunity to work with while at UC Santa Cruz. Ricky Fernandez, Melinda Soares, and Andrea Derdzinski in particular continue to astound me with their scientific prowess and impressive ability to learn. It has been a truly humbling experience to mentor these students during my graduate career.

In addition, my fellow graduate students are a constant source of inspiration. The friendships of my colleagues Morgan MacCleod, Jennifer Burt, Katie Hamren, Angie Wolfgang, Rachel Strickler, and Laurel Ruhlen constantly remind me of the privilege I have of getting to go to work everyday with some of the most intelligent people I've ever met.

The support of my parents throughout my undergraduate and graduate education has been phenomenal. Their belief that their child will be able to figure out any problem put in front

of her, while perhaps occasionally misguided (for example, paying bills on time), has always motivated me to do my best.

Finally, I would like to thank my friends. Amanda provided much excitement and comic relief during the scary start of my graduate career. Alicia fed my need for perspective from the vantage point of her "real job." Matt, Jacques and Badier where gracious ambassadors of all things nerdy. In addition, to the friends I have had for nearly two decades (proving our senses of humor have not changed much since age 10) - Alisa, Bev, Carly and Roxy there are simply no words other than thank you for your love and friendship.

The author of this thesis was the primary investigator and first author of all the research presented on the following pages, which are comprised of five publications to the Astrophysical Journal. The author was supported through the David and Lucille Packard Foundation, the NSF (PHY-0503584 and AST-0908807), Chancellor's Dissertation Year Fellowship, and the ARCS Fellowship.

Chapter 1

Introduction

Stars are the fundamental units of luminous matter in the universe, and they are responsible, directly or indirectly, for most of what we observe. They also serve as our primary tracers of structure formation and evolution of the universe and its constituents. Consequently, it is of central importance in astrophysics to understand how stars form and what determines their properties. Star formation occurs as a result of the influence of gravity on a wide range of scales and various physical mechanisms may be important at different scales, depending on the forces opposing gravity. On galactic scales, the tendency of interstellar matter to condense under gravity into star-forming clouds is intimately related to the rate at which gas is supplied. The aim of my research has been focused on understanding the mass supply conditions required for triggering star formation, with emphasis on processes occurring at large scales in both galaxies and star clusters.

Some important aspects of star formation that are not yet fully understood include the coupling of large galactic scale gas flows with small scale star formation processes to even

smaller scales where heating and cooling dictate the evolution of the gas flow. Typical stellar masses may be determined by the average cloud properties, such as the temperature and density that control the mass required for collapse, but understanding the conditions necessary for gas to flow from large to small scales is key for determining the rate at which stars are formed. For this reason, the triggering of star formation provides a challenge for simulations that endeavor to include all of the relevant physics. Existing cosmological models are able to resolve galactic scale mass flows, but are unable to accurately resolve how the gas interacts and is modified by galactic substructures. This is an area where there is plenty of room for breakthroughs.

The problem of effective gas supply required for the formation of stars in stellar clusters and dwarf galaxies remains unsolved. This is because the properties of the gas surrounding these systems is determined by the large scale galactic structure in which they reside. In this thesis both analytical and computational techniques are used to show how such weakly bound gravitational structures might be able to accumulate gas effectively and form new generations of stars. It is not presently clear either observationally or theoretically whether there is a firm lower limit to the size of a star cluster or dwarf galaxy within which stars can form. Thus, further study of these processes may have long-lasting implications in galaxy evolution and globular cluster assembly.

In addition, the effects of large density enhancements in these weakly bound gravitational structures on the accretion rates of their compact stellar members will be addressed. Accretion onto black holes is responsible for some of the highest energy phenomena currently observed. In particular, active galactic nuclei, powered by accretion onto massive black holes, provide windows into galaxy formation at high redshift. The augmentation of the mass accre-

tion rates onto the theorized intermediate mass black holes thought to inhabit star clusters would have significant implications for their observability.

In Chapter 2 we consider the supply of material into cluster and dwarf galaxy potentials from the external medium as a generalized accretion process. Accretion studies have been focused on the flow around bodies with point mass gravitational potentials, but few general results are available for non-point mass distributions. Here, we study the accretion flow onto non-divergent, core potentials moving through a background medium. We use Plummer and Hernquist potentials as examples to study gas accretion onto star clusters, dwarf and large galaxy halos and galaxy clusters in a variety of astrophysical environments. The general conditions required for a core potential to collectively accrete large quantities of gas from the external medium are derived using both simulations and analytic results. We briefly discuss the consequences of large mass accumulation in galaxy nuclei, dwarf galaxies, and star clusters. First, if the gas cools effectively star formation can be triggered, generating new stellar members in the system. Second, if the collective potential of the system is able to alter the ambient gas properties before the gas is accreted onto the individual core members, the augmented mass supply rates could significantly alter the state of the various accreting stellar populations and result in an enhanced central black hole accretion luminosity.

In Chapter 3 we focus on one of the examples presented in Chapter 2 - the implications that large density enhancements in clusters have on the accretion rates of their compact members. Here, it is demonstrated that the overabundance of ultra-luminous, compact X-ray sources (ULXs) associated with moderately young clusters in interacting galaxies such as the Antennae and Cartwheel can be given an alternative explanation that does not involve the pres-

ence of intermediate mass black holes (IMBHs). It is argued that gas density within these systems is enhanced by the collective potential of the cluster prior to being accreted onto the individual cluster members and, as a result, the aggregate X-ray luminosity arising from the core of neutron star cluster members can exceed $> 10^{39}$ ergs^{-1}. Various observational tests to distinguish between IMBHs and accreting neutron star cusps are discussed.

In Chapter 4 I discuss the augmentation to the mass accretion rate of massive black holes during galaxy mergers when they are surrounded by a nuclear star cluster. In galaxy mergers, the gas falls to the center, triggers star formation, and feeds the rapid growth of supermassive black holes (SMBHs). SMBHs respond to this fueling by supplying energy back to the ambient gas. Numerical studies suggest that this feedback is necessary to explain why the properties of SMBHs and the formation of bulges are closely related. This intimate link between the SMBH's mass and the large scale dynamics and luminosity has proven to be a difficult issue to tackle with simulations due to the inability to resolve all the relevant length scales simultaneously. In this Chapter SMBH growth is simulated at high resolution, accounting for the gravitational focusing effects of nuclear star clusters (NSCs), which appear to be ubiquitous in galactic nuclei. We discuss the conditions required for effective gas funneling to occur, and provide a sub-grid prescription for the augmentation of central SMBH accretion rates in the presence of NSCs. For the conditions expected to persist in the centers of merging galaxies, the resultant large central gas densities in NSCs should produce drastically enhanced accretion rates onto the embedded SMBHs. This will naturally result in faster black hole growth rates and higher luminosities than predicted by the commonly used Bondi-Hoyle-Lyttleton accretion formalism.

In Chapter 5 we change gears and focus on gas supply in shallow potentials, specifically star clusters, by the stellar winds of the cluster members. We first focus on the effects of stellar wind retention in proto-globular clusters and the implications for multiple episodes of star formation in these systems. The discovery of multiple evolutionary sequences has challenged the paradigm that globular clusters (GCs) host simple stellar populations. In addition, spectroscopic studies of GCs show a spread in light-element abundances, suggesting that multiple sequences can be formed from gaseous ejecta processed in evolved cluster stars. If multiple sequences originate from within GCs, then it should be determined how such stellar systems retain gas, form new stars within them and subsequently evolve. Here we expand upon previous studies and carry out hydrodynamical simulations that explore a wide range of cluster masses, compactness, metallicities and stellar age combinations in order to determine the ideal conditions for gas retention. We find that up to 9% of the mass of the original star cluster can be made up of retained stellar wind gas at the time star formation is triggered. However, we show that multiple episodes of star formation can take place during the lifetime of a star cluster in particular for times $\gtrsim 0.4$ Gyr when the stellar wind mass and energy injection rates are conducive to mass retention, thus leading to a sizable enhancement in the total number of new stars. The fact that this favorable star formation time interval coincides with the asymptotic giant branch (AGB) phase seems to give further credence to the idea that, at least in some GCs, there are stars which have formed from material processed by a previous generation of stars. The ability of extended heating sources, such as pulsar outflows or accretion onto compact objects, to hamper gas retention is illustrated via a simple numerical treatment.

In Chapter 6 the stellar wind formalism is extended to investigate the amount of gas

currently expected to reside in globular clusters. In particular, I employ hydrodynamical simulations to investigate the underlying mechanism responsible for the low levels of gas and dust in globular clusters. Our models examine the competing effects of mass supply from the evolved stellar population and energy injection from the main sequence stellar members for globular clusters 47 Tucanae, M15, NGC 6440, and NGC 6752. Disregarding all other gas evacuation processes, we find that the energy output from the main sequence stellar population alone is capable of effectively clearing the evolved stellar ejecta and producing intracluster gas densities consistent with current observational constraints. This result distinguishes a viable ubiquitous gas and dust evacuation mechanism for globular clusters. In addition, we extend our analysis to probe the efficiency of pulsar wind feedback in globular clusters. The detection of intracluster ionized gas in cluster 47 Tucanae allows us to place particularly strict limits on pulsar wind thermalization efficiency, which must be extremely low in the cluster's core in order to be in accordance with the observed density constraints.

Chapter 2

External Mass Accumulation onto Core Potentials: Implications for Star Clusters, Galaxies and Galaxy Clusters

2.1 Introduction

The process by which stars gravitationally capture ambient matter is called accretion. Calculations of the accretion flow onto stars are, in general, very difficult. First, one must determine the flow geometry; in general, if the gas possesses intrinsic angular momentum, it will be multidimensional depending upon the flow symmetry. Second, one must enumerate the dominant heating and cooling mechanisms that characterize the accreting plasma. If the gas is optically thick to the emitted radiation, the net cooling and heating rates will depend on the radiation field. Third, the effect of radiation pressure in holding back the flow must be properly accounted for. Fourth, one must understand the flow boundary conditions, both at

large distances and at the surface of the accretor. Fifth, the possible role of magnetic fields in the plasma must be assessed. So, it is not surprising that the problem of gas accretion onto stars has been solved in only a few idealized cases. In spite of the difficulties, significant progress has been achieved in understanding accretion flows by means of such idealized solutions.

The problem of accretion of gas by a star in relative motion with respect to the gas was first considered by Hoyle and Lyttleton (1939) and later by Bondi and Hoyle (1944) (BHL accretion). The spherically symmetric case, when the accreting mass is at rest with respect to the ambient gas, was first studied by Bondi (1952) and is commonly referred to as *Bondi* accretion. This gives a reasonable approximation to the real situation of an isolated star accreting from the interstellar medium, provided that the angular momentum, magnetic field strength and bulk motion of the interstellar gas with respect to the star can be neglected. For other types of accretion flows, such as those in close binary systems, spherical symmetry is rarely a good approximation. Nonetheless, the spherical accretion problem is of great relevance for the theory, as it introduces some key concepts which have much broader validity. What is more, it is possible to give a fairly exact treatment, allowing us to gain insight into more complicated situations.

Accretion studies have been focused on the flow around bodies with point mass gravitational potentials, but few general results are available for non-point mass distributions. Mass models with tractable potentials may accurately approximate the potentials of galaxies, galaxy clusters and dense stellar systems. Here, we consider calculations of the gas flow onto these smooth core potentials. We are interested in determining the amount of mass accumulation for core potentials with a range of velocities relative to the ambient gas. In §2, we briefly recapit-

ulate the relevant equations which describe the gas structure and deduce analytically the conditions for generalized core potentials to accumulate gas collectively. Because the gas structure is multi-dimensional in nature, we adopt a numerical approach to verify our analytic solutions. We describe the numerical scheme and the range of model parameters in §3, and the results of these calculations in §4. These results are applied, in §5, to study the accumulation of gas into dense stellar systems, galaxies and galaxy clusters moving in a variety of environments. In §6, we summarize our results and discuss their implications.

2.2 Mass Accumulation in a Cluster Core Potential

2.2.1 Generalized Solutions

Much of the effort herein will be dedicated to understanding the conditions by which smooth core potentials are able to accrete surrounding gas with highly enhanced rates. In particular, we would like to understand under which conditions a stable density enhancement will persist within a given potential well and derive a relation between the gas relative velocity, the local sound speed and the the central velocity dispersion of the cluster potential, which can be carried over quite generally to more complicated accretion flows.

To treat the problem mathematically we proceed as in Lin and Murray (2007). We take spherical polar coordinates with origin at the center of the potential. In spherical symmetry, the fluid variables are independent of angle and the gas velocity u has only a radial component.

For a steady flow, the continuity equation reduces to

$$r^2 \rho u = \text{constant}. \tag{2.1}$$

This constant is commonly denoted to as $\dot{M}$, and refers to a mass inflow (outflow) rate. In the Euler equation the only contribution to the external force comes from gravity and this has only a radial component

$$u\frac{du}{dr} + \frac{1}{\rho}\frac{dP}{dr} + \frac{d\phi}{dr} = 0. \tag{2.2}$$

Hence, the term $(1/\rho)(\frac{dP}{dr})$ is $(c_s^2/\rho)(d\rho/dr)$, where c_s is the sound speed. We replace the energy equation by the polytropic relation

$$P = K\rho^{\gamma}, \quad K = \text{constant}. \tag{2.3}$$

In this case: $c_s^2 = dP/d\rho = K\gamma\rho^{\gamma-1}$. This allows us to approximately treat both adiabatic ($\gamma = 5/3$) and isothermal ($\gamma = 1$) gas flows. After the solution has been found, the adiabatic or isothermal assumption should be justified by consideration of the particular radiative cooling and heating of the gas.

The gravitational potential of dense stellar systems, galaxies and galaxy clusters can be accurately described by smooth core potentials with

$$\phi(r) = -\frac{\phi_0}{\left(r^{\beta} + \varpi_c^{\beta}\right)^{\alpha}} = -\frac{\phi_0}{\zeta(r)}, \tag{2.4}$$

where ϖ_c is the radius of the core. The potential's core scale is given by

$$\zeta(r) = \left(r^{\beta} + \varpi_c^{\beta}\right)^{\alpha} \tag{2.5}$$

Cores potentials described by (2.4) are non-divergent, so that $\phi(r \mapsto 0) = \text{constant}$. This property, as we will show, allows core potentials to sustain subsonic inflow and collect ambient gas into a quasistatic envelope.

An estimate of the radial density distribution of collected ambient gas, $\rho(r)$, follows from the application of the conservation laws for energy and momentum. From equation (2.2) we have

$$\frac{u^2}{2} + \int \frac{dp}{\rho} + \phi = \frac{u^2}{2} + \frac{c_s^2}{\gamma - 1} + \phi = \text{const.} \tag{2.6}$$

Equation (2.6) makes use of the polytropic equation of state, where $dp = K\gamma\rho^{\gamma-1}d\rho$ and $c_s^2 = \gamma p/\rho = K\gamma\rho^{\gamma-1}$. Here, the limits $\phi(r \mapsto \infty) = 0$ and $u(r \mapsto \infty) = 0$ help determine the constant

$$\frac{u^2}{2} + \frac{c_s^2}{\gamma - 1} + \phi = \frac{c_\infty^2}{\gamma - 1}. \tag{2.7}$$

Dividing equation (2.7) by c_s^2 and making use of $c_s^2/c_\infty^2 = \rho^{\gamma-1}/\rho_\infty^{\gamma-1}$, one recovers a modified form of the Bernoulli equation in Bondi (1952)

$$\frac{1}{2}\frac{u^2}{c_s^2} + \frac{1}{\gamma - 1}\left[1 - \left(\frac{\rho_\infty}{\rho}\right)^{\gamma-1}\right] = -\frac{\phi}{c_\infty^2}\left(\frac{\rho}{\rho_\infty}\right)^{\gamma-1} \tag{2.8}$$

The isothermal version of the Bernoulli equation can be derived from equation (2.6) using

$dp = Kd\rho$ and $c_s = c_\infty$,

$$\frac{1}{2}\frac{u^2}{c_s^2} + \log\rho + \frac{\phi}{c_\infty^2} = \log\rho_\infty. \tag{2.9}$$

Together with knowledge of the radial velocity profile, equation (2.8) allows one to determine $\rho(r)$. For subsonic inflow $u^2(r)/c_s^2 \ll 1$, the ambient gas collects into a a *quasistatic* envelope with a density distribution given by

$$\rho(r) \approx \rho_\infty \left[1 + \frac{(\gamma-1)\phi_0}{c_\infty^2 \zeta(r)}\right]^{\frac{1}{\gamma-1}}, \tag{2.10}$$

where ρ_∞ is the density of the ambient medium. For an isothermal equation of state, this result is simply

$$\rho(r) = \rho_\infty \exp\left[\frac{\phi_0}{c_\infty^2 \zeta(r)}\right] \tag{2.11}$$

In §2.2.1.1, we derive under what conditions we can safely ignore the $u(r)^2/c_s^2$ term in equation (2.10).

2.2.1.1 Subsonic Flows in Core Potentials

We now consider the validity of the subsonic inflow assumption $|u(r)| < c_s$ used to derive equation (2.10) assuming subsonic flow at infinity, $|u_\infty| < c_\infty$. In spherically symmetry, the radial structure of the flow's velocity can be calculated by integrating (2.2) with the help of (2.3) and (2.1), so that

$$\frac{1}{2}\left(1 - \frac{c_s^2}{u^2}\right)\frac{d(u^2)}{dr} = \frac{1}{r}\left(2c_s^2 - r\frac{d\phi}{dr}\right) \tag{2.12}$$

At large distances from the potential the term $(2c_s^2 - r\frac{d\phi}{dr})$ on the right hand side of equation (2.12) must be positive since c_s^2 approaches c_∞^2 and $\phi \propto 1/r$, while r increases without limit. Given the that the inflow is initially subsonic, it will remain subsonic provided

$$c_s^2 > \frac{r}{2}\frac{d\phi}{dr} \tag{2.13}$$

for all r in the flow such that there is no transonic point.

Because c_s is a monotonically decreasing function of r, equation (2.13) is satisfied provided

$$c_\infty^2 > \frac{r}{2}\frac{d\phi}{dr}. \tag{2.14}$$

Consequently, condition (2.14) guarantees $|u(r)| < c_s$ throughout the gas flow.

Describing $\phi(r)$ as in equation (2.4), condition (2.14) can be rewritten as

$$c_\infty^2 > \frac{1}{2}\frac{\beta\alpha r^\beta \phi_0}{\left(r^\beta + \varpi_c^\beta\right)^{\alpha+1}}. \tag{2.15}$$

The right hand side of equation (2.15) has a maximum at

$$r = \left(\frac{\varpi_c}{\alpha}\right)^{1/\beta}, \tag{2.16}$$

so that condition (2.14) is satisfied for core potentials if

$$c_\infty^2 > \frac{\phi_0}{\varpi_c^{\beta\alpha}}\frac{\beta}{2}\left(\frac{\alpha}{\alpha+1}\right)^{\alpha+1}. \tag{2.17}$$

Notice that as $\varpi_c \mapsto 0$, the ambient gas is unable to collect into a quasistatic envelope and, as a result, the density structure of the flow is no longer accurately described by equation (2.10). In this limit, the potential essentially reduces to that of a point mass and the inflow rate can be derived following Bondi (1952).

2.2.1.2 Mass Accumulation in Non-Stationary Core Potentials

The density structure of ambient gas collecting into a core potential in the case that the gravitational structure is collecting gas isotropically is described by equation (2.10). If the potential is moving with some velocity with respect to the ambient medium, one expects the build up of a stable density enhancement to be inhibited. A characterization of this impedance on the growth of the central density enhancement is derived here by comparing the pressure support due to the collected ambient gas to that provided by the ram pressure. The radius at which these two pressures are equal defines a *characteristic radius*, which we denote here as r_s. A schematic diagram illustrating the geometry of the flow around non-stationary core potentials, together with a sketch of the expected sound speed and density profiles of the collected ambient material, is given in Figure 6.1.

The characteristic radius, r_s, is calculated here under the assumption that a stable density enhancement has been established, whose radial profile is well described by equation (2.10). The potential, together with its collected ambient gas, is then assumed to move with a constant velocity, $u_{const} \approx u_\infty = \mu_\infty c_\infty$. This provides a reasonable approximation provided that the flow variables across the shock region are accurately described in terms of their limiting values (i.e. the incoming flow is not significantly altered by the gravitational potential and

therefore the interior flow preserves its static solution). When this high velocity gas hits the stationary ambient medium, a bow shock forms. In the frame moving with the shock, the density jump condition can be written as

$$\frac{\rho_\mu}{\rho_\infty} = \frac{(\gamma+1)\mu_\infty^2}{(\gamma+1)+(\gamma-1)(\mu_\infty^2-1)} \tag{2.18}$$

where $\rho_\mu = \rho(r)$, with $\rho(r)$ given by equation (2.10). Equation (2.18) assumes the adiabatic index γ is the same for the post and pre-shock gas. The jump conditions across the shocked region yield

$$\zeta(r_s) = \frac{\phi_0(\gamma-1)}{c_\infty^2}\left[\left\{\frac{(\gamma+1)\mu_\infty^2}{2+(\gamma-1)\mu_\infty^2}\right\}^{\gamma-1} - 1\right]^{-1} \tag{2.19}$$

where we have used $\zeta(r_s) = (r_s^\beta + \varpi_c^\beta)^\alpha$. These standoff distance define the *characteristic radius* of the bow shock. For $\phi_0 \propto M$ we have $\alpha \cdot \beta = 1$, so that

$$\zeta(r_s = \varpi_c) \equiv 2^{1/\alpha}\varpi_c. \tag{2.20}$$

Equation (2.19) can be rewritten for an isothermal equation of state as

$$\zeta = \frac{\phi_0}{c_\infty^2}\frac{1}{\log\mu_\infty^2} \quad \text{for} \quad \gamma \to 1. \tag{2.21}$$

In general, core potentials moving at high velocities have density enhancements and characteristic radii that decrease with increasing velocity. At sufficiently high Mach numbers, one expects the incoming flow's ram pressure to overcome the central pressure due to the col-

lected ambient gas and to penetrate into the potential's core. The transition between a stable density enhancement and an unsupported, supersonic inflow occurs roughly when $r_s \approx \varpi_c$. When $r_s \leq \varpi_c$, the ability of the core to sustain a stable density enhancement is lost. For this reason, we expect rapidly moving potentials to have smaller density enhancements than those predicted by equation (2.10). In these cases our formalism inherently overestimates the internal pressure support against the inflowing ambient material, which in turn overestimates the characteristic radius. The detailed behavior of the characteristic radius with adiabatic index, Mach number and gravitational potential type will be explored in §2.3 using numerical simulations. In the following numerical models, we will approximate isothermal equations of state by setting $\gamma = 1.01$. For consistent comparison, we will use equations (2.10) and (2.20) with $\gamma = 1.01$ in all plots unless otherwise noted.

2.2.2 Specific Core Potentials

Here, we focus our attention on the ability of stellar clusters, galaxies, and galaxy clusters to collect ambient material. Stellar clusters can be accurately described by Plummer potentials (Brüns *et al.*, 2009a; Pflamm-Altenburg and Kroupa, 2009)

$$\phi(r) = \frac{GM_p}{(r^2 + r_c^2)^{1/2}}, \tag{2.22}$$

where $M_{\rm p}$ is the mass of the potential and $r_{\rm c}$ is the commonly referred to as *core radius*. In this case, $\phi_0 = GM_{\rm p}$, $\varpi_{\rm c} = r_{\rm c}$, $\beta = 2$, and $\alpha = 1/2$, so that equation (2.10) can be rewritten as

$$\rho(r) = \rho_\infty \left[1 + \frac{GM_{\rm p}(\gamma-1)}{c_\infty^2 \left(r^2 + r_{\rm c}^2\right)^{1/2}}\right]^{\frac{1}{\gamma-1}} \tag{2.23}$$

Dark matter profiles of galaxies and galactic clusters are, on the other hand, commonly modeled by Hernquist (1990) potentials

$$\phi(r) = \frac{GM_{\rm h}}{r+a}, \tag{2.24}$$

where $M_{\rm h}$ is the mass of the potential and a is the scale length. In these cases, $\phi_0 = GM_{\rm h}$, $\varpi_c = a$, $\beta = 1$, and $\alpha = 1$, so that equation (2.10) becomes

$$\rho(r) = \rho_\infty \left[1 + \frac{GM_{\rm h}(\gamma-1)}{c_\infty^2 (r+a)}\right]^{\frac{1}{\gamma-1}} \tag{2.25}$$

In what follows, these two types of potentials are numerically modeled moving through ambient gas at rest to and compare to our analytic treatment.

2.3 Simulations of Mass Accumulation in Core Potentials

2.3.1 Numerical Method and Initial Model

To examine the ability of core potentials to collect ambient gas into a quasistatic envelope, we simulate core potentials moving through ambient gas with FLASH, a parallel,

adaptive mesh refinement hydrodynamics code. This scheme, and tests of the code are described in Fryxell *et al.* (2000a).

Common to all calculations is the placement of inflow boundaries to one side of our computational domain in order to simulate the motion of the core potential through the external medium. As a result, ambient gas moves to the right of our grid at a supersonic velocity. When this high velocity gas hits the stationary potential, a bow shock forms. All gravitational potentials are modeled here using a Plummer (2.22) or a Hernquist (2.24) functional form.

Simulations start with a uniform background density and run until a steady density enhancement is established inside the core's potential. This usually takes about 10-100 sound crossing times (Naiman *et al.*, 2009). Several models were run longer to test convergence and density enhancements were found to change only slightly with longer run times. We further tested convergence of our models for several resolutions and domain sizes. All tests produced similar density enhancements to those shown here. After hundreds of sound crossing times, the flow is relatively stable, and does not exhibit the *flip-flop* instability seen in two dimensional simulations (Blondin and Pope, 2009).

The effects of self gravity of the gas are ignored. This is adequate for most of our models, for which the accumulated mass is significantly less than the mass responsible for the potential. To improve the controlled nature of the models, and to facilitate comparison with our analytic estimates, we do not explicitly include radiative heating or cooling. As with our analytic estimates, we assume a polytropic equation of state $P \propto \rho^{\gamma}$. The effects of radiative equilibrium are approximated by having the gas evolve with an adiabatic constant $\gamma = 1.01$ (giving nearly isothermal behavior), while inefficient cooling is model here by having the gas

evolve with $\gamma = 5/3$.

2.3.2 General Properties of the Gas Flow

The classical Bondi treatment for non-divergent potentials, representative of star cluster and galactic gravitational potentials, is only a fair approximation far from the core when $GM_c/\varpi_c \gg c_\infty^2 + u_\infty^2$. When $GM_c/\varpi_c \lesssim c_\infty^2 + u_\infty^2$, the collective potential alters the local gas properties, allowing the core to sustain subsonic mass inflow and, as a result, collect ambient gas into a quasistatic envelope.

Figure 2.2 shows the resulting density structures of the collected ambient gas for a point mass and two different core potentials. To facilitate comparison, the Plummer and Hernquist potentials depicted in Figure 2.2 have been constructed to yield the same circular velocity peak radius: r_v. This requirement can be rewritten as

$$a = \sqrt{2} r_c, \tag{2.26}$$

which, by demanding the mass within this characteristic radial scale to be the same, gives

$$M_h = \frac{8}{3}\sqrt{\frac{2}{3}} M_p. \tag{2.27}$$

Hence, equations (2.23) and (2.25) give

$$\frac{\rho_h(r=0)}{\rho_p(r=0)} \approx \left(\frac{8}{3\sqrt{3}}\right)^{\frac{1}{\gamma-1}}, \tag{2.28}$$

where $\rho_{\max} \equiv \rho(r=0) \gg \rho_\infty$.

The flow pattern around a core potential is multi-dimensional and complex. In the frame of the potential, the gas streamlines are bent towards the cluster center. Some shall intersect the center, while others converge along a line behind it. The convergence speed of the gas determines the reduction in its velocity relative to the potential due to shocks, and therefore whether or not the gas is accumulated in the core. As seen in Figure 2.2, the flow structure within the cluster markedly differ from the classical Bondi flow.

The properties of the core potential have a decisive effect on the radial profiles of the collected ambient gas. For $r \ll \varpi_c$ and $\rho_{\max} \gg \rho_\infty$, equation (2.10) gives

$$\frac{\rho(r)}{\rho_{\max}} \approx \left[1-\alpha\left(r/\varpi_c\right)^\beta\right]^{\frac{1}{\gamma-1}} \tag{2.29}$$

This shows that gas collected in potentials with steep core profiles have, as expected, sharper central density profiles. From equations (2.29) and (2.26), it follows that $\rho/\rho_{\max} \propto [1-(r/\sqrt{2}r_c)]^{\frac{1}{\gamma-1}}$ and $\rho/\rho_{\max} \propto [1-2(r/r_c)^2]^{\frac{1}{\gamma-1}}$ for Hernquist and Plummer potentials, respectively. Figure 2.2 shows that the the steeper Hernquist interior potential produces gas accumulation which is more centrally confined within its core than that in the Plummer potential.

At $r \gg \varpi_c$, the divergence of the gravitational potential naturally leads to a loss of pressure support against the incoming material. As a result, the characteristic radius, r_s, will be smaller for less extended (or less massive) core potentials. Inserting equation (2.27) into

equation (2.19) and making use of equation (2.20), one finds

$$\frac{\zeta(r_s = \varpi_c)_h}{\zeta(r_s = \varpi_c)_p} = \frac{8}{3\sqrt{3}} \tag{2.30}$$

for Hernquist and Plummer potentials yielding the same circular velocity peak radius, γ, μ_∞ and c_∞. Under these conditions, the ambient gas collected into a Hernquist potential at $r \gg \varpi_c$ will be comparatively denser and thus lead to an increase in pressure support against the incoming flow. This is mainly due to the comparatively larger mass (see equations (2.27) and (2.19)) together with the less divergent potential at large radii. This enhanced support forces the flow to move around the central density enhancement, thus leading to a widening of the standing bow shock. This is evident in Figure 2.3, which plots the bow shock patterns produced around a point mass (Ruffert, 1994b), Plummer and Hernquist potential set in motion through an initially uniform medium.

2.3.3 Mach Number Dependence

In line with the conventional treatment, potential cores moving with respect to the ambient medium at increasing supersonic velocities will have density enhancements that are progressively smaller and significantly more offset from the cluster's center. Figure 2.4 shows the resulting density and velocity flow structures generated around a point mass, Plummer and Hernquist potential moving through an initially uniform medium with $\mu_\infty \geq 1$. The differences in the flow structure are most notable when comparing the flow velocity structures depicted in Figure 2.4, which show that the central density enhancements in core potentials are quasi-static,

while those for the point mass are not. While there are regions of inflowing gas around core potentials, primarily behind the bow shock and downstream from the core's center, there are large central regions that experience no net inward gas flow.

A stable density enhancement is observed to persist as long as $\mu_\infty \lesssim 3$ (Figure 2.4). For larger relative velocities, the central gas pressure support is overwhelmed by the ram pressure of the incoming gas and, as a result, the bow shock begins to detach from the potential's core. The transition from a bow to a tail shock takes place at around $\mu_\infty \approx 3$. Note that in the case of a point mass potential with an arbitrarily small sink radius, the gravitational forces will always overwhelm the ram pressure at a finite radius. In this case, there is no transition to a tail shock (Wolfson, 1977). However, for core potentials (and point mass potentials with a finite sink size), the gravitational force approaches a constant value near the potential's center, thus allowing the formation of a tail shock.

As shown in Figure 2.5, the radial density profiles of the accumulated ambient gas, within a core potential differ from the classical Bondi profiles, and, for low Mach numbers, are accurately described by the quasistatic solutions derived in §2.2. These solutions fail to provide a good description of the density of the inflowing gas for $\mu_\infty \gg 1$. This is because these solutions were derived assuming a static ambient gas. The decrease of the characteristic radius and of the collected ambient gas density with increasing μ_∞ are clearly visible in the simulations. This decrease is connected with an increase of the ram pressure of the incoming material which, in turn, helps overcome the central pressure of the collected ambient gas.

2.3.4 Dependence on the Polytropic Index γ

The determination of the internal structure of gas flowing around gravitational potentials depends upon detailed knowledge of the equation of state. In §2.2, we have derived analytical solutions for the internal pressure and density structure of the flow in the cases in which the pressure depends solely upon the density through an equation of state of the form $P = K\rho^{\gamma}$.

The dependence of the overall gas density structure on the polytropic index γ is illustrated in Figures 2.6 and 2.7. By comparing the flow structures in Figures 2.6 and 2.7, one sees that ambient gas is in fact collected much more gradually when its pressure support increases adiabatically ($\gamma = 5/3$). From equation (2.10), it follows that $P \propto \zeta^{\frac{-\gamma}{\gamma-1}}$. Thus, gas accumulated in potentials with higher adiabatic indexes will be less centrally confined and, as a result, will be less effective at protecting the collected gas from being displaced by the inflowing material. By contrast, gas collected isothermally ($\gamma \approx 1$) into a core potential will be comparatively denser and thus lead to a significant increase in pressure support at small radii. This is consistent with the behavior observed in Figure 2.6, where decreasing γ moves the shock closer to the potential's core. Despite the initially less extended bow shock, the enhanced support provided by more compressible flows at small radii delays the transition to a tail shock as the relative velocity increases and, as a result, the bow shock radius decreases.

2.3.5 General Conditions Required for Large Density Enhancements

A core potential can sustain a large central density enhancement provided that $r_{\rm s} \gtrsim \varpi_{\rm c}$. This condition can be rewritten as $GM/\varpi_{\rm c} \gtrsim \left(c_{\infty}^2 + u_{\infty}^2\right) \equiv V^2$, or alternatively, as $\sigma_{\rm v} \gtrsim V$ where

σ_v is the velocity dispersion of the system.

In Figure 2.8 we examine the ability of a core potential to collect ambient gas as a function of the characteristic radius r_s. A density enhancement is observed to persist as long as $r_s \gtrsim \varpi_c$. Once $r_s < \varpi_c$, the collective potential is unable to alter the properties of the flow within $r \leq \varpi_c$.

In addition, the equation of state alters the compressional properties of the incoming flow. Isothermal flows, corresponding to $\gamma \approx 1$, allow for the effective build up of mass. Adiabatic gas, $\gamma = 5/3$, will instead rapidly heat the gas as it accumulates in the core, and halt the gas inflow at much lower central densities than for the $\gamma \approx 1$ case. Figure 2.9 compares the simulated density enhancements results with those predicted by equation (2.10).

2.3.6 Bow Shock Instabilities

Most shock instabilities identified and studied in astrophysics are related to the acceleration or deceleration of the shock itself (e.g. Bernstein & Book 1978, Vishniac 1983). By definition, stationary shocks are stable with respect to these mechanisms, but can still be unstable. Nakayama (1993) pointed out the radial instability of the shock if the flow is immediately accelerated after the shock transition, in isothermal flows. In this respect the shocked Bondi flow should be unstable. The validity of the postshock acceleration criterion for adiabatic flows is still uncertain, even for radial perturbations (Nakayama 1994). Independently of the sign of post-shock acceleration, Foglizzo & Tagger (2000) and Foglizzo (2001) revealed another generic instability mechanism based on the cycle of acoustic and vortical perturbations in the shock region.

The vortical-acoustic instability is fundamentally non-radial. In this case, both vorticity and entropy perturbations are advected from the shock to the accretor, and both are coupled to the acoustic perturbations. The most unstable cycle involves high frequency acoustic waves, those able to explore the hottest parts of the flow but still be refracted out, with a wavelength slightly larger than the smallest size of the sonic surface. In the isothermal limit ($\gamma \to 1$), where entropy perturbations are absent from the problem, vorticity is more appropriate than entropy to describe the advective-acoustic cycle.

The entropic-acoustic cycle is expected to be an efficient instability mechanism for $\gamma \approx 5/3$, provided $\mu_\infty \gtrsim 2$ and that the distance to the sonic surface (with depends on r_s) is small enough (Foglizzo et al. 2005). This coincides with our numerical simulations of core accretion which show strong instability when $r_s \approx \varpi_c$ (Figure 2.8). The lack of strong instability of adiabatic flows around core potentials with $r_s \gg \varpi_c$ could be due to the lack of effective acoustic feedback from the advected vorticity perturbation. Our numerical experiments also show the presence of instabilities within fast moving, isothermal flows. In particular isothermal flows appears much more unstable when $r_s \approx \varpi_c$ (Figure 2.6). In this conditions, a small pressure perturbation of the shock is able to generate vorticity perturbations very efficiently for $\gamma = 1$ strong shocks. The differences seen in the shock geometry between these two limiting cases precludes an accurate comparison of the stability of the flow, especially since the instability threshold is very sensitive to the size and shape of the sonic surface (Foglizzo et al. 2005).

2.4 Astrophysical Relevance

The ability of core potentials to collect ambient mass depends sensitively on their velocity dispersion, relative speed with respect to the ambient gas and gas cooling properties. Estimates of velocity dispersion and environmental gas properties are known for a wide range of systems, including star clusters, dwarf galaxies, large galactic halos, and clusters of galaxies. In what follows, we refine our calculations to include a wide variety of embedding media and discuss how environmental properties conspire to enable or disable the effective collection of surrounding mass in these systems. We assume the individual stellar members are accreting at low enough rates such that mass removal (and feedback) can be neglected. These results are summarized in Table 2.1.

2.4.1 Star Clusters

Star clusters are generally well described by Plummer potentials (Plummer, 1911; Brüns *et al.*, 2009a; Pflamm-Altenburg and Kroupa, 2009). In this section, we will discuss two limiting cases spanning the range of environments star clusters might inhabit. First, we discuss a compact star cluster moving slowly with respect to cold gas, representative of young clusters in a galaxy merger environment. This situation is simulated in Figure 2.10 (model A). Second, we model a less compact cluster moving quickly with respect to the background gas. These less favorable conditions for gas accumulation are simulated in Figure 2.10 (model B).

2.4.1.1 Young Star Clusters

Young massive star clusters are frequently found in merging systems like the Antennae and Cartwheel galaxies (Whitmore *et al.*, 1999a; Crivellari *et al.*, 2009). In the Antennae complex, for example, young (compact) star clusters are observed to move slowly with respect to the cold gas: $c_\infty \approx 10\,\mathrm{km\,s^{-1}}$ and $\mu_\infty \lesssim 2$ (Whitmore *et al.*, 1999a; Gilbert and Graham, 2007a). Observations in the infrared suggest large amounts of dust present in the gas (Brandl *et al.*, 2005a), which justifies an assumption of isothermal gas. A typical cluster, $M_\mathrm{p} = 3.5 \times 10^5\,M_\odot$, $\varpi_\mathrm{c} = r_\mathrm{c} = 1\,\mathrm{pc}$, in this cold, efficiently cooling gas ($\gamma = 1.01$), moving at $\mu_\infty = 2.0$ is shown in Figure 2.10 (model A). In these merging environments, conditions are ideal for accumulating large amounts of ambient gas in these systems as $r_\mathrm{s} \gg r_\mathrm{c}$. Taking $\rho_\infty \approx 10^{-22}\,\mathrm{g\,cm^{-1}}$, similar to that inferred by Zhu *et al.* (2003a), we find the collected mass to be a sizable fraction of the total cluster mass: $M_\mathrm{acc}/M_\mathrm{p} \approx 0.05$.

For these young clusters (< Gyr), one might worry about the applicability of our results, as feedback due to massive stellar winds is neglected in our treatment. We can estimate the magnitude of this effect by comparing the ram pressure from stellar winds of the cluster members to the pressure support generated by the collected ambient gas. The ram pressure due to expanding stellar winds is approximately given by $P_* = \rho_* v_*^2 = N\dot{M}_* v_*/(4\pi r^2)$ for N massive stars. Each star here is assumed to have a mass loss rate and wind velocity $\dot{M}_*$ and v_*, respectively, expanding into a spherical volume of radius r. We can then calculate the size of the wind bubble, r_w, by equating $P_*(r_\mathrm{w}) = P_\rho(r_\mathrm{w})$, where $P_\rho = c_\infty^2[\rho(r)]^\gamma/\gamma \approx c_\infty^2\langle\rho\rangle$, where $\langle\rho\rangle$ is the average density in the cluster's core. Solving for r_w gives $r_\mathrm{w} \approx 0.02 N_2^{1/2} \dot{M}_{*,-7}^{1/2} v_{*,3}^{1/2} \langle\rho\rangle_{-18}^{-1/2} c_{\infty,1}^{-1}$ pc,

where $N = 10^2 N_2$, $\dot{M}_* = 10^{-7} \dot{M}_{*,-7}\, M_\odot\ \mathrm{yr}^{-1}$, $v_* = 10^3\, v_{*,3}\ \mathrm{km\ s^{-1}}$, $\langle\rho\rangle = 10^{-18}\, \langle\rho\rangle_{-18}\, \mathrm{g\,cm^{-3}}$ and $c_\infty = 10\, c_{\infty,1}\, \mathrm{km\ s^{-1}}$. For large density enhancements, we have $r_\mathrm{w} \ll r_\mathrm{c} \approx 1\,\mathrm{pc}$ and, therefore the stellar winds would be unable to significantly impede the inflowing of gas.

2.4.1.2 Globular Clusters

Globular cluster's orbits are primarily dictated by the host galactic potential (Harris, 1991). In the Milky Way, globular clusters (GCs) are observed to move at highly supersonic velocities $\mu_\infty \sim 5-10$ (Dinescu *et al.*, 1997). In addition, the gas within the galactic halo is expected to be virialized so that $c_\infty \approx u_\infty$, implying $V^2 \gg GM_\mathrm{p}/\varpi_\mathrm{c}$. As a result, for a typical GC with $M_\mathrm{p} = 3.5 \times 10^5\, M_\odot$ and $\varpi_\mathrm{c} = r_\mathrm{c} = 2\,\mathrm{pc}$ moving at $\mu_\infty = 4.0$, one expects negligible mass accumulation as $r_\mathrm{s} \lesssim r_\mathrm{c}$. This is true even if the cluster is surrounded by cold, efficiently cooling ambient gas ($c_\infty = 10\,\mathrm{km\,s^{-1}}$ and $\gamma = 1.01$) as shown in Figure 2.10 (model B). In this case, for a background density similar to that of the ISM, $\rho_\infty \approx 10^{-24}\,\mathrm{g\,cm^{-3}}$, the accumulated mass is only $M_\mathrm{acc}/M_\mathrm{p} \approx 2 \times 10^{-6}$.

A GC might collect gas more effectively if its orbit happened to lie in the disc plane of its host galaxy. If the GC moving with $\mu_\infty \leq 2$ through the galactic disc, we might expect the mass accumulation to more closely resemble that seen for model A in Figure 2.10. However, these conditions are rare for GCs (Dinescu *et al.*, 1997).

2.4.2 Galactic Systems

Hernquist potentials (Hernquist, 1990) are used to describe a wide variety of galactic systems - from the dark matter halos of dwarf galaxies and Milky Way sized systems, to the

halos of galaxy clusters (Adén *et al.*, 2009; Scott *et al.*, 2009; Hwang and Lee, 2008). In what follows we assume, for simplicity, that these gravitational potentials are not significantly modified from their dark matter profiles by the presence of gas or stars.

2.4.2.1 Dwarf Galaxy Halos

Dwarf galaxies (DGs) are seen either moving through the IGM or embedded within larger halos (Diemand *et al.*, 2008; Mateo, 1998). For those moving under the influence of a larger gravitational potential we expect that, on average, DGs to orbit around the ambient gas with a velocity comparable to the circular velocity of their host: $V^2 \gtrsim GM_{\rm h}/a$. However, many DGs are found to reside in nearly radial orbits, and thus will spend only a small fraction of their orbital time moving at lower velocities (Diemand *et al.*, 2008, 2007).

For example, a DG on a highly elliptical orbit, $e = 0.9$, will spend approximately 1% of its orbital period moving at less than 20% of the host's circular velocity. During this period a large central density enhancement is expected to be effectively sustained within the DG' core if $GM_{\rm h}/a \gtrsim c_\infty^2 + u_\infty^2$. That is, if the DG is surrounded by cold gas with $c_\infty^2 \lesssim GM_{\rm h}/a$. Such an ideal situation for mass accumulation is illustrated by model C in Figure 2.11. In these conditions, if the density of cold gas is $\rho_\infty = 10^{-25}\,{\rm g\,cm^{-3}}$, the mass collected by the DG could be as large as[1] $M_{\rm acc}/M_{\rm h} \approx 0.14$. In contrast, if the surrounding gas is virialized, $c_\infty \approx \sigma_{\rm v,host} \gg GM_{\rm h}/a$, the DG halo will spend most of its orbit with mass inflows similar to those depicted for model D in Figure 2.11. In this case, for $\rho_\infty = 10^{-25}\,{\rm g\,cm^{-3}}$, the accumulated

[1] We note here that model C has been run until a quasi-static density profile has been established, which takes about a few core sound crossing times. If the DG is at apogee for a shorter time, the accumulated mass is expected to be lower.

mass is only $M_{\rm acc}/M_{\rm h} \approx 5 \times 10^{-4}$.

2.4.2.2 Halos in Merging Systems

A massive galactic halo is likely to experience a relatively equal mass merger during its lifetime. Galaxies of $M \approx 10^{11}\,M_{\odot}$ will have undergone, on average, about one merger with a galaxy of $M \gtrsim 5 \times 10^{10}\,M_{\odot}$ since $z = 1.2$ (Robaina *et al.*, 2010). Because the smaller component is moving under the gravitational influence of a halo of similar mass, we expect $u_{\infty} \approx \sigma_{\rm v}$. Moreover, if gas is effectively virialized within more massive halo, then $c_{\infty} \approx \sigma_{\rm v}$ and, as a result, a large density build up is expected to be effectively retained in the core of the smaller halo. This situation is depicted in Figure 2.12 (model E), in which a a Milky Way-like sized halo is simulated moving through hot gas with $c_{\infty} = 100\,{\rm km/s}$ at $\mu_{\infty} = 2.0$. Comparing the bremsstrahlung cooling and the core sound crossing time, we find $t_{\rm cool} \gtrsim t_{\rm dyn}$. Since cooling is expected to be inefficient, we assume $\gamma = 5/3$. While $r_s \gtrsim \varpi_c = a$, ineffective cooling results in an accumulated mass of only $M_{\rm acc}/M_{\rm h} = 10^{-2}$ for ambient densities of $\rho_{\infty} = 10^{-27}\,{\rm g\,cm^{-3}}$.

2.4.2.3 Galaxy Clusters

Similar to the case discussed above, a large central gas density enhancement is expected in equal mass merging galaxy clusters, such as the Bullet cluster complex. The Bullet cluster is a galaxy cluster merging with another slightly more massive cluster (Markevitch *et al.*, 2002). In this case, $M_{\rm h} = 10^{15}\,M_{\odot}$, $\varpi_{\rm c} = a = 1\,{\rm Mpc}$, $\mu_{\infty} = 2.5$, and $c_{\infty} = 1580\,{\rm km\,s^{-1}}$. For an inefficiently cooled gas ($\gamma = 5/3$), this results in $r_{\rm s} \approx \varpi_{\rm c} = a$. Such situation is depicted in Figure 2.13 (model F). Assuming IGM densities of $\rho_{\infty} = 10^{-27}\,{\rm g\,cm^{-3}}$ results in an accumulated mass

of $M_{\rm acc}/M_{\rm h} = 3.5 \times 10^{-4}$. This simple model of the Bullet cluster gives similar flows structures to those found in more sophisticated calculations which include the stellar and gas mass distributions.

2.5 Discussion

In §2.4 we have shown the conditions required to collectively accumulate large quantities of gas from the ambient medium in the centers of a variety of astrophysical systems thought to be well described by a core gravitational potential. The consequences of large mass accumulation in such systems fall into two basic categories. First, if the gas cools effectively star formation can be triggered, generating new stellar members in the system. Second, if the gas accretes efficiently onto the core's current stellar population, the state of these stellar systems (and possibly the central black hole) can be significantly perturbed. In what follows we discuss the implications of gas accumulation and their accompanying observational signatures.

2.5.1 The State of the Accumulated Gas

2.5.1.1 Emission Properties

The emission properties of the accumulated gas in clusters of galaxies and young stellar clusters are briefly reviewed in this section. At temperatures $\gtrsim 3 \times 10^7$ K, the primary cooling process for intracluster gas is thermal bremsstrahlung, while for temperatures $\lesssim 3 \times 10^7$ K, line cooling becomes very important. For the the intracluster gas in most star clusters, the cooling time is longer than the Hubble time (age of the universe). Thus cooling is not dynam-

ically very important in these cases. Figure 2.14 (bottom panel) shows the surface brightness profile, calculated assuming optically thin cooling resulting from bremsstrahlung and collisionally excited metal transitions, for a cluster merging environment with parameters selected to mimic the Bullet Cluster complex (model F). We find an integrated bolometric luminosity of $L_{\rm bol} \approx 10^{44}\,{\rm erg\,s^{-1}}$ and a bowshock structure that are comparable to those observed by *Chandra* (Markevitch, 2006; Markevitch *et al.*, 2002). In the center of the cluster, where cooling is important, our calculated emission is considerably harder than found in simulations including the cooling term in the energy equation (Milosavljević *et al.*, 2007).

Also shown in Figure 2.14 is the surface brightness profile of the accumulated gas in a young star cluster with parameters similar to those seen for the stellar cluster members in the Antennae galaxy merging system (model A). To calculate the emission we assume optically thin cooling, where we employ an effective cooling curve. In the cluster's core, the near infrared (NIR) surface brightness is approximately $\approx 10^{41}\,{\rm erg\,s^{-1}\,pc^{-2}}$, which is probably optimistic given that we do not explicitly include the cooling term in the energy equation but instead use an adiabatic simulation. This simple model gives, nonetheless, results that are consistent with the observed range of luminosities in the Antennae star clusters: $L_{\rm NIR} = 10^{39} - 10^{42}\,{\rm erg\,s^{-1}}$ (Brandl *et al.*, 2005a). For clusters embedded in these types of merging environments, the emission from the bowshock and cluster core should distinguishable[2] given enough spatial resolution and provided the reprocessed stellar radiation is not the dominant contribution to the NIR.

[2]This is because the change in brightness across these two components is at least two orders of magnitude.

2.5.1.2 Enhanced Central Densities Leading to Star Formation

If the gas collected by these potentials cools efficiently, we would expect it to fragment and form stars if the density is high enough. In general, one can relate the gas density to the star formation rate (Kennicutt, 1998): $\Sigma_{\rm sfr} \approx 10^{-4}\ (\Sigma_{\rm gas}/10^4 M_\odot\,{\rm pc}^{-2})^{1.4}\ M_\odot\,{\rm yr}^{-1}\,{\rm pc}^{-2}$, where $\Sigma_{\rm sfr}$ and $\Sigma_{\rm gas}$ are the star formation and gas column densities, respectively. A dwarf galaxy, for example, embedded within a larger halo with properties similar to those assumed for model C (i.e., $\rho_\infty = 10^{-24}\,{\rm g\,cm^{-3}}$ and a 200 pc star forming region) is expected to form stars at a rate of $\Sigma_{\rm sfr} = 10^{-1}\,{\rm M_\odot\,yr^{-1}}$, similar to that predicted by star formation simulations in these systems (Sawala *et al.*, 2011).

For the star clusters embedded in the Antennae galaxy merging system, whose conditions are relatively well described by our model A, we find $\Sigma_{\rm sfr} \approx 4\times10^{-2}\,{\rm M_\odot\,yr^{-1}}$ per system, or a total rate of $\Sigma_{\rm sfr} \approx 4(N_{\rm c}/10^2)\,{\rm M_\odot\,yr^{-1}}$ for all $N_{\rm c}$ clusters. Such star formation rates were calculated assuming a star forming region of 5 pc and a background ambient density of $\rho_\infty = 10^{-21}\,{\rm g\,cm^{-3}}$, which results in an average increase in cluster gas core density of $\langle\rho\rangle = 10^{-18}\,{\rm g\,cm^{-3}}$ (model A). The resulting rates are similar to those observed in the Antennae complex (Gilbert and Graham, 2007a). If we assume that such rates are effectively sustained over the calculated orbital passage time scale of about 20 Myrs (Karl *et al.*, 2010), one expects at least $10^5\,{\rm M_\odot}$ of new stars to be created per system. More detailed simulations that take into account self-gravity, realistic cooling and feedback effects are needed before detailed comparisons can be made with the inferred conditions required to explain subsequent episodes of star formation in stellar clusters (Conroy and Spergel, 2011; Gratton *et al.*, 2004; Carretta *et al.*,

2010a; Piotto, 2009a; Mackey *et al.*, 2008).

2.5.2 Accretion Onto Individual Stellar Members and the Central Massive Black-hole

A compact star (or a black hole) of mass M_*, moving with relative velocity u through a gas of ambient density ρ_∞ and sound speed c_∞, nominally accretes at the Bondi-Hoyle-Lyttleton rate: $\dot{M} \approx 4\pi(GM_*)^2\rho_\infty(u^2+c_\infty^2)^{-3/2}$. If, however, the collective potential of the system (e.g. star cluster or galaxy) was able to significantly increase the surrounding gas density prior to being accreted onto the individual neutron star members, then the accretion rates of the individual core stellar members (or the central black hole) would be enhanced by $\sim \langle\rho\rangle/\rho_\infty$, where $\langle\rho\rangle$ is the average increase in gas density in the core. It is to this problem that we now turn our attention. In particular, we study the effects of enhanced accretion rates onto the white dwarf core members and the central massive black hole.

2.5.2.1 White Dwarfs in Stars Clusters and Galaxies

In mature stellar systems, we expect a significant fraction of the stellar mass to be in white dwarfs. If the collective potential of the system (which contains the white dwarfs) is able to alter the ambient gas properties before the gas is accreted onto the individual stars, then the resulting enhanced accretion rates could significantly alter the state of the accreting stellar population. If, however, the density is not significantly increased, then the stars accrete gas as though they move through the external medium independently.

The resulting mass accretion rates for the white dwarf members depends on the radial

distribution of both stars and gas. Here we calculate the expected mass accretion rates in the core of slowly moving star cluster (model A) using two extreme examples for the radial distribution of white dwarfs remnants. The first one is based on Fokker-Planck models of a core collapsed (centrally condensed) globular cluster (Dull *et al.*, 1997a), and the second simply assumes that the white dwarfs, containing 1% of the total mass, follow the radial stellar mass distribution. Figure 2.15 shows the mass accretion rate distribution of the white dwarf cluster members for both radial distributions (solid and dashed lines respectively).

This range of mass accretion rates are expected to result in enhanced novae rates (Nomoto *et al.*, 2007). With a nova outburst rate of $\Psi_{\rm nr} \approx 10^{-4}$ yr^{-1}, we expect about $\approx 0.1(\Psi_{\rm nr}/10^{-4}\ {\rm yr}^{-1})\ (N_{\rm wd}/10^4)(N_{\rm c}/10^2)$ outbursts per year. This is probably a conservative estimate as the individual novae rates are expected to increase to $\Psi \leq 10^{-1}$ yr^{-1} for the larger accretion rates calculated here (Starrfield *et al.*, 1985). These novae outbursts will be observed as super soft X-ray sources ($kT \leq 1$keV) with luminosities $\lesssim 10^{38}\,{\rm erg\,s^{-1}}$ and thus might be observable in nearby merging galaxies (Hernanz and Sala, 2010).

Such high mass accretion rates can only be sustained if star clusters move slowly with respect to the background gas. While there are no stellar clusters observed in the Galactic disk which bear these anticipated properties (the relative velocity of the halo clusters to the interstellar medium is in the range of 100 km s^{-1}), observations of several cluster knots in the Antennae indicate intracluster relative velocities that comparable to the central velocity dispersions. In these systems, it has been shown that this merging state is, however, short lived, $\Delta t \lesssim 20\,{\rm Myr}$ (Karl *et al.*, 2010). Even if this (slowly moving) cold gas phase persists for $\leq 20\,{\rm Myr}$, we expect at least 30% of the white dwarf members to double their mass. This

increase in mass would in turn lead to a sizable increase in luminosity (e.g. Mestel, 1952), which in turn modify the white dwarf cooling sequence.

2.5.2.2 Accretion onto Central Massive Black Holes

Most early-type galaxies and spiral bulges are now thought to contain massive black holes in their nuclei (Magorrian *et al.*, 1998a). Direct evidence is also now available which supports the idea that active galaxies are powered by massive black holes. It can then be argued that many if not all galaxies could be expected to have undergone an active phase and to possess a central massive black hole (Haehnelt and Rees, 1993), although the presence of intermediate mass black holes in dwarf galaxies (and some globular clusters) remains controversial (Ulvestad *et al.*, 2007a; Gebhardt *et al.*, 2005a; Baumgardt *et al.*, 2003a).

Large density enhancements in the nuclei of galaxies, dwarf galaxies and star clusters would be accompanied by enhanced mass supply to the central black hole. For a typical galactic halo (model E), this enhanced mass accretion results in a significant black hole accretion luminosity:

$$L_{\rm bh} \approx 10^{41} \frac{M_{\rm bh}}{10^6 M_\odot} \frac{\epsilon}{0.1} \,{\rm erg\,s^{-1}}, \tag{2.31}$$

where ϵ is the efficiency for converting gravitational energy into radiation. Extrapolating the $M_{\rm bh} - \sigma$ relation (Tremaine *et al.*, 2002) to the star clusters and dwarf galaxies modeled by simulations [A, B, C, D] gives black hole masses of $M_{\rm bh} = [0.68, 0.68, 1.42, 1.42] \times 10^4 M_\odot$ and accretion luminosities of $\log L_x/L_{\rm edd} = [10^{1.77}, 10^{-1.46}, 10^{2.18}, 10^{-6.20}]$, respectively. While the integrated output from this increased mass feeding could, in principle, amount to large factors

of the black hole's Eddington luminosity, it would probably be significantly less because we have, for simplicity, neglected feedback.

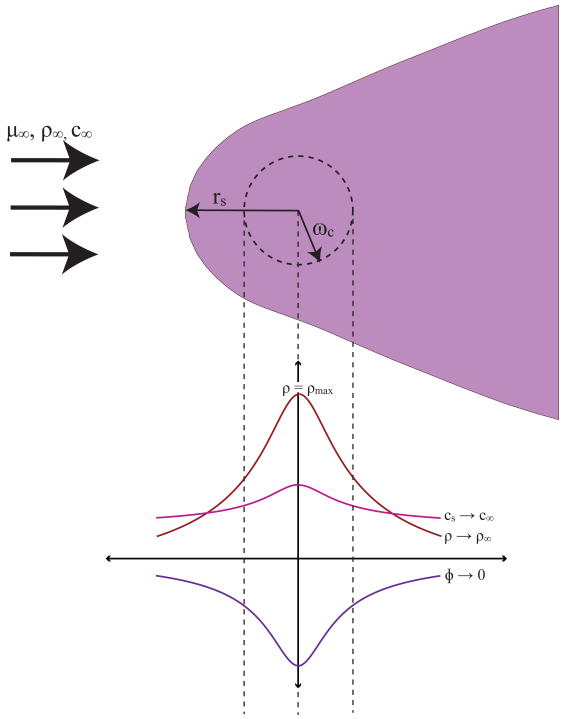

Figure 2.1: Diagram shows the flow geometry of non-stationary core potentials with central mass accumulation. A bow shock is produced by the motion of the potential with respect to the ambient gas. The initial asymptotic Mach number, sound speed and density of the inflowing gas are denoted here as μ_∞, c_∞ and ρ_∞, respectively. Also depicted are the characteristic, r_s, and the core, ϖ_c, radii, together with a sketch of the expected profiles of density, $\rho(r)$, and sound speed, $c_\mathrm{s}(r)$, along the flow axis.

90

Table 2.1: Astrophysically Motivated Simulations

Simulation Label	γ	c_∞ [km s^{-1}]	μ_∞	ϖ_c [pc]	M_p or M_h [M$_\odot$]	Analytic $\log(\rho_{max}/\rho_\infty)$	Simulated $\log(\rho_{max}/\rho_\infty)$	Analytic r_s [pc]	Simulated r_s [pc]	u_{max}/c_∞
A[a]	1.01	10	2	1	3.5×10^5	6.03	4.32	2.7	1.7	3.8
B[b]	1.01	10	4	2	3.5×10^5	3.12	1.08	1.34	0[†]	5.3
C[c]	1.01	10	2	200	10^8	8.38	4.79	1500	210	4.8
D[d]	1.67	100	4	200	10^8	0.09	0.03	11	0[†]	4
E[e]	1.67	100	2	3×10^4	8×10^{11}	1.5	0.77	1.5×10^5	1.4×10^4	3.23
F[f]	1.67	1580	2.5	10^6	10^{15}	0.5	0.86	6×10^5	3.6×10^5	4.4

[a]Young star cluster modeled here by a Plummer potential.

[b]Globular cluster modeled by a Plummer potential.

[c]Slowly moving dwarf galaxy in cool gas modeled by a Hernquist potential.

[d]Slowly moving dwarf galaxy in hot gas modeled by a Hernquist potential.

[e]Milky Way sized halo moving through hot gas modeled by a Hernquist potential.

[f]Simulation of galaxy cluster similar to the Bullet Cluster, modeled by a Hernquist potential.

[†]These simulations resulted in a detached tailshock.

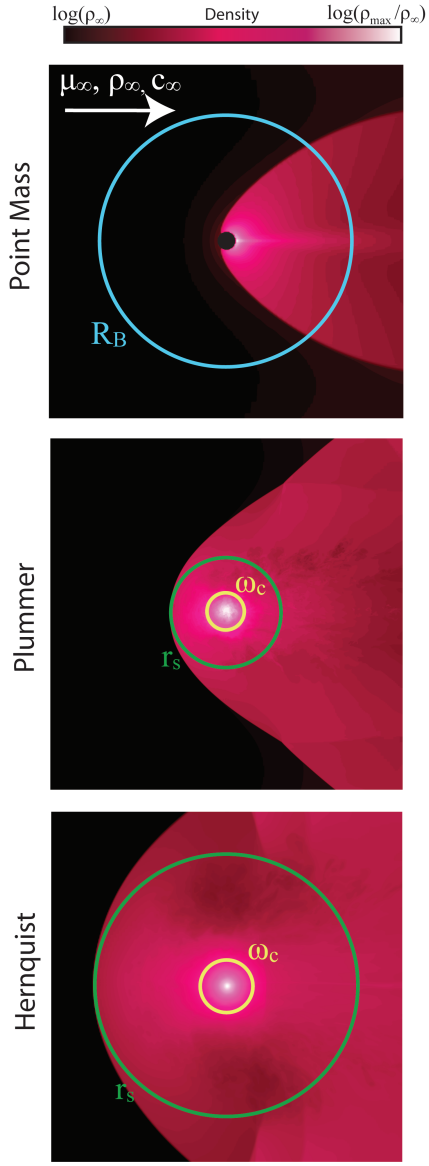

Figure 2.2: Density contours of the flow pattern around point mass, Plummer and Hernquist potentials set in motion through an initially uniform medium with $\rho_\infty = 1$ and $\mu_\infty = 2$. The point mass potential is implemented here with a sink boundary following the method of Ruffert (1994b) by flooring the values of density and pressure to 50% of their background values and setting the velocities to zero inside the sink radius. Color bars show density cuts through the xy-plane with limiting values: $\log(\rho_{\max}/\rho_\infty) = [1.2, 1.1, 1.5]$ for point mass, Plummer and Hernquist potentials, respectively. The equation of state used here is adiabatic ($\gamma = 5/3$). Also depicted are the characteristic, r_s (which reduces to the Bondi radius R_B for a point mass potential), and the core, ϖ_c, radii. The Plummer and Hernquist potentials have been constructed to yield the same circular velocity peak radius: r_v. Note that the difference between r_s in the Plummer and Hernquist potentials is consistent with equation (2.30).

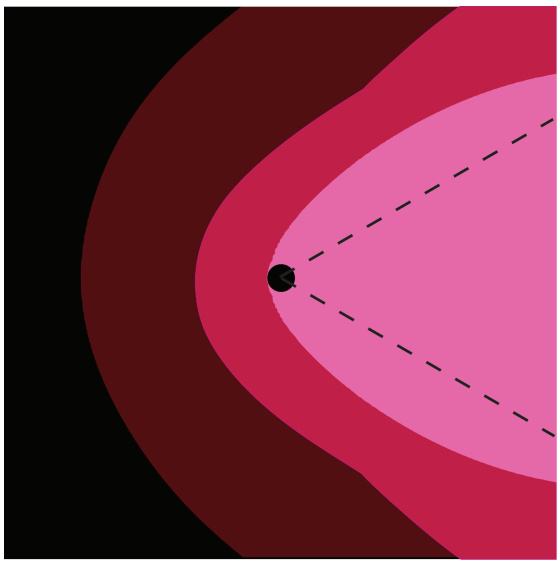

Figure 2.3: Bow shock patterns produced around a point mass (pink), Plummer (red) and Hernquist (brown) potentials set in motion through an initially uniform medium with $\mu_\infty = 2.0$. Also plotted, for comparison, is the bow shock expected for a supersonically moving, non-gravitating object (dashed line). In this case the bow shock's opening angle is simply given by $\theta_{\rm bow} = \arcsin \mu_\infty^{-1}$. The size of the box is 40 times the sink size (used here to model the point mass potential), depicted by the black circle.

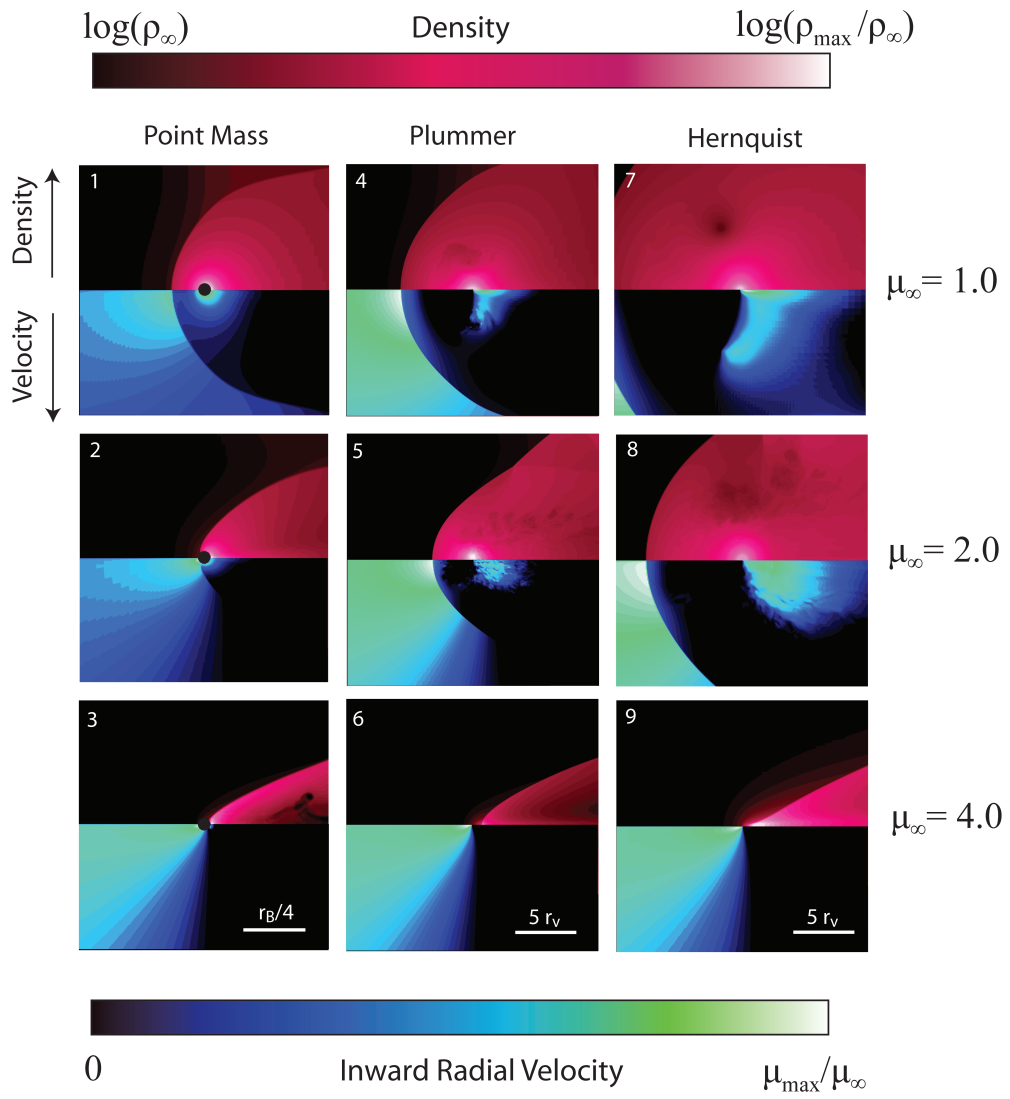

Figure 2.4: Density and radial velocity contours for gas flowing around a point mass, Plummer and Hernquist potential at various relative velocities. We exploit the flow symmetries to plot both the density contrast (upper, maroon half) and inward radial velocity profiles (lower, blue half) in the same panel. Color bars show density and velocity cuts through the *xy*-plane in units of $\log(\rho_{\rm max}/\rho_\infty)$ and μ/μ_∞. The maximum densities and radial velocities attained in simulations 1 through 9 are $\log(\rho_{\rm max}/\rho_\infty) = [1.5, 1.2, 0.8, 1.4, 1.1, 1.4, 1.7, 1.5, 1.1]$ and $(\mu_{\rm max}/\mu_\infty) = [3.9, 6.2, 6.9, 1.9, 3.1, 6.2, 1.7, 2.9, 6.4]$, respectively. The equation of state used here is adiabatic ($\gamma = 5/3$).

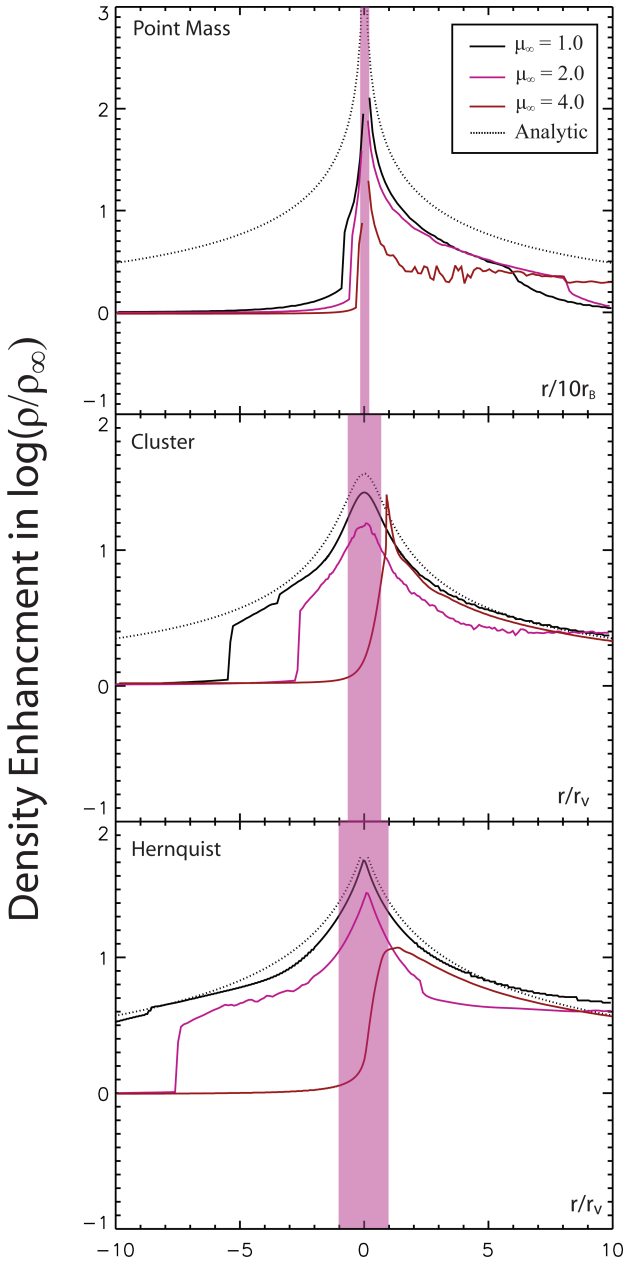

Figure 2.5: Density cuts along the axis parallel to the incoming flow for the simulations shown in Figure 2.4. The dotted lines give the analytic solutions for a point mass, Plummer and Hernquist potential, while the black, pink and red lines show the numerical profiles for $\mu_\infty = 1.0$, 2.0, and 4.0, respectively. The shaded regions depict either the core radii or the sink size.

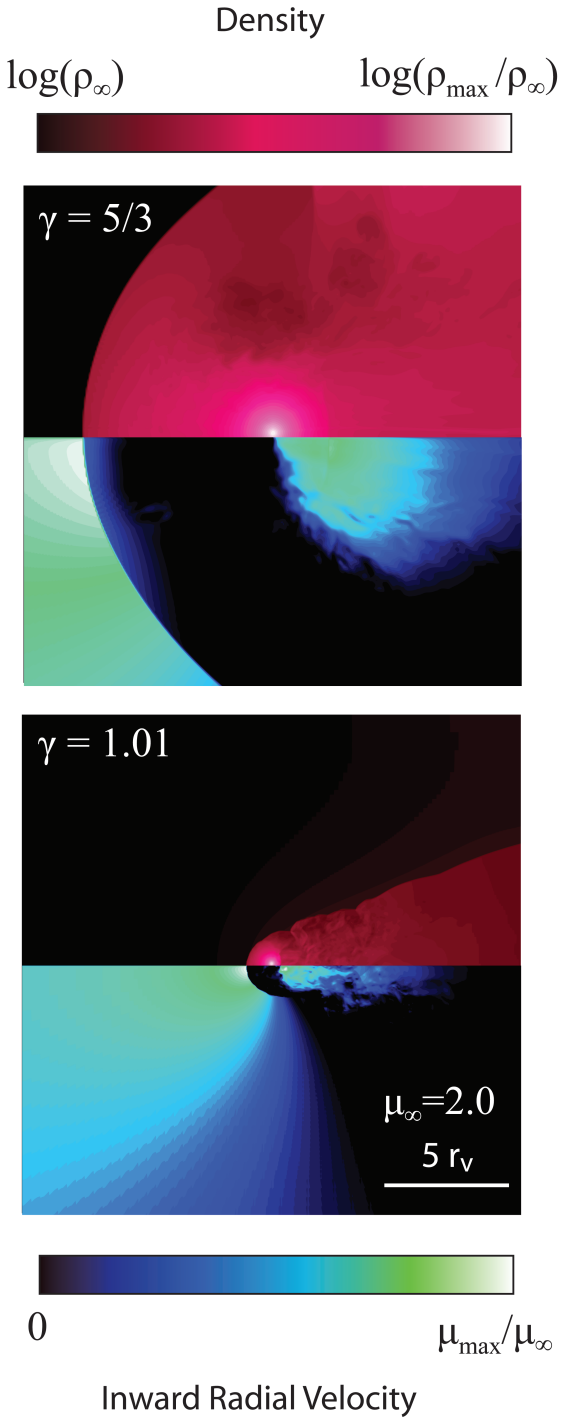

Figure 2.6: Density and radial velocity contours for gas flowing with $\mu_\infty = 2.0$ around a Hernquist potential in the adiabatic ($\gamma = 5/3$) and isothermal ($\gamma = 1.01$) limits. The maximum densities and radial velocities attained in simulations for $\gamma = 5/3$ and $\gamma = 1.01$ are $\log(\rho_{\rm max}/\rho_\infty) = [1.5, 5.1]$ and $(\mu_{\rm max}/\mu_\infty) = [2.9, 4.9]$, respectively.

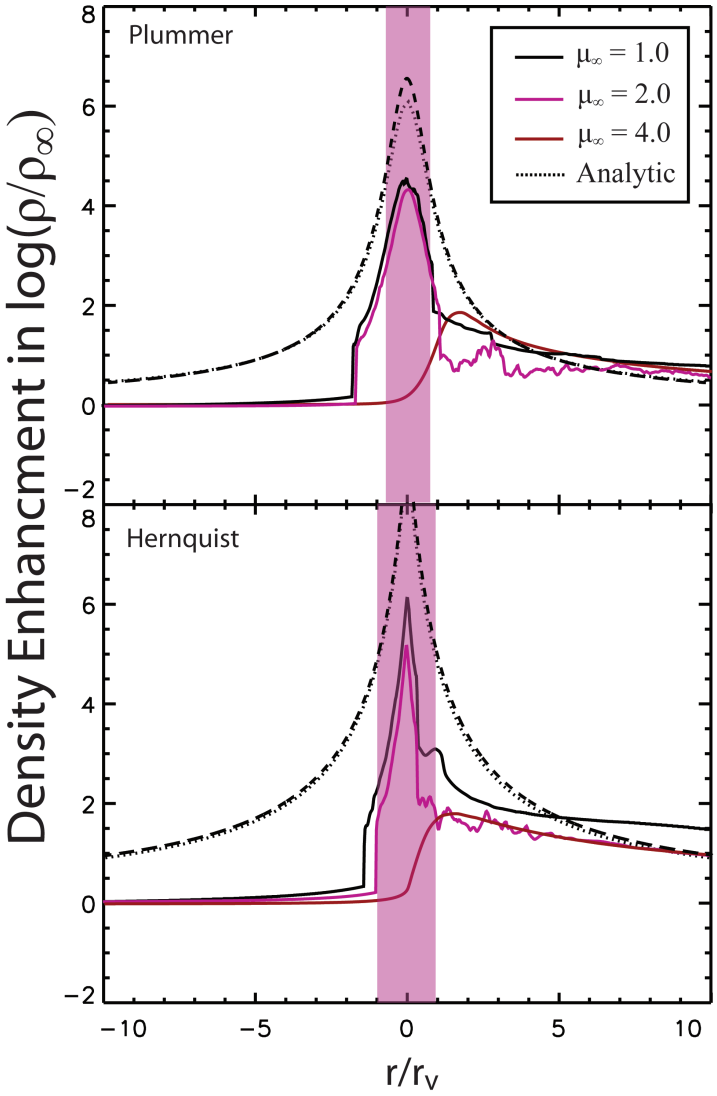

Figure 2.7: Same as Figure 2.5 but for a near isothermal equation of state ($\gamma = 1.01$). The dotted lines are the analytic profiles derived in §2.2, specifically equations (2.23) and (2.25) with $\gamma = 1.01$. The dashed lines are the isothermal form of the density equation, (2.11). The shaded regions show the size of the core.

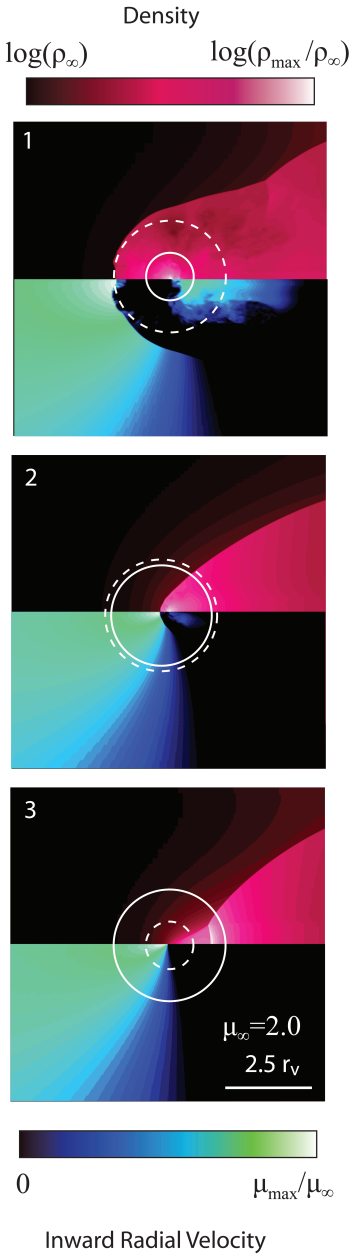

Figure 2.8: Density and radial velocity contours for gas flowing with $\mu_\infty = 2.0$ around a Hernquist potential with varying r_s in the adiabatic ($\gamma = 5/3$) limit. Dashed circles depict the location of the analytic characteristic radius, r_s (equations [2.19] and [2.20]), while solid circles give the approximate location of the core radius ϖ_c. The maximum densities and radial velocities attained in simulations 1 through 6 are $\log(\rho_{max}/\rho_\infty) = [1.8, 1.3, 1.0]$ and $(\mu_{max}/\mu_\infty) = [3.3, 3.6, 3.2]$, respectively.

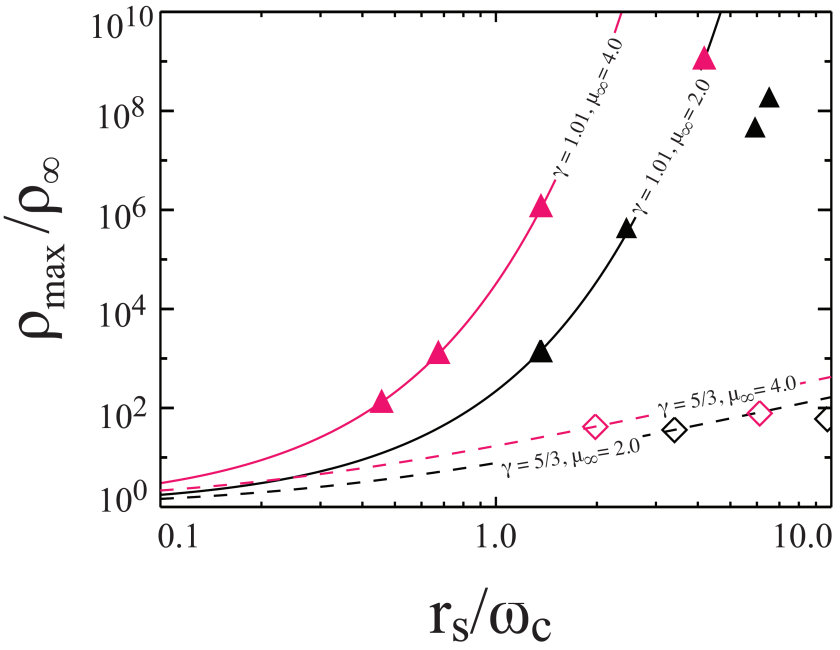

Figure 2.9: Expected density enhancements as a function of r_s/ϖ_c for a variety of simulations with $c_\infty = 10\,\mathrm{km\,s^{-1}}$. The triangles (diamonds) are measured ρ_{max}/ρ_∞ and r_s/ϖ_c from the isothermal (adiabatic) simulations. For comparison, the lines are trends of ρ_{max}/ρ_∞ from the analytic results from equations (2.20) and (2.23) for Plummer potentials with a variety of masses and core radii in $c_\infty = 10\,\mathrm{km\,s^{-1}}$ gas.

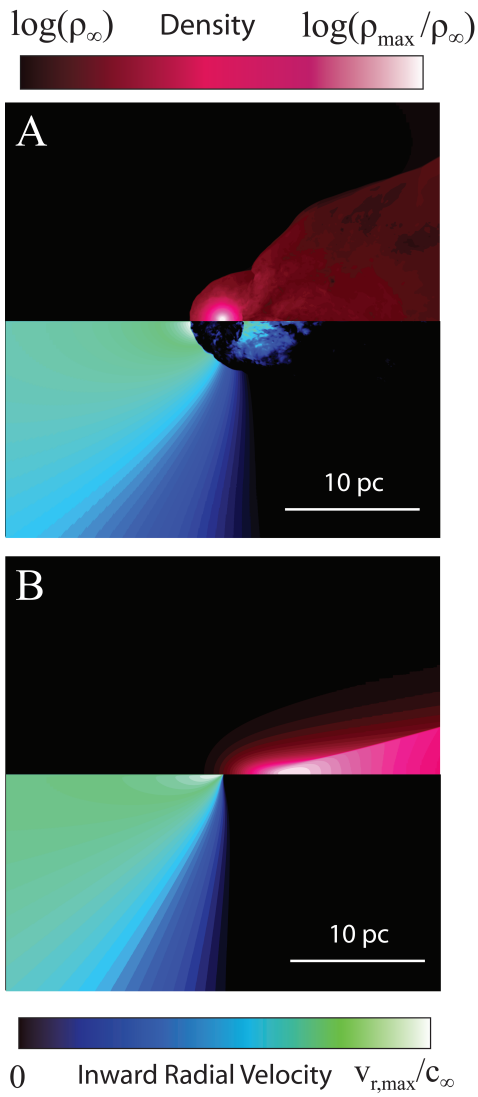

Figure 2.10: Examples of gas accumulation in star clusters. Density and radial velocity contours for models A and B. The maximum densities and radial velocities attained in the simulations are $\log(\rho_{\rm max}/\rho_\infty) = [4.32, 1.08]$ and $(u_{\rm max}/c_\infty) = [3.8, 5.3]$, respectively.

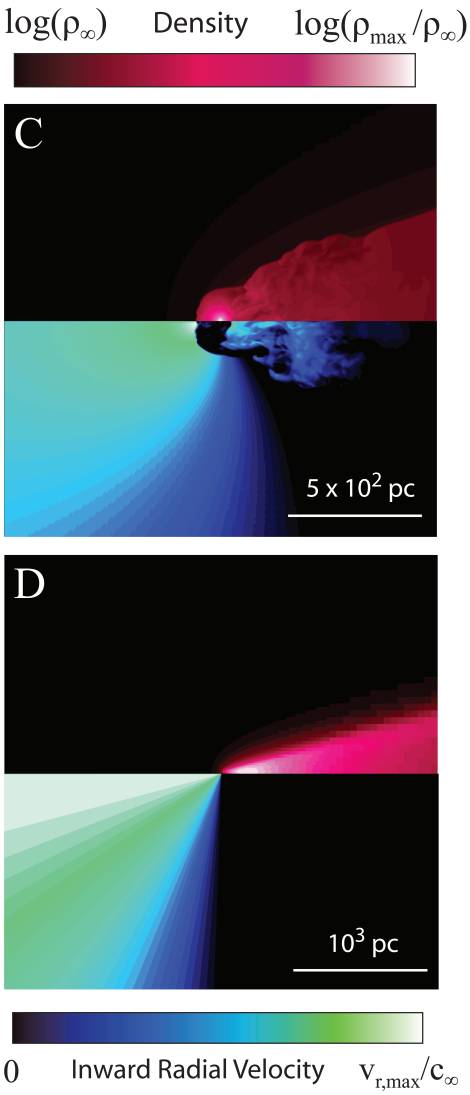

Figure 2.11: Examples of gas accumulation in dwarf galaxies. Density and radial velocity contours for models C and D. The maximum densities and radial velocities attained in the simulations are $\log(\rho_{\max}/\rho_\infty) = [4.79, 0.03]$ and $(u_{\max}/c_\infty) = [4.8, 4.0]$, respectively.

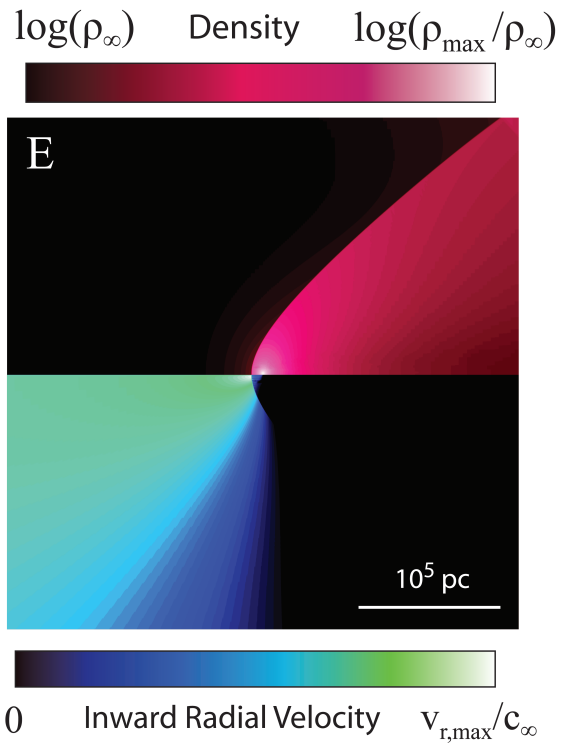

Figure 2.12: Gas accumulation for a Milky Way-like halo moving in a major merging environment. Density and radial velocity contours for model E. The maximum densities and radial velocities attained in the simulation are $\log(\rho_{\max}/\rho_{\infty}) = 0.77$ and $(u_{\max}/c_{\infty}) = 3.23$, respectively.

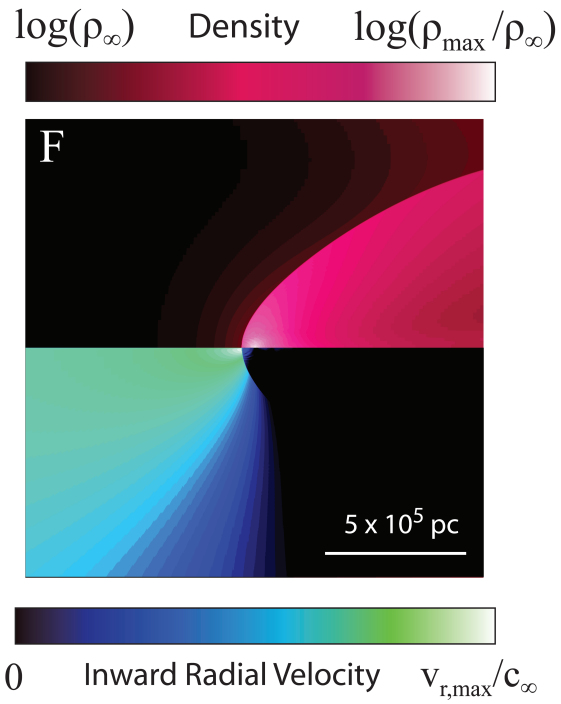

Figure 2.13: Gas accumulation for a galaxy cluster in a major merger environment. Density and radial velocity contours for model F. The maximum densities and radial velocities attained in the simulation are $\log(\rho_{\max}/\rho_{\infty}) = [0.86]$ and $(u_{\max}/c_{\infty}) = [4.4]$, respectively.

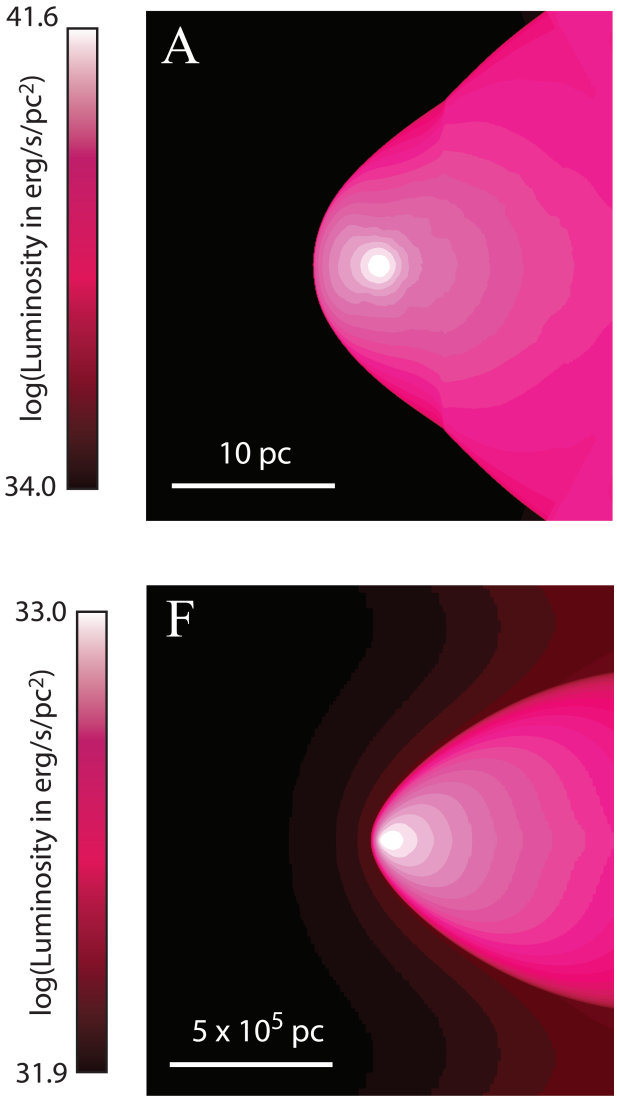

Figure 2.14: The emission properties of the accumulated gas in a galaxy cluster (model F) and a young stellar cluster (model A). Emission is calculated using the cooling curves for an optically thin plasma from Peres *et al.* (1982) for chromospheric energy losses in the temperature range $4.44 \times 10^3 < T < 2 \times 10^4\,K$, the curves of Rosner *et al.* (1978) for coronal temperatures of $2 \times 10^4 < T < 10^8\,K$, and bremsstrahlung emission above $10^8\,K$. We assume $\gamma = 5/3$. That is, the cooling term is not explicitly included in the energy equation. The ionization fraction is assumed to be purely collisional, giving $\chi_i = 0.003$ for model A and $\chi_i \sim 1$ for model F. Model A has a temperature range in the band $kT = 0.6 - 7.2\,\mathrm{eV}$, while for model F the range is $kT = 15.0 - 146.0\,\mathrm{keV}$.

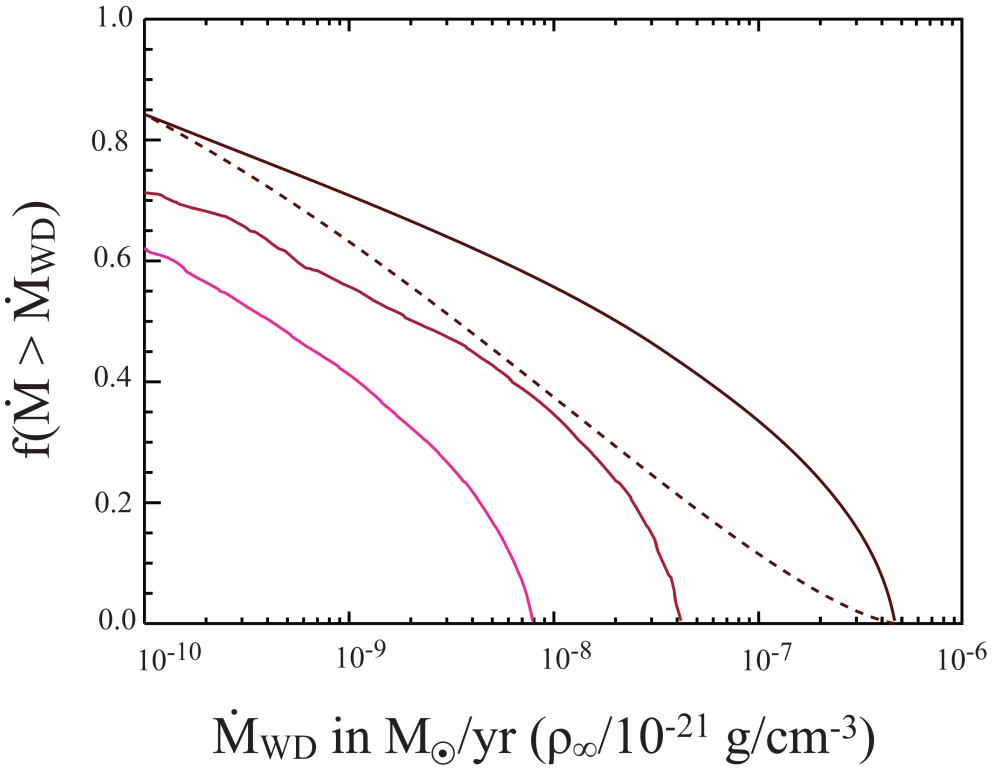

Figure 2.15: The mass accretion rate fraction, f, of the white dwarf cluster members for both centrally condensed (solid line) and non-condensed (dashed line) compact remnant distributions. The gas density profile for model A has been used, with $\rho_\infty = 10^{-21}\,\mathrm{g\,cm^{-3}}$. To calculate the mass accretion distributions we have assumed $M_{\rm wd} = 1\,M_\odot$ and $u_{\rm wd} = 15\,\mathrm{km\,s^{-1}}$. The red (brown) line was calculating using the numerical density profile for $\mu_\infty = 2.0\,(0.5)$. The black line assumes the analytic profile for $\mu_\infty = 2.0$.

Chapter 3

Gas Accretion by Star Clusters and the Formation of Ultraluminous X-ray Sources from Cusps of Compact Remnants

3.1 Introduction

Over the years, the existence of two distinct populations of black holes has been established beyond a reasonable doubt. Supermassive black holes, $M > 10^6 M_\odot$, are inferred in many galactic centers (Kormendy and Richstone, 1995; Magorrian *et al.*, 1998b), while stellar mass black holes, $M \sim 1-10 M_\odot$, have been identified by their interaction with companion stars (McClintock and Remillard, 2006). The situation at intermediate masses, $M \sim 10^2 - 10^5 M_\odot$, is still uncertain despite recent evidence for mass concentrations within the central regions of some globular clusters (Gebhardt *et al.*, 2005b; Ulvestad *et al.*, 2007b; Noyola *et al.*, 2008). This evidence remains controversial, partly because the velocity dispersion profiles can be reproduced

without invoking the presence of an intermediate mass black hole (IMBH) (Baumgardt *et al.*, 2003b,c; Dull *et al.*, 2003; Anderson and van der Marel, 2009).

Recently, some evidence has arisen for the presence of IMBHs in moderately young star clusters, where ultra-luminous, compact X-ray sources (ULXs) have been preferentially found to occur (Fabbiano *et al.*, 2001; Trinchieri *et al.*, 2008). Their high luminosities have been interpreted as imprints of IMBHs, rather than binaries containing a normal stellar mass black hole (Zezas *et al.*, 2006). In this Chapter, we present an alternative explanation for the overabundance of ULXs associated with young clusters in galaxies such as the Antennae and Cartwheel. In this new paradigm, the accretion of gas by the collective star cluster potential moving through the merging medium is strongly enhanced relative to the individual rates and, as a result, the aggregate X-ray luminosity arising from the core of neutron star cluster members can exceed $> 10^{39}$ ergs^{-1}. Much of the effort herein will be dedicated to understanding the conditions by which the collective potential of a star cluster is able to accrete gas with highly enhanced rates and its effect on the integrated accretion luminosity of the neutron star cluster members. The conditions found in systems such as the Antennae galaxy, as we will argue, are favorable for this type of mechanism to operate effectively and produce an overabundance of ULXs.

3.2 ULX Cusps from Compact Stellar Cluster Members

ULXs are seen in the star clusters of merging galaxies, such as the Antennae and the Cartwheel (Trinchieri *et al.*, 2008; Zezas *et al.*, 2006). These sources are compact in nature and

in general associated with super star clusters (SSCs) - young, compact, massive clusters of stars (Zezas *et al.*, 2002). Many of these sources have luminosities $\geq 10^{39}\,\mathrm{erg\,s^{-1}}$, which suggest that they could be IMBHs rather than binaries containing a normal stellar mass black hole.

A compact star of mass M_*, moving with relative velocity v through a gas of ambient density ρ and sound speed c_s, nominally accretes at the Bondi-Hoyle-Lyttleton rate: $\dot{M} \approx 4\pi(GM_*)^2\rho(v^2+c_s^2)^{-3/2}$ (Edgar, 2004). For a NS of mass $M_* = M_{\rm NS} = 1.4M_\odot$ and radius $R_{\rm NS} = 10$ km, the corresponding X-ray luminosity is given by

$$L_X = \epsilon G M_{\rm NS}\dot{M}R_{\rm NS}^{-1} = 10^{32} n\epsilon \left(\frac{V}{10\ \mathrm{km/s}}\right)^{-3}\ \mathrm{erg/s}, \tag{3.1}$$

where $\epsilon \leq 1$ is the efficiency for converting gravitational energy into X-ray radiation, $n = \rho/m_p$ is the hydrogen number density in units of $\mathrm{cm^{-3}}$ and $V = (v^2+c_s^2)^{1/2}$. The integrated X-ray accretion luminosity of $N_{\rm NS}$ neutron star cluster members is then given by

$$L_X = 10^{36}(N_{\rm NS}/10^4) n\epsilon (V/10\ \mathrm{km/s})^{-3}\ \mathrm{erg/s}. \tag{3.2}$$

In order for an aggregated accretion model to successfully describe ULXs, the predicted X-ray luminosity must naturally span the range of observed luminosities. This requires that the resulting speed V not be too large but more importantly that the external density be relatively high. Direct observational searches for cluster gas in the form of molecular, neutral, and ionized hydrogen have yielded non-detections, implying upper limits on the total gas content in the range of 0.1-10 $M_\odot$ (Smith *et al.*, 1995a). In a search for ionized gas Knapp *et al.*

(1996a) found upper limits of 0.1 $M_\odot$ within about one core radius for the clusters, implying $n_{\rm H+} \leq 50\ {\rm cm}^{-3}$.

A simple argument can be made to determine a lower limit to the density of the gas in the cores of globular clusters (GCs) in the absence of gas retention (Pfahl and Rappaport, 2001a). Suppose that the inner core of a GC contains $N_* = 10^2 N_{*,2}$ red giant stars, and so their mean separation is $r_\perp = 6.4 \times 10^{16} N_{*,2}^{-1/3} r_{\rm c,-1}$ cm, where $r_{\rm c} = 0.1 r_{\rm c,-1}$ pc. A lower limit on the wind density can be made by assuming that the wind of each of the stellar member extends only to its closest neighbors. In this approximation, $n > n_{\rm w} = 80 N_{*,2}^{2/3} r_{\rm c,-1}^{-2} v_{\rm w,1}^{-1} \dot{M}_{\rm w,-7}\, {\rm cm}^{-3}$, where $v_w = 10 v_{\rm w,1}$ km s^{-1} and $\dot{M}_{\rm w} = 10^{-7} \dot{M}_{\rm w,-7}$ M$_\odot$ yr^{-1} are the velocity and mass loss rate of the stellar core members. When the cluster gravity and the interaction between stellar winds is taken into account, we suspect that the gas density can be larger than this value.

For clusters that are moving through a relatively dense medium, as in Antennae galaxy for which CO measurements give $n \sim 10^3$ cm^{-3} (Zhu *et al.*, 2003b), the collective external mass accretion is likely to shape the luminosity function for the accreting central cluster of neutron stars. A density of 10^3 cm^{-3}, however, gives an aggregate neutron star luminosity of about $L_X = 10^{38} (N_{\rm NS}/10^4)\ (\epsilon/0.1)(V/10\,{\rm km/s})^{-3}$ erg/s, which is not high enough to explain ULXs (Kalogera *et al.*, 2004; Maccarone *et al.*, 2007; Pfahl and Rappaport, 2001a). If, however, the collective potential of the cluster was able to significantly increase the surrounding gas density prior to being accreted onto the individual neutron star members, the aggregate X-ray luminosity could exceed 10^{39} erg/s. It is to this problem that we now turn our attention.

3.3 The Cluster Model and Numerical Method

To test the gas density enhancement efficiency of a star cluster, we simulated a cluster potential moving through the merging galaxy medium at various typical velocities using FLASH, a parallel, adaptive mesh refinement hydrodynamics code. This scheme, and tests of the code are described in Fryxell *et al.* (2000b). All star clusters are modeled here with a Plummer potential:

$$\Phi = \frac{GM_{\rm c}}{(r^2 + r_{\rm c}^2)^{1/2}} \tag{3.3}$$

Here, $M_{\rm c}$ is the total cluster mass, taken to be $3.5 \times 10^5 M_{\odot}$ (Zhang and Fall, 1999; Gilbert and Graham, 2007b). We use several typical SSC cluster core radii, $r_{\rm c} = 1, 2, 3$ pc (McCrady and Graham, 2007). For comparison, Whitmore *et al.* (1999b) estimates the typical half-light radius of the Antennae clusters to be (4 ± 1) pc. The core radius is expected to be significantly less than the half-light radius.

Our main goal is to examine the ability of a potential to accrete gas as a function of the relative speed of the potential through the gas, and the gas temperature. Our star cluster, here modeled as a Plummer potential, has been therefore set in motion through an initially uniform medium. The speed of sound far away from the cluster is taken to be $c_{\rm s} \sim 10\,{\rm km\,s^{-1}}$, which is consistent with the inferred intracluster medium temperature $\sim 10^4\,K$ in the Antennae galaxy (Gilbert and Graham, 2007b). Based on observations of several cluster knots in the Antennae galaxy, which indicate intracluster velocity dispersions of order $10\,{\rm km\,s^{-1}}$ (Whitmore *et al.*, 2005), the initial Mach number of the cluster relative to the gas is varied between $\mu_\infty = v_\infty / c_s = 0.5$ to 4.0. Here, v_∞ and c_s are the velocity of the medium and the sound speed at

infinity, respectively. The gas within the dense medium has a temperature selected to give the desired value of c_s and a density $\rho_\infty = 10^{-21}\,\mathrm{g\,cm^{-3}}$, chosen to match the intracluster densities as derived from CO measurements (Zhu *et al.*, 2003b).

The effects of self gravity of the gas are ignored. This is adequate for most of our models, for which the accreted mass is less than the mass responsible for the potential. To improve the controlled nature of the models, we do not explicitly include radiative heating or cooling. The gas, instead, evolves adiabatically. The effects of radiative equilibrium are approximated by having the gas evolve with an adiabatic constant $\gamma = 1.01$, giving nearly isothermal behavior, which is consistent with the presence of a large quantity of dust near these clusters as inferred from infrared observations (Brandl *et al.*, 2005b). In cases where sufficient gas is accreted for it to become self-shielded, cooling could decrease the temperature of the gas significantly, potentially enhancing the accretion rate beyond the values computed here.

We use inflow boundaries on one side of our rectangular grid to simulate the cluster's motion through the ambient media. We run our simulations from initially uniform background density until a steady density enhancement forms in the cluster center, which usually takes a few 10-100 sound crossing times. Several models were run longer to test convergence and density enhancements were found to change only slightly with longer run times. We further tested convergence of our models for several resolutions and domain sizes. All tests produced similar density enhancements to those shown here.

3.4 Resulting Mass Density Profiles and ULX Cusps

The accretion of ambient gas by moving bodies is a classical problem. Many studies have been focused on the flow around compact stars with a point mass potential. Although clusters have much larger masses than individual stars, their potential is relatively shallow and the classical treatment derived for a point-mass potential is only a fair approximation far from the cluster when $GM_c/r_c \gg c_s^2+v^2$. When $GM_c/r_c \lesssim c_s^2+v^2$, the collective potential alters the local gas properties before the gas is accreted onto the individual stars within the cluster.

Figure 5.2 shows the resulting density profiles for star clusters with $GM_c/r_c \sim c_s^2+v^2$ for a variety of core radius and relative motions with respect to the external medium combinations. For small r_c, the potential starts to resemble that of a point mass and, as a result, the density enhancement in the core is very significant. A density enhancement is observed to persist as long as the sound speed or the relative velocity of the ambient medium is greater than the central velocity dispersion of the cluster. The enhanced density profiles within the cluster differ from the classical Bondi solution, and, as depicted in Figure 5.3, are better described by the cluster-Bondi analytic profiles derived by Lin and Murray (2007).

The flow pattern around a star cluster at large relative velocities is multi-dimensional and complex (Figure 5.2). In the frame of the potential, the gas streamlines are bent towards the cluster center. Some shall intersect the center, while others converge along a line behind it. The convergence speed of the gas determines the reduction in its velocity relative to the potential due to shocks, and therefore whether or not the gas is accreted. In line with the conventional treatment, clusters moving with respect to the interstellar medium at increasing supersonic velocities

will have density enhancements that are progressively lower and significantly more offset from the cluster's center. In these cases the aggregate mass accretion rate of the neutron star core is not significantly increased and stars accrete gas as though they move through the external medium independently. Because several gas knots in the Antennae galaxy have velocities relative to the cluster of order the sound speed of the ambient medium, gas within these cluster cores would achieve high densities. Within this environment, accretion by the individual cluster members will be enhanced greatly relative to their rate of accretion directly from the ambient gas.

3.4.1 X-ray Luminosities from Enhanced Accretion Rates

Accretion and emission from the neutron star cluster strongly depends on the radial distribution of both compact remnants and gas. In this model, we calculate the expected X-ray emission from the neutron star core in the cluster using two extreme examples for the radial distribution of compact remnants. The first one is based on Fokker-Planck models of a core collapsed (centrally condensed) globular cluster (Dull *et al.*, 1997b), and the second simply assumes that the neutron stars, containing 1% of the total mass, follow the radial stellar mass distribution. The absorption corrected X-ray luminosities and characteristic emission frequencies of the neutron star cusps are calculated assuming a neutral absorbing medium with solar metallicity. Note that here we consider neutron stars to be magnetic field free. If their fields are strong enough, the propeller effect may reduce the X-ray luminosity of neutron stars (Menou *et al.*, 1999).

Figure 5.5 shows the aggregate X-ray luminosity of the accreting neutron star cluster

as a function of the relative Mach number for both centrally condensed and non-condensed compact remnant distributions. The upper panel shows, for the centrally condensed case, how the absorption corrected X-ray luminosities vary with both photon energy and radial position within the cluster. As argued above, clusters moving with increasing supersonic velocities will have density enhancements that are progressively lower and significantly more offset from the cluster's center. As a result, the aggregate X-ray luminosity rapidly decreases with increasing Mach number (although less sharply for more extended clusters). While the density enhancement increases monotonically with decreasing relative velocity, so does the corresponding photoionization absorption. These two competing effects produce a maximum in the X-ray luminosity of the cluster at about $\mu_\infty = 2$. Most of the luminosity comes from 95% (60%) of all neutron stars in the condensed (non-condensed) core with X-ray luminosities ranging between 2×10^{34} (10^{33}) and 4×10^{34} (2×10^{34}) erg s^{-1}. In this regime, the results depend weakly on the assumed radiation spectra of the individual accreting members.

3.5 Discussion

Many studies have been focused on the flow around compact stars with a point mass potential. Although clusters have much larger masses than individual stars, their potential is relatively shallow. Here we consider the efficiency of accretion in these cluster potentials, and show that when the sound speed or the relative velocity of the ambient medium is less than the central velocity dispersion of the cluster, the collective potential alters the local gas flow before the gas is accreted onto the individual stars within the cluster. Accretion onto these dense stellar

cores at the inferred rate can lead to the onset of ULX sources.

While there are no stellar clusters observed in the Galactic disk which bear these anticipated properties (the relative velocity of the halo clusters to the interstellar medium is in the range of 100 km/s), observations of several cluster knots in the Antennae indicate intracluster relative velocities that comparable to the central velocity dispersions (Whitmore *et al.*, 2005). Based on the results of the current work, we show that accretion by individual compact stars in the core of such systems is enhanced greatly relative to their rate of accretion directly from the ambient gas, and conclude that this process may be relevant for explaining the origin of ULX sources in these extraordinary clusters. Illumination of nearby gas clouds by these sources may also lead to reprocessed infrared, optical and ultraviolet emission. Finally, the sources may leave trails of denser and likely hotter gas behind them as they plough through the gas.

A way to distinguish between an IMBH and an accreting neutron star cusp is via time-dependent observations. The emission from a relativistic region of a IMBH might vary on time-scales of seconds. The emission of a large number of statistically independent black holes and neutron stars should be considerably less variable: $\Delta t \leq r_{\rm c}/c_{\rm s} \sim 10^4$ yr. Observations find that a handful of the X-ray sources in the Antennae galaxy are indeed variable albeit on timescales that are larger than a few years (Zezas *et al.*, 2006). Such variability might be explained if only a moderate fraction of the compact stars dominate the total luminosity. Such compact isolated accretors will probably have unusual time-variability properties as their discs may be much larger than the typical discs of X-ray binaries, and indeed they are missing the perturbing influence of the secondary. On the other hand, accretion disc feeding in these sources will be variable itself, leading to variability on variety of time-scales.

Although accretion disk spectra are notoriously difficult to calculate from first principles, an IMBH and a cluster core may also have observably different spectra. It has been suggested that a cool multicolor disk spectral component, might indicate the presence of an IMBH (Miller *et al.*, 2003). This is understood as following. The larger mass of the BH accretor, the lower the temperature of the inner edge of the disk, which scales as $T_{\rm i} \propto (M_{\rm BH}\dot{M}/r_{\rm i})^{1/4} \propto \dot{M}^{1/4}M_{\rm BH}^{-1/2}$ for a simple thin-disk model. Since for our model, individual neutron star sources have $T_{\rm i} \sim 1$ keV (consistent with observations), then an IMBH might have $T_i \sim 30$ eV. Thus, an association of the ULXs with an IMBH, as opposed to a accreting core of compact remnants, could be made on the basis of a very soft observed spectral component. We know of no reported observations of such components.

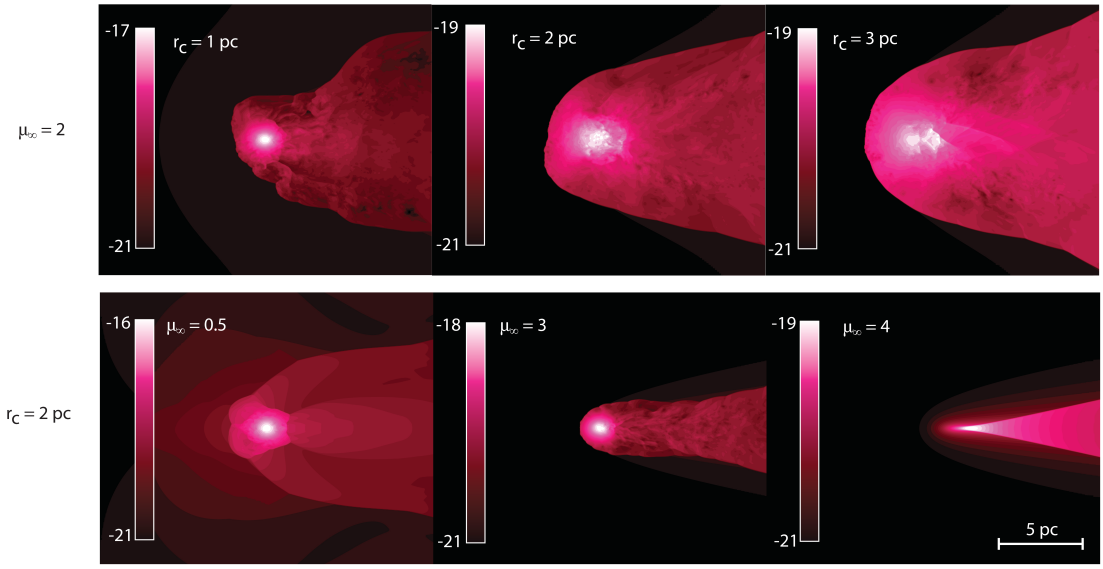

Figure 3.1: The flow pattern around a star cluster set in motion through an initially uniform medium with varying core dimensions (r_c) and relative speeds (μ_∞). Color bars show density cuts through the *xy*-plane in units of $\log(g/cm^3)$.

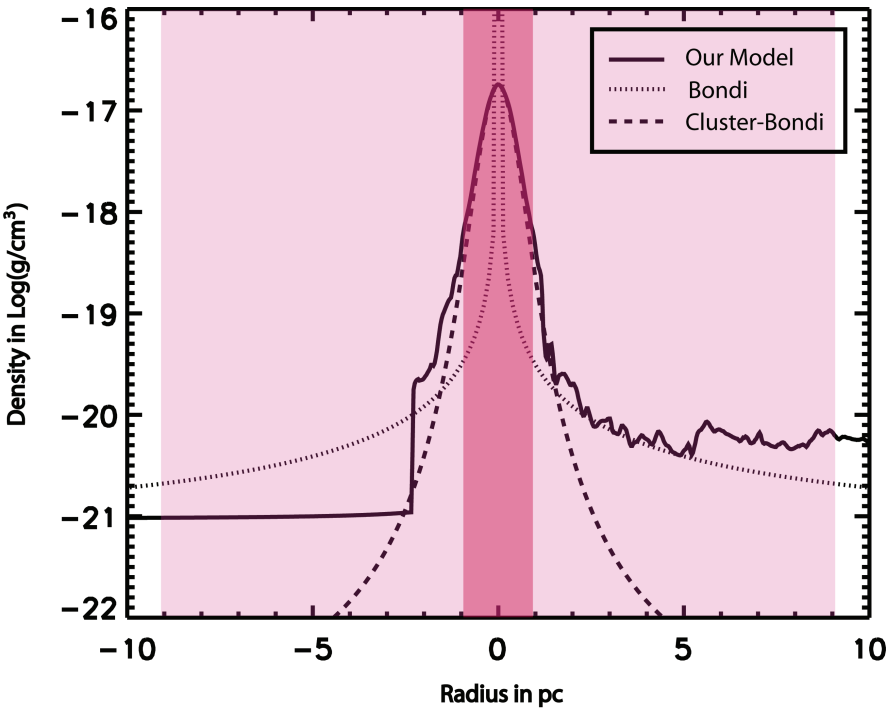

Figure 3.2: Density profile for a model with core radius $r_c = 1$ pc and $\mu_\infty = 2.0$. Solid black line show a cut along the x-axis for the simulated cluster. The the dotted line is the Bondi solution for a stationary point mass, while the dashed line gives the modified Bondi-Hoyle-Lyttleton solution for a cluster potential as derived by Lin and Murray (2007).

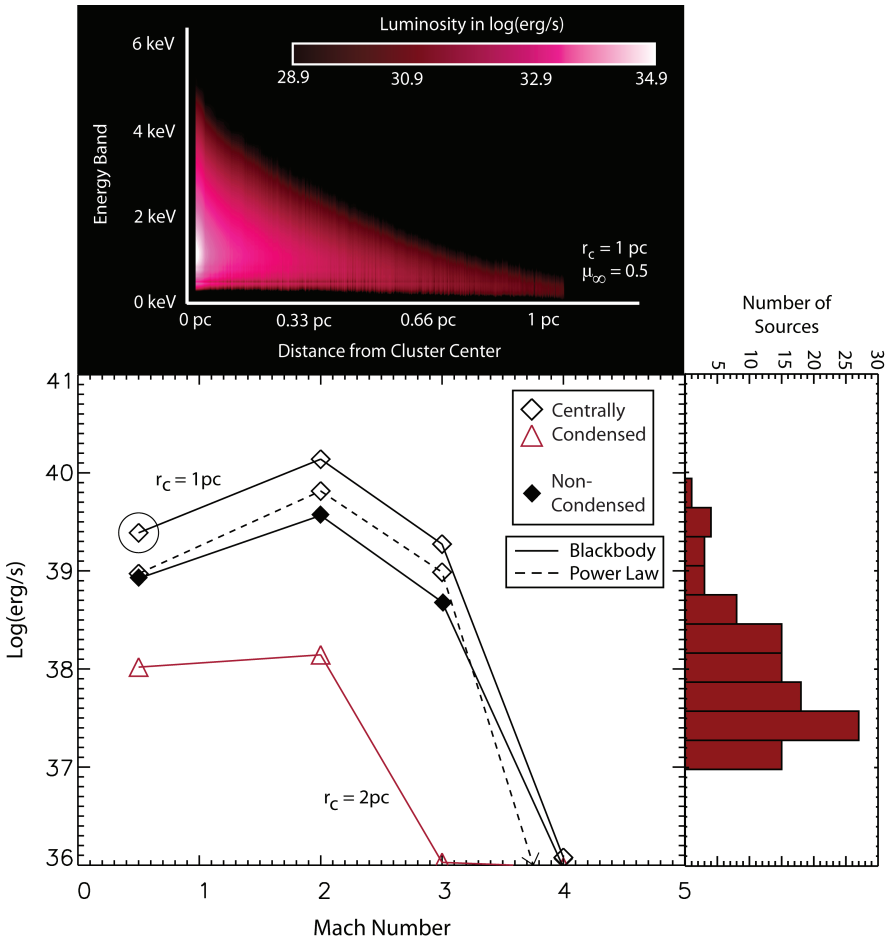

Figure 3.3: X-ray luminosities from enhanced accretion rates. *Center:* The absorption corrected X-ray luminosities from an accreting neutron star core in a star cluster as a function of μ_∞ calculated using two extreme examples for the radial distribution of compact remnants. Triangles are for $r_c = 2\,\mathrm{pc}$ while diamonds are for $r_c = 1\,\mathrm{pc}$. *Upper:* Spectral and luminosity decomposition as a function of distance from the cluster's center for a model with $\mu_\infty = 0.5$, $r_c = 1\,\mathrm{pc}$. *Right:* Luminosity distribution of the X-ray sources in the Antennae galaxy (Zezas *et al.*, 2007).

Chapter 4

The Role of Nuclear Star Clusters in Enhancing Supermassive Black Hole Feeding Rates During Galaxy Merging

4.1 Introduction

Supermassive black holes (SMBHs; $M \gtrsim 10^5 M_\odot$) are inferred to reside in most galactic nuclei (Kormendy and Richstone, 1995; Magorrian *et al.*, 1998b; Shankar, 2009; Laor, 2000; Ferrarese *et al.*, 2006). When efficiently supplied with gas, these objects can produce some of the most luminous sources in the Universe (Falocco *et al.*, 2012; Koss *et al.*, 2012). Recent panchromatic surveys have shown that close dual AGN are comparatively more luminous at high energies than their isolated counterparts, suggesting that the merger process is intricately tied to the feeding history of the waltzing SMBHs (Koss *et al.*, 2012; Liu *et al.*, 2013; Gültekin *et al.*, 2009b,a).

Gas supply to central SMBHs during galaxy mergers directly affects the growth and luminosity of these objects, and therefore, understanding how mass is bestowed to SMBHs results in predictions of their number density and luminosity distribution (Silk and Rees, 1998; Komossa *et al.*, 2003). In cosmological simulations of merging galaxies, some form of the classical Bondi-Hoyle-Lyttleton (BHL) accretion prescription is usually implemented to estimate SMBH feeding rates (Barai *et al.*, 2014; Choi *et al.*, 2012, 2013; Hirschmann *et al.*, 2013; Anglés-Alcázar *et al.*, 2013; Gabor and Bournaud, 2014; Newton and Kay, 2013; Blecha *et al.*, 2013; Li, 2012; Jeon *et al.*, 2012; Fabjan *et al.*, 2010; Kurosawa *et al.*, 2009; Springel *et al.*, 2005). The use of this recipe assumes that the properties of gas at 50-100 pc (generally determined by the resolution scale length) accurately models the mass accretion rate onto the SMBH (Johansson *et al.*, 2009).

A significant fraction of SMBHs are expected to be embedded in nuclear star clusters (NSCs; Böker, 2002; Böker *et al.*, 2004; Böker, 2010; Graham and Spitler, 2009; Walcher *et al.*, 2005; Seth *et al.*, 2010). Because these NSCs are typically more massive than the central SMBH, they can significantly alter the gas flow at scales which are commonly unresolved in cosmological simulations ($\approx 1-5\,\mathrm{pc}$). As a result, NSCs could provide an efficient mechanism for funneling gas towards the central black hole. Accurately determining the mass accretion history of SMBHs has important consequences not only for their growth history, but also the evolution of the host galaxy (Sijacki *et al.*, 2007; Debuhr *et al.*, 2011, 2012; Primack *et al.*, 2008; Booth and Schaye, 2009; Hopkins *et al.*, 2007; King, 2003; Di Matteo *et al.*, 2008; Croton *et al.*, 2006). For this reason, pinning down the dominant mechanism by which gas at large scales is funneled into the SMBH is essential for understanding their role in mediating galaxy evolution.

Here, we use simulations to investigate how the accretion rate of SMBHs might be enhanced during galaxy mergers when they are embedded in massive and compact NSCs. These well-resolved, three dimensional simulations are used to generate sub-grid accretion prescriptions for larger scale simulations, thus providing a more accurate estimate of the feeding rates of SMBHs in cosmological simulations as well as a better determination of the expected luminosities of dual AGNs. This paper is organized as follows. In Section 4.2 we review the commonly used sub-grid prescriptions for calculating the mass accretion rates onto central massive black holes during galaxy merger simulations and suggest a modification in the presence of a NSC. A numerical scheme aimed at calculating black hole growth at high resolution, accounting for the gravitational focusing effects of NSC, is presented in Section 4.3. The conditions necessary for NSCs to collect ambient gas and, in turn, enhance the mass accretion rate of SMBHs are derived in Section 4.4. In Section 4.5 we use the central gas densities from realistic SPH cosmological merger simulations to estimate the augmentation to SMBHs mass accretion rates in the presence of a NSC as a function of time. We summarize our findings in Section 4.6.

4.2 Accretion Flows Modified by the Presence of a NSC

SMBHs can trigger nuclear activity only as long as they interact with the surrounding gas. The way in which gas flows into a SMBH depends largely on the conditions where material is injected. The mass accretion rate into SMBHs in cosmological simulations is commonly estimated using analytical prescriptions based on the large scale gas structures in the centers of the simulated merging galaxies. The BHL formalism assumes the gas is accreted spherically

symmetrically (Johansson *et al.*, 2009):

$$\dot{M}_{\rm BHL} = 4\pi (GM)^2 \rho_\infty (v^2 + c_{\rm s}^2)^{-3/2}, \tag{4.1}$$

where v is the relative velocity of the object through the external gas whose sound speed and density are given by $c_{\rm s}$ and ρ_∞, respectively (Edgar, 2004).

The flow pattern is dramatically altered if the inflowing gas has a small amount of angular momentum. If the inflowing gas is injected more or less isotropically from large r, but has specific angular momentum per unit mass such that $l^2/GM \gg r_{\rm g}$, then the quasi-spherical approximation will break down and the gas will have sufficient angular momentum to orbit the SMBH (here $r_{\rm g}$ is the SMBH's Schwarzschild radius). Viscous torques will then cause the gas to sink into the equatorial plane of the SMBH. In recent works, such departures from spherical symmetry have been accounted for by assuming the accretion proceeds through a disk:

$$\dot{M}_\nu = 3\pi\alpha\Sigma c_{\rm s}^2 \Omega^{-1} \tag{4.2}$$

where Σ is the surface gas density of the disk, Ω is the rotational angular frequency, and α is a dimensionless parameter dictating the strength of turbulent viscosity in the disk (Debuhr *et al.*, 2011, 2012). Both prescriptions rely on an understanding of the gas properties at $r \gtrsim 100$ pc in order to determine the mass accretion rate onto the central SMBH.

As discussed in Naiman *et al.* (2009, 2011), a NSC moving at a low Mach number through relatively cold gas can drastically increase the gas density in its interior with respect to

that of the external medium. Simple analytical estimates suggest that in the central regions of a NSC the expected density enhancement is given by

$$\frac{\rho(r=0)}{\rho_\infty} \approx \left[1+\frac{GM_{\rm c}(\gamma-1)}{c_\infty^2 r_{\rm c}}\right]^{1/(\gamma-1)}, \tag{4.3}$$

where the core radius, $r_{\rm c}$, is related to the cluster velocity dispersion by $\sigma_V^2 \approx GM_{\rm c}/r_{\rm c}$. The gas properties characterized here by ρ_∞ and c_∞ are the density and sound speed at $r \gg r_{\rm c}$. Here γ denotes the adiabatic index of the flow and $M_{\rm c}$ designates the mass of the NSC (Naiman *et al.*, 2011). Given this density enhancement in the core of the NSC, the accretion rate of the embedded SMBH would be amplified by a factor of $\dot{M}_{\rm c} \propto \rho(r=0)/c_{\rm s}^3(r=0)$ where $c_{\rm s}(r=0) = c_{\rm s,nsc}$ is the sound speed of the gas within the NSC and we have assumed that accretion proceeds at the classical Bondi rate (Bondi, 1952).

This simple derivation has thus far assumed a stationary cluster, however, the supermassive black hole and nuclear star cluster complex (SMBH+NSC) is likely to move with respect to its surrounding gas during a merger. We thus modify our analytical accretion rate prescription following the formalism discussed in Ruffert (1994a) and Ruffert and Arnett (1994) such that:

$$\dot{M}_{\rm c} = \lambda\pi R_{\rm b}^2 \rho_{\rm nsc} c_{\rm s,nsc} \tag{4.4}$$

where $R_{\rm b} = 2GM_{\rm BH}c_{\rm s,nsc}^{-2}$ is the classic Bondi radius with $c_{\rm s,nsc} = K\gamma\rho_{\rm nsc}^{\gamma-1}$, $\lambda \approx 1$ is a dimension-

less parameter that depends on the size of the accretor, and

$$\frac{\rho_{\rm nsc}}{\rho_\infty} = \max\left\{\left(1+\frac{GM_{\rm c}[\gamma-1]}{c_\infty^2 r_{\rm c}[1+\mu_\infty^2]}\right)^{\frac{1}{\gamma-1}}\left(\frac{\mu_\infty^2}{\mu_\infty^2+1}\right)^{\frac{3}{2}},1\right\} \tag{4.5}$$

where $\rho_{\rm nsc}$ is the modified density in the NSC's interior. Here the Mach number of the SMBH+NSC complex with respect to the large scale surrounding gas is given by $\mu_\infty = v_\infty/c_\infty$. In this formalism, the motion of the SMBH+NSC complex with respect to the ambient medium does not result in a sizable decrease in the amount of gas retained in the cluster's core as in the classical BHL case. This is because equation 4.5 accounts for the protection provided by the large scale NSC which forms a quasi-hydrostatic envelope around the SMBH (Naiman *et al.*, 2011). The presence of a compact and massive NSC could then significantly increase the gas densities surrounding central SMBHs during galaxy mergers thereby enhancing their accretion rates. The degree by which the accretion rate is enhanced by the presence of a NSC is tested with numerical simulations in the remaining of the Chapter.

4.3 Simulating Accretion onto SMBHs embedded in NSCs

To examine the ability of a NSC to collect ambient gas and, in turn, enhance the mass accretion rate onto the central SMBH, we simulate the SMBH+NSC complex as a gravitational potential with a central sink term moving through ambient gas with FLASH, a parallel, adaptive mesh refinement hydrodynamics code (Fryxell *et al.*, 2000a). A smooth potential, given by

$$\Phi = \frac{GM_{\rm c}}{(r^2+r_{\rm c}^2)^{1/2}}, \tag{4.6}$$

provides an accurate description of the NSC potential given the cluster mass, M_c, and radius, $r_c = 2\sigma_V^2 G M_c / 3^{3/2}$ (Pflamm-Altenburg and Kroupa, 2009). We use inflow boundaries to simulate the NSC's motion through the central galaxy medium. The SMBH sink sizes are within hundredths of sonic radii,

$$r_s = \frac{2GM_{bh}}{c_\infty^2(1+\mu_\infty^2)} \tag{4.7}$$

in order to accurately resolve the mass accretion rate onto the black hole (Ruffert, 1994a; Ruffert and Arnett, 1994). Models are run from an initially uniform background until a steady density enhancement forms within the NSC, which usually takes tens to hundreds of core sound crossing times. Convergence tests with higher refinement and longer run times produce models which show similar central densities and mass accretion rates to those depicted here. We compute both models with adiabatic ($\gamma = 5/3$) and nearly isothermal ($\gamma = 1.1$) equation of states in order to test the effects of cooling.

To adequately resolve the small scale sink along with the significantly more extended NSC's core, and the even larger scale flow structures that develop around the cluster, a sizable level of refinement is required on the AMR grid. As the minimal time step in our simulation is determined by the gas flow on small scales, necessary runtimes would need to be prohibitively large in order to simulate a resolved sink and the large scale gas structure until a steady state density enhancement forms within the NSC. Instead, we construct the accretion rates onto our model BH+NSC systems from a set of three simulation setups, as depicted in Figure 4.1.

The first of these simulations, labeled *initial* in the density contours and mass accretion rate plots shown in Figure 4.1, is a small scale simulation which follows the gas flow as the

central density enhancement begins to form in the NSC core while simultaneously tracking the mass accretion rate onto the fully resolved central sink. Once the large scale bowshock begins to interact with the boundaries of the computational domain (at about three to five core sound crossing times) the simulation is halted. We concurrently simulate the same initial setup in a larger box (about fifty core radii) at a lower resolution and follow the density build up within the NSC's core without the presence of a sink. We label this simulation as *no sink* in Figure 4.1. Because the presence of a sink has a minimal effect on the build up of mass in the core, the central density in the large scale simulation albeit lower resolution agrees well with central density evolution observed in the *initial* simulation. While there is no explicit sink in these second set of simulations, the mass accretion rate onto a central black hole can be relatively accurately inferred from the gas properties within the NSC's core as shown in Figure 4.1. Once a steady state density enhancement has formed in the central regions of the NSC, these large scale simulations are then refined further until a central sink is resolved by at least 16 cells. This level of refinement was chosen to allow the the unsteady mass accretion rate to converge, as argued by Ruffert and Arnett (1994). We refer to these simulations as *steady state* in Figure 4.1.

The set of simulations shown in Figure 4.1 depicts the gas flow around a compact nuclear star cluster in a slowly moving isothermal gas. However, the enhancement in the black hole's accretion rate depends on the thermodynamical conditions of the surrounding gas as well as on the properties of the NSC. The remainder of this Chapter is devoted to calculating the necessary conditions for large central density enhancements in the centers of SMBH+NSC systems and determining whether or not these conditions persist during a galaxy merger.

4.4 Necessary Conditions for Accretion Rate Enhancements

In order for the gravitational potential of the NSC to alter the local gas flow before it is accreted onto the central SMBH, the NSC must be moving relatively slowly through cold gas; a condition shown in Naiman *et al.* (2011) to be equivalent to requiring that

$$\sigma_V^2 > c_s^2 + v^2. \tag{4.8}$$

Typical cluster velocity dispersions in observed NSCs are found to be $\sigma_V \approx 50 - 300\,\mathrm{km\,s^{-1}}$ and are similar in magnitude to both the sound speed of the surrounding gas and the relative gas velocities of SMBHs during galaxy mergers (Debuhr *et al.*, 2011, 2012). As a result, the conditions necessary for efficient mass accumulation are commonly satisfied, an assertion that we will quantify making use of detailed, galaxy merger simulations.

Figure 4.2 shows how the accretion rate onto a SMBH is modified by the presence of a NSC satisfying $\sigma_V \approx c_s^2 + v^2$. In all calculations, the flow is assumed to behave adiabatically. Without the presence of a NSC, the bowshock penetrates close to the sink boundary. However, in the presence of a NSC, the bowshock forms at the outer boundary of the cluster's core. As discussed in Lin and Murray (2007) and Naiman *et al.* (2011), this effectively mitigates the effects of the gas motion on the central sink and the accretion proceeds as a nearly radial inward flow. This added protection results in a moderate mass accretion rate enhancement onto the central sink, which are slightly larger for more compact NSC. As the flow accumulates in the NSC's potential, a quasi-hydrostatic envelope builds up around the central sink, whose central density increases with the compactness of the NSC. For an adiabatic flow, this density

enhancement is accompanied by an increase in the sound speed of the flow such that $\dot{M}_{\rm nsc} \propto \rho_{\rm nsc}/c^3_{\rm s,nsc} \approx \rho_\infty/c^3_\infty$. As a result, the accretion rate for a stationary sink is not expected to be aided by the increase in central density in an adiabatic flow. The moderate increase in mass accretion rates for an adiabatic flow, produced mainly by changes in the flow structure, is shown by both our analytical (see equations 4.4 and 4.5) and simulation results.

On the other hand, the central density enhancement enabled by the presence of a NSC when $\sigma_V \approx c_{\rm s}^2 + v^2$ can be accompanied by a drastic increase in mass accretion rate if the gas is permitted to cool. This allows the central density to grow without a mitigating increase in the local sound speed of the gas. In the near isothermal ($\gamma = 1.1$) calculations depicted in Figure 4.2, we have $c_{\rm s}(r) \approx c_\infty$ and the presence of a NSC results in an enhancement of about an order of magnitude in the mass accretion rate onto the central sink. Here, the accretion rate fluctuates around a mean value, as the isothermal gas can collapse to much smaller scale structures than in the adiabatic case, providing the central sink with much larger temporal changes in the amount of accreted gas.

Figures 4.2 and 4.3 together demonstrate the important effects that both the equation of state and the compactness of the NSC can have on the mass accreted by the central SMBH. In what follows, we make use of cosmological simulations to estimate the range of gas and NSC properties conducive to large enhancements in the mass accretion rate onto the central SMBHs during galaxy mergers.

4.5 The Accretion History of SMBHs in Galaxy Mergers

The majority of galaxies (50−70%) are expected to harbor nuclear star clusters (Neumayer, 2012), and therefore large enhancements in accretion rates onto SMBHs are possible during typical galaxy mergers when conditions are favorable (i.e. $\sigma_V \approx c_s^2 + v^2$). If, in addition, during the merger the gas in the central regions cools efficiently, the increase in the mass accreted by the SMBH can be significant. To determine if and when these conditions are satisfied during a merger we plot the gas properties in the central core regions of galaxies computed in merger simulations by Debuhr *et al.* (2011) in Figure 4.4. This range of sound speeds and densities represent the average values of a subset of particles within the accretion radii, defined as four times the simulation's gravitational softening length: $R_{\rm acc} \approx 188$ pc (Debuhr *et al.*, 2011, 2012). To estimate the average properties of the gas (c_∞, v_∞, ρ_∞) flowing toward the SMBH we use only particles within a 30° conical region in front of the SMBH's velocity vector. While the average gas parameters are relatively insensitive to the exact value of the opening angle of the cone, the amount of inflowing gas is slightly underestimated using this method as it ignores the material which can be accreted from behind the direction of motion of the SMBH.

Given the estimated average properties of the gas flow at large scales, we expect the effects of the NSC in altering the mass accretion history of the central SMBH to be most prominent when the gas is able to cool efficiently, as argued in Section 4.4. In a merger simulation, the condition for efficient cooling is established when the sound crossing time across the accretion radius is longer than the cooling time of the gas: $t_{\rm cs,acc} \gtrsim t_{\rm cool}$. If this condition holds, the cold gas can be significantly compressed and, as a result, lead to a large density enhancement in the

core of the NSC.

We can estimate the accretion radius of the SMBH as

$$t_{\rm cs,acc} = \frac{2GM_{\rm bh}}{c_\infty^3(1+\mu_\infty^2)} \tag{4.9}$$

where $\mu_\infty = v_\infty/c_\infty$ is the Mach number of the large scale flow. The cooling time can be written as $t_{\rm cool} = \epsilon/[n_e n_H \Lambda(T,Z)]$, where ϵ is the internal energy of the gas, Λ is the cooling rate of the gas at a temperature T and metallicity $Z = 10^{-2}\,Z_\odot$, and n_e and n_H are the electron and neutral hydrogen number densities, respectively. In galaxy merger simulations, the condition $t_{\rm cs,acc} \gtrsim t_{\rm cool}$ is generally satisfied (Figure 4.4) although for a particular run, the average gas properties can fluctuate between the cooling and non-cooling regimes as the merger progresses. This is illustrated in the simulation snapshots *A*, *B* and *C* taken from the *fidNof* model of Debuhr *et al.* (2011), which are depicted in Figure 4.4. As a consequence, there may be times during the galaxy merger when cooling rates within the accretion radius are high and the mass accretion rate can be heavily augmented by the presence of a NSC, provided that $\sigma_V \approx c_\infty$.

Since we are not treating the feedback from the black hole explicitly, we use both adiabatic (inefficient cooling; efficient feedback) and isothermal (efficient cooling; inefficient feedback) simulations to illustrate the effects of the surrounding NSC on the gas flow as a whole and the importance of the $\sigma_V \approx c_\infty$ condition. Figure 4.5 shows the gas in the inner regions of a model where $\sigma_V < c_\infty$. Here, a moderately massive black hole ($M_{\rm bh} = 10^6\,M_\odot$) with and without a surrounding NSC ($M_{\rm c} = 10^7\,M_\odot$ and $\sigma_v = 115\,{\rm km/s}$) propagates through a background medium with $c_\infty = 200{\rm km/s}$ and $\rho_\infty = 10^{-23}\,{\rm g\,cm^{-3}}$ (similar to the gas properties

found in simulation snapshot *C* of Figure 4.4). Because $\sigma_V < c_\infty$, the gas flow around the SMBH is not altered by the presence of the NSC and the mass accretion rates change only minimally between the model with and without the NSC, even when cooling is efficient. This is corroborated by the results of the near isothermal and adiabatic simulations, which are shown in Figure 4.5.

When the SMBH+NSC complex propagates into a region in parameter space where cooling is efficient and the condition $\sigma_V \gtrsim c_\infty$ is satisfied, the presence of a NSC can dramatically increase the mass supply onto the black hole. Figure 4.6 shows the gas flow in the inner regions of a NSC where cooling is predicted to be efficient. Similar to Figure 4.5, the SMBH+NSC complex is characterized by $M_{\rm bh} = 10^6\,M_\odot$ and $M_{\rm c} = 10^7\,M_\odot$ ($\sigma = 115\,{\rm km/s}$) but in this case it propagates through a background medium with $c_\infty = 100$ km/s and $\rho_\infty = 10^{-21}\,{\rm g\,cm^{-3}}$ (similar to those found in simulation snapshot *A* of Figure 4.4). Under these conditions, the presence of a NSC can result in a large mass feeding rate increase when compare to the case without a NSC, in particular when the gas cools efficiently. This is evident when comparing the evolution of the mass accretion rate calculated in the adiabatic and near isothermal simulations. We note here that in both regimes, the prescription laid out by equations (4.4) and (4.5) provides a relatively good estimate of the steady state mass accretion rate onto the SMBH (see Figures 4.5 and 4.6). In what follows, we will assume the validity of such prescription in order to estimate the growth history of SMBHs in galaxy mergers.

To establish the mass feeding history of merging SMBHs embedded in NSCs, we use the gas properties in the central regions of simulated merging galaxies. Figure 4.7 shows how the growth history of the central SMBHs, as derived from the *fidNof* simulation of Debuhr

et al. (2011), is altered by the presence of a NSC. In both galaxies, a NSC with $M_c = 10^7 M_\odot$ is assumed to reside in each galactic center at the start of the simulation. These values are consistent with observations of NSC around SMBHs (Graham and Spitler, 2009; Graham *et al.*, 2011). The calculation assumes that the flow is able to cool efficiently ($\gamma = 1.1$) and that the NSC is unable to grow as the mass of the SMBH increases. At early times, the presence of the NSC enables the central SMBH to grow quicker than it would do if it was in isolation. As the galaxy merger progresses and the mass of the SMBH increases above M_c, the gravitational influence of the cluster ceases to be relevant.

Despite having only a brief impact, this early growth spurt induced by the presence of a NSC results in a vastly different growth and feeding history for the merging SMBHs. We find that the initial properties of the NSC have an enduring effect on the luminosity and mass assembly history of merging SMBHs. We note here that we have assumed that the NSC's mass remains unchanged during the entire simulation. If a larger stellar concentration is able to form around the growing SMBH, then the evolving NSC could have a longer lasting impact.

4.6 Summary and Conclusions

An understanding how matter can be funneled to galactic nuclei is essential when constructing a cosmological framework for galaxy evolution. When modeling galaxy evolution, an implementation of a sub-grid mass accretion prescription to estimate the gas flow onto SMBHs is required for the sake of computational efficiency. In simulations of merging galaxies, some form of the classical Bondi-Hoyle-Lyttleton (BHL) accretion prescription is usually im-

plemented to estimate the SMBH's feeding rate. This prescription assumes that the properties of gas at hundreds of parsecs accurately determine the mass accretion rate. In this Chapter we argue that NSCs, a common component of galactic centers, can provide an efficient mechanism for funneling gas towards the SMBH at scales which are commonly unresolved in cosmological simulations.

For the conditions expected to persist in the centers of merging galaxies, the resultant large central gas densities in NSCs should produce enhanced accretion rates onto the embedded SMBHs, especially if cooling is efficient. Because these NSCs are typically more massive than the central SMBH, they can significantly alter the gas flow before being accreted. While the model shown in Figure 4.7 results in a modest increase in the final mass of the merged SMBH, the presence of NSCs result in faster SMBH growth rates and higher bolometric luminosities than predicted by the standard BHL formalism. Obviously, the calculation are incomplete and should improve with a self-consistent implementation of feedback.

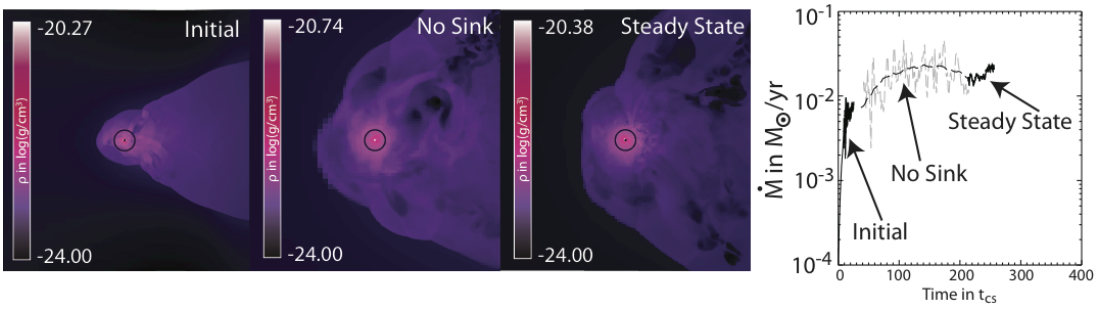

Figure 4.1: Density contours of the flow pattern around a SMBH+NSC system moving through a uniform density, near isothermal ($\gamma = 1.1$) medium for three different simulation setups. The *initial* simulation is a small scale calculation that resolves how the gas flow starts to accumulate within the NSC core and accretes onto the fully resolved central sink. The *no sink* simulation is a low resolution, large scale calculation without a sink that captures the gas build up in the NSC core until a steady state is reached. The *steady state* simulation is a large scale calculation that includes an embedded sink once a steady state central density has been realized. The bottom line plot shows the mass accretion rate for the three different simulation setups as a function of the sink's sound crossing time: $t_{cs} = r_s/c_s$. Common to all calculations are $M_{bh} = 10^8\,M_\odot$ and $M_c = 10^9\,M_\odot$. The Plummer core radius, $r_c = 5.3$ pc is denoted by a black open circle and the sink size $r_s = 0.5$ pcis denoted by a black filled circle. The sound speed in all simulations is set to $c_\infty = 214\,\mathrm{km/s}$, and Mach number is $\mu_\infty = 1.64$. Snapshots from left to right correspond to times $t_{cs} = 130$, 221, and 250.

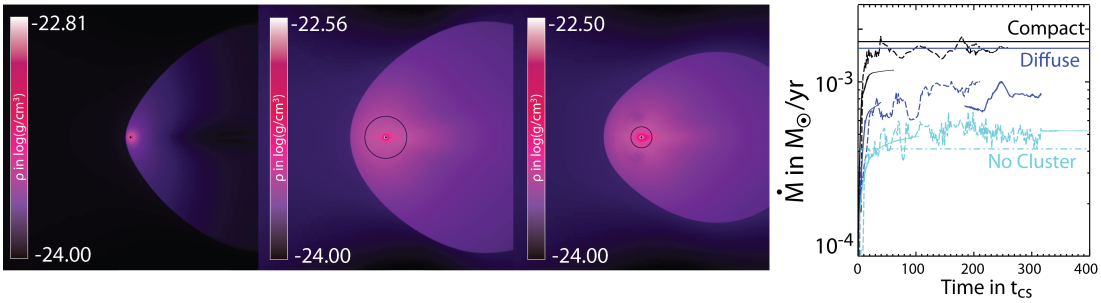

Figure 4.2: Density contours of the flow pattern around a SMBH with $M_{\rm bh} = 10^8\,M_\odot$ moving through a uniform density medium characterized by $\gamma = 5/3$. Simulation snapshots are plotted for a naked SMBH (*left*), a SMBH embedded in a diffuse NSC (*middle*) and a SMBH embedded in a compact NSC (*right*) together with the mass accretion rate history in each system, which is calculated using the three different simulation setups discussed in Figure 4.1. The effect of the NSC's velocity dispersion ($M_{\rm c} = 10^9\,M_\odot$) can be seen by comparing the gas flow between the diffuse ($r_{\rm c} = 5.3$ pc) and compact ($r_{\rm c} = 10.6$ pc) clusters. The horizontal *dot-dashed* line shows the analytical prescription for Bondi-Hoyle-Lyttleton accretion onto the naked SMBH from Ruffert and Arnett (1994) and the *dark blue* and *black* horizontal lines show our modified prescription for the mass accretion rate in the presence of a NSC. All sink sizes are $r_{\rm s} = 0.5$ pc. Here, the sound speed and Mach number are $c_\infty = 263\,{\rm km/s}$ and $\mu_\infty = 1.33$, respectively. The snapshots from left to right are at times $t_{\rm cs} = 112$, 108, and 81.

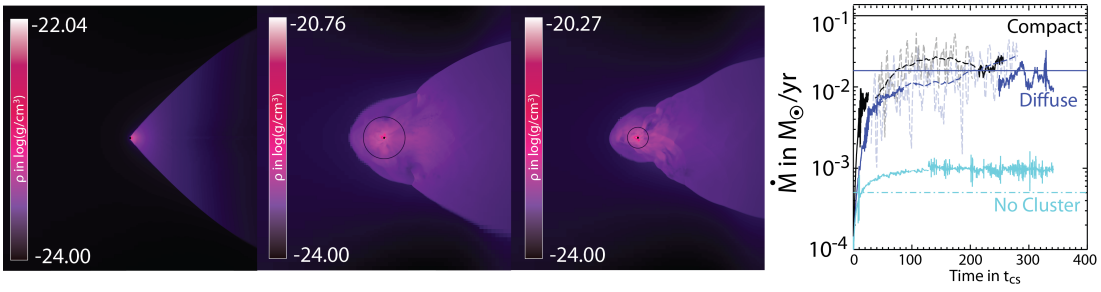

Figure 4.3: Similar to Figure 4.2 but for a near isothermal ($\gamma = 1.1$) medium. The snapshots from left to right are at times $t_{\rm cs} = 130$, 134, and 131.

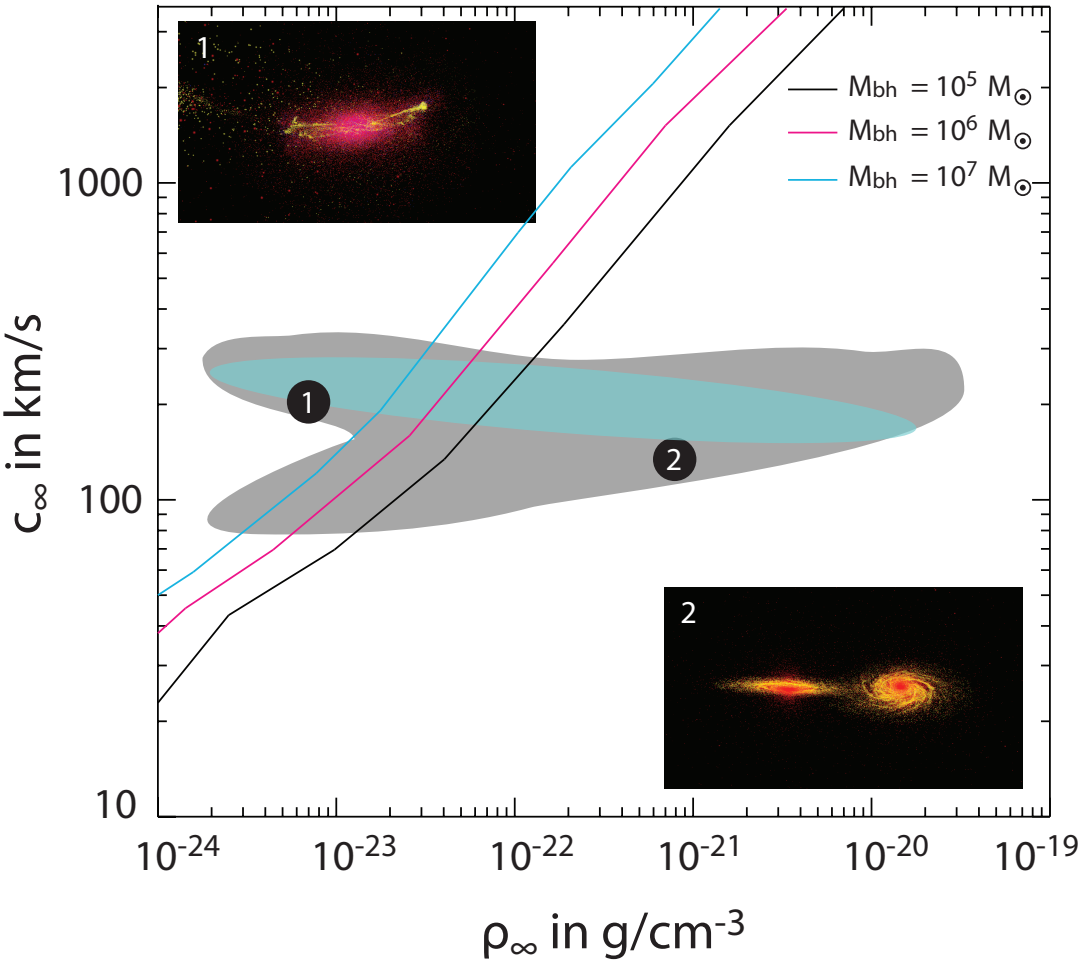

Figure 4.4: The range of sound speeds, c_∞, and densities, ρ_∞, from the gas surrounding a naked SMBH in the galaxy merger models of Debuhr *et al.* (2011). The *gray* contour denotes the combinations of $[c_\infty,\rho_\infty]$ for their entire suite of models while the *blue* contour shows the range for their *fidNof* model. The locations in the $[c_\infty,\rho_\infty]$ plane for three different simulation snapshots (*A*, *B*, *C*) taken from the *fidNof* model of Debuhr *et al.* (2011) are highlighted. The plotted lines correspond to the condition $t_{\rm cool} = t_{\rm cs,acc}$ for three different values of $M_{\rm bh}$.

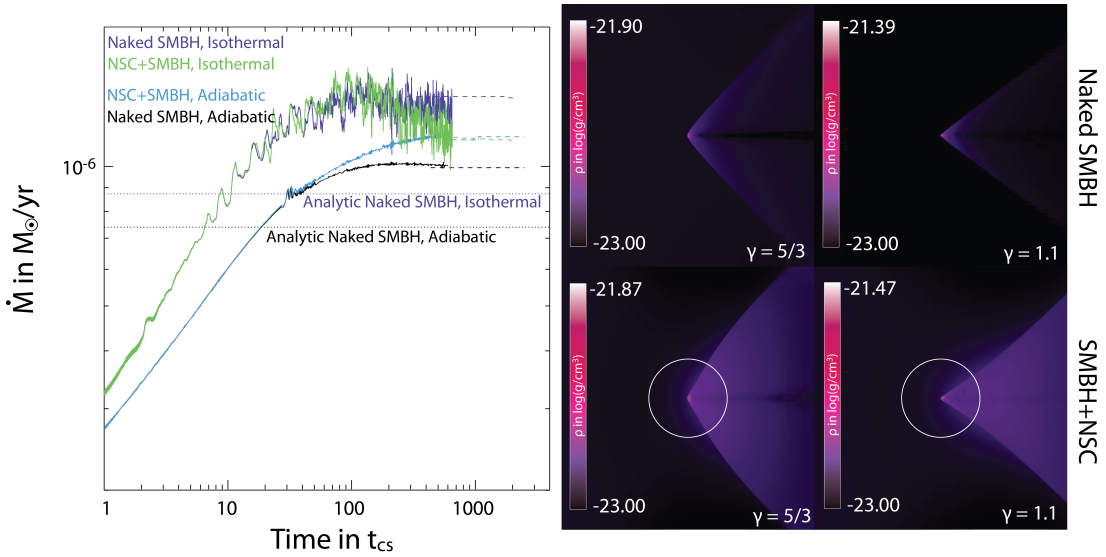

Figure 4.5: A $M_{\rm bh} = 10^6\,M_\odot$ black hole with and without a surrounding NSC ($M_{\rm c} = 10^7\,M_\odot$ and $\sigma_V = 115$ km/s) propagates with $\mu = 1.5$ through a background medium with $c_{\rm s} = 200$ km/s and $\rho_\infty = 10^{-23}\,{\rm g\,cm^{-3}}$ (similar to the gas properties found in simulation snapshot *C* of Figure 4.4). The *left* panel shows the mass accretion rate of models with and without a NSC for adiabatic ($\gamma = 5/3$) and near isothermal gas ($\gamma = 1.1$) flows, which are calculated using different simulation setups as discussed in Figure 4.1. Under these conditions, $\sigma_V < c_\infty$ and the gas flow around the SMBH is not altered by the presence of the NSC. As a result, the change in mass accretion rate between the model with and without the NSC is negligible, even when cooling is efficient. Cluster radii are shown as white circles.

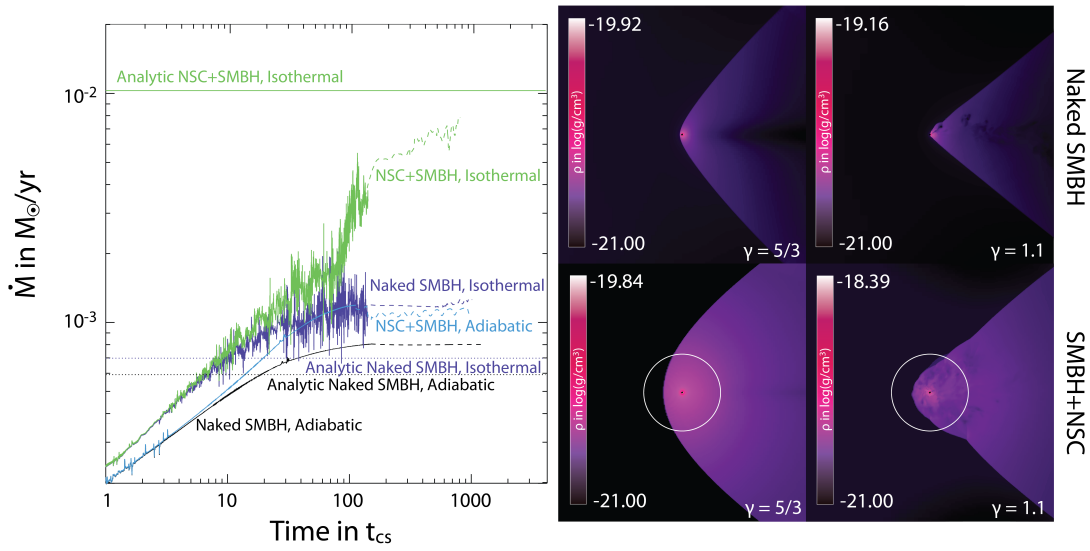

Figure 4.6: Similar to Figure 4.5 but in this case the black hole propagates through a background medium with $c_\infty = 100$ km/s and $\rho_\infty = 10^{-21}\,\mathrm{g\,cm^{-3}}$ (similar to those found in simulation snapshot *A* of Figure 4.4). Because $\sigma_V < c_\infty$, the presence of a NSC can result in a large mass feeding rate increase when compare to the case without a NSC, in particular when the gas cools efficiently ($\gamma = 1.1$). Once again, the accretion rate onto the SMBH is calculated using different simulation setups as illustrated in Figure 4.1.

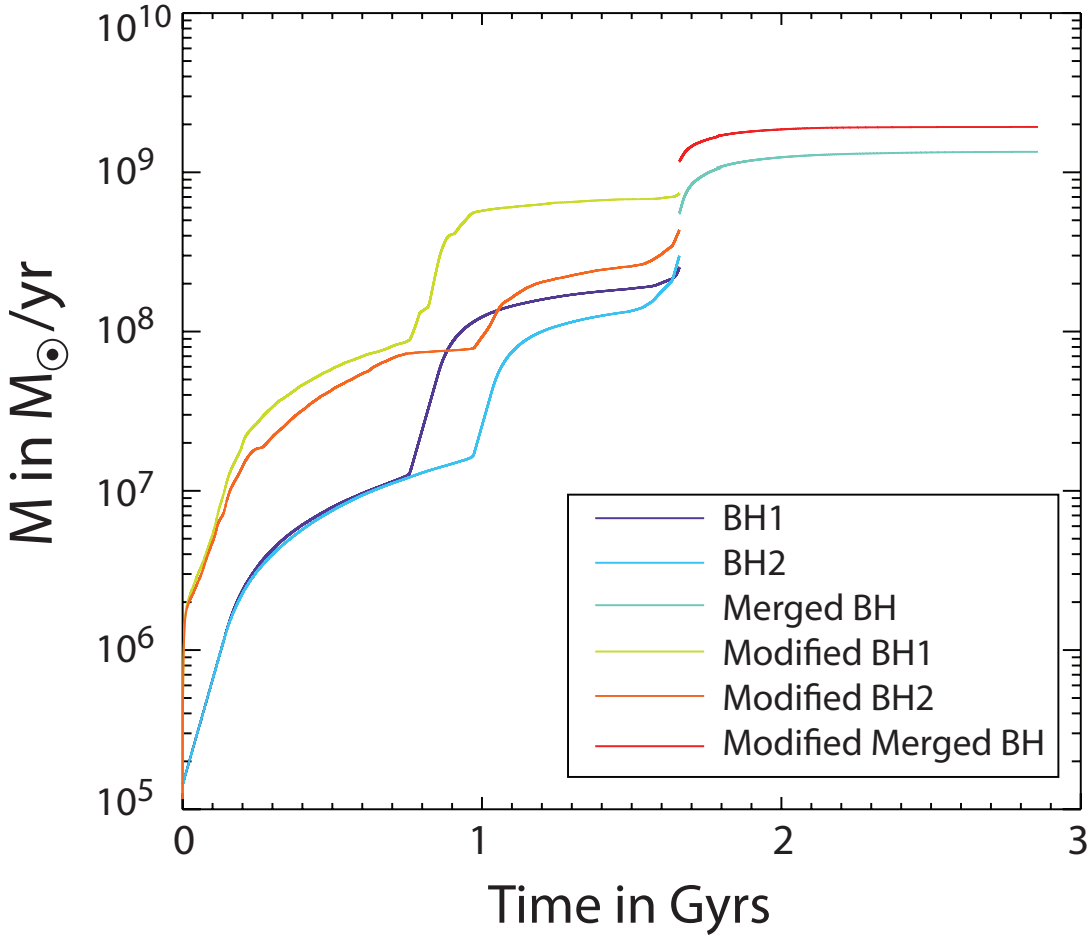

Figure 4.7: The growth history of the two central SMBHs in the merging galaxy model *fidNof* of Debuhr *et al.* (2011). The prescription laid out by equations (4.4) and (4.5) is used to estimate the steady state mass accretion rate onto the SMBH, which in turn use the gas properties as derived by the SPH simulations. A NSC characterized by $M_c = 10^7\,M_\odot$ and $\sigma_V = 180\,\mathrm{km/s}$ (Graham and Spitler, 2009; Graham *et al.*, 2011, consistent with observations of SMBH+NSC systems) is assumed to reside in each galactic center at the start of the simulation. The calculation assumes that the flow is able to cool efficiently ($\gamma = 1.1$) and that the mass of the NSC is fixed. As the galaxy merger evolves and the mass of the SMBHs increase above M_{nsc}, the gravitational influence of the NSC stops being relevant.

Chapter 5

Stellar Wind Mass Retention in Star Clusters: Implications for Subsequent Episodes of Star Formation

5.1 Introduction

The idea that stars in globular clusters (GCs) are a coeval population has been a long disputed topic with significant discussion devoted to the presence (or lack thereof) of multiple main sequences and subgiant branches (see Piotto, 2009b, for a review). However, recent observational evidence has demonstrated that these multiple stellar populations (MSPs) are not only ubiquitous but also make up a sizable fraction ($\sim$40-60%) of the total stellar mass (Caloi and D'Antona, 2007; D'Antona and Caloi, 2008). Spectroscopic observations of MSPs in GCs have also unveiled differences in their light element abundances (see e.g. Gratton *et al.*, 2004; de Silva *et al.*, 2009; Martell and Smith, 2009). These anomalies can only be produced if these

MSPs were formed from material processed at temperatures $T > 10^7$K (D'Ercole *et al.*, 2008; Renzini and Voli, 1981; Ventura and D'Antona, 2008).

To explain the presence of MSPs with the observed abundance anomalies the following timeline has been identified (Conroy and Spergel, 2011; Cottrell and Da Costa, 1981; Smith, 1987; Carretta *et al.*, 2010b): after the first generation of stars is formed and intracluster gas is expelled by supernovae, matter processed in the interiors of AGB stars is returned to the ISM through winds and after several 100 Myrs a second generation of stars is formed from a mixture of stellar-processed material and captured ISM gas. Some of the issues at the forefront of attention include the type and age of stars able to process gas at the required internal temperatures while at the same time efficiently returning material into GCs to form a sizable mass fraction of new stars. We address both of these issues here.

The effective retention of stellar wind material to create MSPs of comparable mass presents a challenge to the current understanding of GC formation (Conroy, 2012). Accounting for the inflow and mixing of pristine ISM material slightly lowers the retained mass requirements, however the original GCs still need to be significantly more massive than those currently observed (Naiman *et al.*, 2011; Pflamm-Altenburg and Kroupa, 2009; D'Ercole *et al.*, 2010; Conroy and Spergel, 2011).

Despite their relevance, stellar wind gas retention has so far only been studied for a very restricted number of systems (D'Ercole *et al.*, 2008, 2010; Conroy, 2012; Conroy and Spergel, 2011), with a parametric study of the role of cluster mass and compactness performed using only a limited range of structural parameters (Vesperini *et al.*, 2010). Here we expand upon these studies with detailed hydrodynamical simulations which investigate not only a wide

range of cluster mass and compactness parameters but also stellar age as well as the importance of the stellar wind prescriptions and metallicity in determining the optimum parameter space for effective gas retention. In addition, we also investigate the role of extended heating sources, such as pulsar winds or accretion onto the compact stellar members, in preventing gas from being adequately confined.

5.2 Numerical Methods and Initial Setup

5.2.1 Hydrodynamics

To examine the ability of clusters to effectively retain the winds emanating from their evolving stellar members, we simulate mass and energy injection in isolated core potentials under the assumption of spherical symmetry (Quataert, 2004; Hueyotl-Zahuantitla *et al.*, 2010). The one-dimensional hydrodynamical equations are solved using FLASH, a parallel, adaptive mesh refinement hydrodynamical code (Fryxell *et al.*, 2000a). The winds from the closely packed stellar members are assumed to shock and thermalize such that density and energy contributions can be treated as source terms in the hydrodynamical equations. In spherical symmetry, these equations can be written as (Holzer and Axford, 1970; Hueyotl-Zahuantitla *et al.*, 2010):

$$\frac{\partial \rho}{\partial t} + \frac{1}{r^2}\frac{\partial}{\partial r}\left(\rho u r^2\right) = q_m(r,t) \tag{5.1}$$

$$\frac{\partial u}{\partial t} + u\frac{\partial u}{\partial r} + \frac{1}{\rho}\frac{\partial P}{\partial r} = -\frac{d\Phi_g}{dr} - q_m(r,t)u \tag{5.2}$$

$$\frac{\partial \varepsilon}{\partial t} + \frac{1}{r^2}\frac{\partial}{\partial r}\left(\varepsilon u r^2\right) + P\frac{\partial u}{\partial r} = q_\varepsilon(r,t) - Q(r) \tag{5.3}$$

where $P = P(r)$, $\rho = \rho(r)$, $u = u(r)$ and $\varepsilon = \varepsilon(r)$ are the gas density, pressure, radial velocity and internal energy density, respectively. Here, $Q(r) = n_i(r)n_e(r)\Lambda(T,Z)$ is the cooling rate for gas with ion and electron number densities $n_i(r)$ and $n_e(r)$, and $\Lambda(T,Z)$ is the cooling function for gas at temperature T and metallicity Z. We use $\Lambda(T,Z)$ from Gnat and Sternberg (2007) for $T > 10^4$ K and Dalgarno and McCray (1972) for $10 \leq T \leq 10^4$ K.

The $q_m(r,t)$ and $q_\varepsilon(r,t)$ terms in equations (6.4)-(6.6) are used here to mediate the total rate of mass and energy injection at a time t in a cluster's history. For N stars each with average mass loss rate **at time** t **of** $\langle \dot{M}(t) \rangle$ and wind energy injection rate $\frac{1}{2}\langle \dot{M}(t) \rangle \langle v_{\rm w}(t)^2 \rangle$ we have $\dot{M}(t)_{\rm w,total} = N\langle \dot{M}(t) \rangle = \int 4\pi r^2 q_m(r,t) dr$ and $\dot{E}(t)_{\rm w,total} = \frac{1}{2}N\langle \dot{M}(t) \rangle \langle v_{\rm w}(t)^2 \rangle = \int 4\pi r^2 q_\varepsilon(r,t) dr$, such that $q_\varepsilon(r,t) = \frac{1}{2} q_m(r,t) \langle v_{\rm w}(t)^2 \rangle$. For simplicity, we neglect the effects of mass segregation and assume $q_m(r,t) \propto n(r)$ such that $q_m(r,t) = A(t) r^{-2} \frac{d}{dr}\left(r^2 \frac{d\Phi_g}{dr}\right)$. Here, $A(t) = \langle \dot{M}(t) \rangle / (4\pi G \langle M_\star \rangle)$ with the average mass of a star given by $\langle M_\star \rangle$. We also neglect the effects of external mass accumulation, which can be an important source of gas when clusters reside in cool, dense ISM gas (Naiman *et al.*, 2009, 2011). If the cluster's velocity dispersion is large compared to the wind velocity, shock heating of the gas caused by the motion of the stars could be important. However, as we show, this effect is minor for the star cluster parameters considered here. While other specific heating sources such as photoionization or supernova are not explicitly included,

the overall effects of additional energy injection in the cluster are discussed in §5.4.

The stellar cluster gravitational potentials are modeled as Plummer models (Brüns *et al.*, 2009a; Pflamm-Altenburg and Kroupa, 2009)

$$\Phi_g = -\frac{GM_c}{\left[r^2 + r_c^2(\sigma_v)\right]^{1/2}} \tag{5.4}$$

for a given total mass, M_c, and velocity dispersion, $\sigma_v = \left(3^{3/4}/\sqrt{2}\right)^{-1}\sqrt{GM_c/r_c}$. While the shape of the potential can have an effect on the radial distribution of gas inside the core (Naiman *et al.*, 2011), the overall amount of gas accumulated in the cluster is relatively unchanged by the exact form of its potential. In addition to following the dynamics of the gas under the influence of Φ_g, the self gravity of the gas is computed using FLASH's multipole gravity module. We fix our resolution to 6400 radial cells for each model. The resolution within the computational domain is set by the core radius, r_c, to ensure that we are adequately resolving the core and that the cluster's potential is effectively zero at the outer boundary.

In cases where catastrophic cooling occurs, we assume star formation is triggered if the collapsing gas's Jean's length is smaller than the central resolution element, or if $t_{\rm cool} \lesssim t_{\rm dyn}$. To estimate the gas evolution during the star forming period, our cooling prescription is modified following Truelove *et al.* (1997) by turning off energy losses and allowing the gas to evolve adiabatically. Such a method approximates the transition of an isothermally collapsing cloud to an optically thick, adiabatically evolving protostellar cluster while forgoing the computationally expensive three dimensional radiative transfer calculations required to treat this problem accurately. Because we do not include an explicit star formation prescription, we allow such

unstable regions to evolve for a few sound crossing times before halting the simulation.

5.2.2 Stellar Evolution

The final ingredients to be specified in our simulations are the time dependent average mass loss rates and wind velocities, which in turn determine the mass and energy injection rates, q_m and q_ε. Because our simulations are spherically symmetric, these rates must encompass the average mass loss properties of the stellar population as a whole.

5.2.2.1 The Turn Off Approximation

To estimate the net mass loss and mean thermal velocities of the colliding winds, we first follow the formalism developed by Pooley and Rappaport (2006) where the integrated wind kinetic energy and mass loss of the stellar population's turn off star is used as a proxy for the average wind velocity and mass loss rate:

$$\langle v_{\rm w,to}^2 \rangle \approx \frac{2\Delta E_K}{\Delta M} \tag{5.5}$$

$$\langle \dot{M}_{\rm to} \rangle \approx \frac{\Delta M}{\Delta t}. \tag{5.6}$$

Here $\Delta E_K = \frac{1}{2}\int_{t_0}^{t_1} \dot{M}_{\rm to} v_{\rm w,to}^2 dt$ and $\Delta M = \int_{t_0}^{t_1} \dot{M}_{\rm to} dt$ are the kinetic energy and mass loss input rates integrated over the lifetime of the turn-off stars, $\Delta t = t_1 - t_0$, where t_0 is the zero age main sequence (ZAMS) and t_1 is the end of the AGB phase, white dwarf stage, or compact object creation. This provides a reasonable estimate for the overall wind mass and energy supply to the cluster although it fails to capture the variability of realistic stellar winds which are currently

not well constrained (Marigo, 2012a; Wood *et al.*, 2005; Cohen, 2011).

5.2.2.2 The Population Averaged Approximation

The effects of the additional input of mass and kinetic energy by stars with $M_\star < M_{\star,\mathrm{to}}$, which are neglected in the formalism we just outlined, can be included by convolving the above definitions of the average mass loss rate and wind velocity with an initial mass function (IMF) and a star formation history. Following Kroupa *et al.* (2013a), the average number of stars in a mass interval $[M_\star, M_\star + dM_\star]$ evolving between $[t, t+dt]$ is given by $dN = \zeta(M_\star, t) N_\star b(t) dM_\star dt$ where $\zeta(M_\star, t)$ is the IMF, which we assume is accurately described by the Kroupa (2001) IMF, $b(t)$ is the normalized star formation history, and $N_\star$ is the total number of stars. For a non-evolving IMF, $\zeta(M_\star, t) = \zeta(M_\star)$, with a mass distribution extending from masses $M_{\star,L}$ to $M_{\star,H}$, the normalized star formation history can be written as $1/t_{\mathrm{age}}(M_{\star,L}) \int_0^{t_{\mathrm{age}}(M_{\star,L})} b(t) dt = 1$, where $t_{\mathrm{age}}(M_\star)$ is the lifetime of a star of a given $M_\star$. Examples of $b(t)$ include a constant star formation rate, $b(t) = 1$, or a coeval population, $b(t) = \delta(t - t_0)$, with all stars formed at t_0.

The average mass $\langle \Delta M(t_i) \rangle$ and kinetic energy $\langle \Delta E_K(t_i) \rangle$ injected into the cluster environment at a time t_i, by a population of stars with $M_\star \epsilon [M_{\star,L}, M_{\star,H}]$ and whose birth rate is regulated by $b(t)$, are then given by

$$\langle \Delta M(t_i) \rangle = \int_{t_0}^{t_i} b(t) \int_{M_{\star,\mathrm{L}}}^{M_{\star,\mathrm{H}}} \zeta(M_\star) \dot{M}(M_\star, t) dM_\star dt \tag{5.7}$$

and

$$\langle \Delta E_K(t_i) \rangle = \frac{1}{2} \int_{t_0}^{t_i} b(t) \int_{M_{\star,\mathrm{L}}}^{M_{\star,\mathrm{H}}} \zeta(M_\star) \dot{M}(M_\star, t) v_w^2(M_\star, t) dM_\star dt, \tag{5.8}$$

respectively. Stars that have lifetimes $t_{\rm age}(M_\star) < t_i$ forsake the stellar population unless they were born during the most recent star formation time interval $[t_i - t_{\rm age}(M_\star), t_i]$. For this reason, t_0 is set to $\max[0, t_i - t_{\rm age}(M_\star)]$. This formalism allows for equations (6.10) and (6.11) to be cast into a more general form for the average mass loss rates and wind velocities at a specific stellar population life-time, t_i:

$$\langle \dot{M}(t_i) \rangle = \frac{\langle \Delta M(t_i) \rangle}{t_i} = \frac{1}{t_i} \int_{t_0}^{t_i} b(t) \int_{M_{\star,\rm L}}^{M_{\star,\rm H}} \zeta(M_\star) \dot{M}(M_\star, t) dM_\star dt \tag{5.9}$$

and

$$\langle v_w^2(t_i) \rangle = \frac{2\langle \Delta E_K(t_i) \rangle}{\langle \Delta M(t_i) \rangle} = \langle \dot{M}(t_i) \rangle^{-1} \int_{t_0}^{t_i} b(t) \int_{M_{\star,\rm L}}^{M_{\star,\rm H}} \zeta(M_\star) \dot{M}(M_\star, t) v_w^2(M_\star, t) dM_\star dt. \tag{5.10}$$

In what follows, we assume the stellar population initially residing in star clusters is coeval such that $b(t) = \delta(0)$, which provides an accurate description for clusters with $t_i \gtrsim 10$ Myrs.

To compute the individual mass loss rates $\dot{M}(M_\star, t)$ and wind velocities $v_w(M_\star, t)$ we use the MESA stellar evolution models (Paxton *et al.*, 2011). We use MESA to follow the evolution of a grid of stellar models with $M_\star = 0.1\,M_\odot$ - $20\,M_\odot$ from ZAMS to either the white dwarf stage, end of the AGB phase, or compact object creation. The mass loss rates during the crucial AGB phase are estimated in MESA using the wind prescription of Bloecker (1995), $\dot{M}_B = 1.93 \times 10^{-21} \eta_B (M/M_\odot)^{-3.1} (L/L_\odot)^{3.7} (R/R_\odot)\, M_\odot \mathrm{yr}^{-1}$, with a normalization of $\eta_B = 0.04$ consistent with LMC measurements (Ventura *et al.*, 2000) and with previous studies (D'Ercole *et al.*, 2008, 2010; Conroy and Spergel, 2011). We note here that AGB mass loss models are still being

developed and no exact mass loss rates have been agreed upon (Ventura and D'Antona, 2008; Karakas and Lattanzio, 2007; Marigo, 2012a). The wind velocity is approximated as the escape velocity, accurate within a factor of a few across a wide range of masses and life stages (Abbott, 1978; Evans *et al.*, 2004; Schaerer *et al.*, 1996; Nyman *et al.*, 1992; Vassiliadis and Wood, 1993; Loup *et al.*, 1993; Dupree and Reimers, 1987; Debes, 2006; Badalyan and Livshits, 1992). The Reimers (1975) prescription, $\dot{M}_R = 4 \times 10^{-13} \eta_R (M/M_\odot)^{-1} (L/L_\odot)(R/R_\odot) M_\odot \mathrm{yr}^{-1}$, $\eta_R = 1.0$, is used in MESA to estimate the mass loss during the RGB branch and main sequence lifetime. As depicted in Figure 5.1, this prescription provides a reasonable estimate for the mass loss rates of low mass main sequence stars where we can also approximate $\dot{M}_{MS} \approx 10^{-12} (M/M_\odot)^3 M_\odot \mathrm{yr}^{-1}$. We fix $Z = 1/10 Z_\odot$ for most models although the effects of changing the metallicity are discussed in §5.4.

5.3 Stellar Wind Retention in Star Clusters

The mass injection properties, characterized here by the mass loss rates and wind velocities emanating from a coeval population of stars, change dramatically as the population evolves. Figure 5.2 shows the evolution of the average stellar wind parameters. As the wind velocities and stellar mass loss rates change, so does the ability of a cluster potential to retain the shocked stellar wind gas. Figure 5.2 clearly illustrates the differences between efficient (population averaged prescription which includes the kinetic energy injected by main sequence stars) and inefficient (turn off mass prescription which does not include the kinetic energy injected by main sequence stars) thermalization and mixing of stellar winds from stars of different masses.

Note that the differences between the turn off mass and population averaged prescriptions manifest themselves predominately in the values of the population's averaged wind velocity as main sequence stars do not contribute to the total mass injection rate.

Figure 5.2 depicts the wind properties as a function of time throughout the cluster's evolution. If the cluster has its gas removed by, for example, ram pressure stripping due to interaction with external gas (Priestley *et al.*, 2011) or by additional gas heating processes, gas retention will commence without memory of any previous episode of mass accumulation. If however, the cluster potential is assumed to be non-evolving and isolated with no additional heating sources operating other than stellar winds, the gas retention properties at a particular age will depend on the mass and energy injection history of the stellar members. We refer to these two extreme scenarios as mass retention without memory and with memory, respectively.

A young star cluster without gas retention memory, corresponding to time A in Figure 5.2, with its high average wind velocity cannot retain gas effectively if $\sigma_v \ll v_w$. This is clearly seen in Figure 5.3 which shows the properties of the shocked stellar wind gas confined to a cluster potential characterized by $\sigma_v = 30\,\mathrm{km/s}$ and $M_c = 10^7\,M_\odot$ for both turn off mass and population averaged prescriptions (*red* curves). The flow in this case was evolved for $t_i = t_A =$ 23 Myrs as the average mass loss rates and wind velocities do not change appreciably over this time period. A young cluster is thus only able to retain a small quantity of high temperature gas in its inner region ($M_{\rm acc}/M_{\rm c} \approx 10^{-7}$), while further away gas is blown out of the system in a wind.

As the cluster members evolve, a dramatic decrease in the average wind velocity occurs due to the dominant contribution of the slow, dense AGB winds to the overall mass

injection, corresponding to time *B* in Figure 5.2. For the star cluster, here assumed to be characterized by a non-evolving gravitational potential, the AGB contribution results in stellar wind injection parameters that favor significant mass retention, as shown in Figure 5.2 (*black* curves). As the stellar wind gas shocks and cools, mass is efficiently accumulated ($M_{\rm acc}/M_{\rm c} \approx 0.04$) until the central region becomes Jeans unstable, thus triggering star formation. In this case, the gas flow within the cluster is evolved until $t = t_{\rm sf}$, defined here as the sound crossing time within the (adequately resolved) Jeans unstable region. Here $t_{\rm sf}$ = 1200 Myrs and 1700 Myrs for the turn-off mass prescription and population averaged approximation, respectively.

As the cluster ages, remaining stars no longer pass through an extended thermally pulsing AGB phase. This results in a dramatic increase in average wind velocity and decrease in average mass loss rates as seen at time *C*. As a result, the cluster potential is unable to effectively retain the emanating gas and the remaining wind material flows out of the cluster almost unrestrained ($M_{\rm acc}/M_{\rm c} \approx 10^{-7}$).

The amount of gas in clusters in which stellar wind material is efficiently retained, as in time *B* of Figure 5.2, can increase significantly if the cluster is not stripped of gas prior to this time by additional internal heating sources or by external gas removal. In this case the cluster can retain the memory of previous gas accumulation. Figure 5.4 compares the hydrodynamical profiles and central gas mass accumulation histories of two clusters in which mass retention is assumed to take place with and without memory. In both cases, star formation is triggered albeit at different times and involving different amounts of accumulated cold gas. The larger central gas density in the model with memory results in a few percent increase in cold gas made available for a second generation of star formation - $M_{\rm acc}/M_{\rm c}$ increases from 4.3% to 6.9%

when the mass retention takes place with memory.

The ability for a star cluster to retain wind ejecta depends not only on the evolutionary stage of its members but also on their spatial distribution. To illustrate this, in Figure 5.5 we show the properties of the shocked stellar wind gas confined to a shallow potential characterized by $\sigma_v = 14\,\mathrm{km/s}$ and $M_c = 4.5 \times 10^5\,M_\odot$, parameters thought to accurately represent the current stellar mass distribution in M15 (McNamara *et al.*, 2004; Gerssen *et al.*, 2002). A shallow gravitational potential is thus unable to retain a significant amount of stellar wind material, even during the AGB phase. This is observed to also be the case in simulations in which the cluster is assumed to have gas retention memory. The observational constraint on the allowed gas density in M15 (Knapp *et al.*, 1996b) is consistent with our predictions for the present state of the gas in this system.

The dramatic difference observed in Figures 5.3 - 5.5 between the stellar wind mass accumulated in cluster potentials of varying properties motivates our study to compare results obtained with different velocity dispersions and cluster masses for clusters with and without gas retention memory. To facilitate comparisons, we first systematically vary the cluster velocity dispersion for a fixed total mass $M_c = 10^7\,M_\odot$, assuming the turn off mass wind velocity and mass loss rate are representative of the entire population and the cluster has no gas retention memory. The left panel of Figure 5.6 gives the amount of accumulated stellar wind mass in units of M_c for a range of cluster velocity dispersions and different evolutionary stages (t_i) of the stellar members. By looking at the shaded regions in Figure 5.6, the reader can identify the cluster velocity dispersion and mass combinations for which favorable conditions for star formation are satisfied at a given cluster age provided there is no memory of gas retention.

Cluster potentials with $\sigma_v \lesssim 20\,\mathrm{km/s}$ are not effective at retaining gas in their cores, and gas is blown out of the cluster at all times. This is consistent with the results of Smith (1999), who estimate an upper limit of $\sigma_v \lesssim 22\,\mathrm{km/s}$ for main sequence stellar winds to effectively remove gas from Galactic globular clusters. As the velocity dispersion increases above $30\,\mathrm{km/s}$, the cluster core is able to retain the shocked and efficiently cooled stellar wind gas, making the central region Jeans unstable before (i.e. $t_{\mathrm{sf}} \ll t_i$) a significant amount of mass is accumulated into the cluster. The largest fraction of mass retained takes place for star clusters with $\sigma_v \approx 25\,\mathrm{km/s}$. In this case, the potential is steep enough to retain the shocked and subsequently cooled wind material, but shallow enough to force the cold gas to collapse only until a significant amount of mass has been accumulated. The contours in the left panel of Figure 5.6 show that potentials with $\sigma_v \gtrsim 30\,\mathrm{km/s}$ may endure multiple episodes of star formation albeit involving less retained gas, while potentials with $25\,\mathrm{km/s} \lesssim \sigma_v < 30\,\mathrm{km/s}$ can have only short but more intense star formation periods. However, because we do not treat star formation explicitly, future detailed simulations are needed to address the possibility of recurrent star formation in these systems. The largest mass accumulation for a single star formation episode occurs for $\sigma_v \approx 27\,\mathrm{km/s}$ between the ages of $1-10$ Gyrs, with a mass retention fraction of $M_{\mathrm{acc}}/M_c \approx 6.4\%$. This value is lower than the $\approx$10% estimated by previous studies (Conroy, 2012; D'Ercole *et al.*, 2008), owing to the fact that we used the time averaged values of the wind velocity which results in about five times larger kinetic energy injection rates than using the instantaneous AGB wind loss rates.

The extension of the star formation region in Figure 5.6 depends dramatically on the velocity dispersion of the cluster. While our optimal single star formation episode takes place

between cluster ages of $1-10$ Gyrs, significant levels of star formation can occur at earlier times for higher velocity dispersions. For the $\approx 300-400$ Myrs age spreads seen in many LMC and globular clusters (Mackey *et al.*, 2008; Goudfrooij *et al.*, 2009), we find approximately 3% of the original cluster mass can be retained provided $\sigma_v \gtrsim 30\,\mathrm{km/s}$. This suggests that globular clusters with extended episodes of star formation may have been more compact as well as more massive in the past.

The inset panel in Figure 5.6 shows the effects of including the cluster velocity dispersion in the energy injection term (equation 6.6). In compact clusters, this extra energy injection term slightly delays star formation until enough mass has been accumulated in the central regions to cool efficiently and subsequently trigger star formation. However, for less compact clusters ($\sigma_v \lesssim 35\,\mathrm{km/s}$) this additional heating is not important. The slight changes to the mass retention contours when the cluster velocity dispersion is included as an additional energy source can be explained by comparing the rates of energy injection arising from stellar motion induced shocks and stellar winds. The energy injection rate for shocked gas of density ρ_g around a star of mass $M_\star$ is given by $\dot{E}_\mathrm{s} \approx (1/2)\rho_\mathrm{g}\sigma_v^2\Re$. Here, the gas interaction rate at the bow shock generated by the moving star, $\Re = \sigma_v\Sigma$, can be estimated from the bow shock radius of the star (Wilkin, 1996), $\Sigma \approx \pi R_0^2 = \pi\dot{M}v_w/(4\rho_g\sigma_v^2)$. Assuming the energy injection from a star's stellar wind is given by $\dot{E}_\mathrm{w} = (1/2)\dot{M}v_w^2$, then the ratio of injection rates can be written simply as $\dot{E}_\mathrm{s}/\dot{E}_\mathrm{w} \approx \sigma_v/(4v_w)$. Thus, appreciable changes in the heating rates caused by the motion of the stars are only expected when when the cluster velocity dispersion is larger than $4v_w$.

The right panels of Figure 5.6, in conjunction with the left panel, allows us to estimate the amount of stellar wind material retained by a star cluster of a given age, mass and

velocity dispersion. While our models do not span the full range of $M_c - \sigma_v$ combinations, some generalizations can be made from the results presented in Figure 5.6. The conclusions drawn are based upon the assumption that the cluster potential properties, whose evolution causes are poorly known, remain relatively unaltered for $\min[t_i, t_{sf}]$ and that the cluster has no gas retention memory. The right panel of Figure 5.6 is self-explanatory - heavier star clusters at a fixed velocity dispersion retain more gas. The mass retention fraction is observed to increase slightly with augmenting cluster mass as a result of less efficient cooling, which in turn delays the triggering of star formation as mass continues to accumulate. As the proto-globular cluster evolves, the assumption of a static potential used in Figure 5.6 brakes down, however the effects of a time varying potential can be estimated by altering the trajectory of a cluster in the [σ_v, time] or [M_c, time] plane.

Using the average wind velocity and mass loss rate of the turn off mass star to represent the properties of the entire population underestimates the kinetic energy input arising from the more numerous, lighter stars (Figure 5.2). This gives an optimistic value of the wind retention and star formation efficiencies. The effects of using the total kinetic energy input from the star cluster to calculate effective mass retention are shown in Figure 5.7. Direct comparison with Figure 5.6 shows that although the overall mass accumulation is rather similar, in the population-averaged prescription star formation is triggered over a narrower range of velocity dispersions. Not only are higher velocity dispersions required to produce efficient star forming models, but the additional kinetic energy inhibits star formation in the largest mass accumulation regions. This is because the larger wind velocities keep the gas at higher temperatures, thus quenching star formation. Previous studies used the instantaneous AGB wind velocity as

proxy for the total kinetic energy being injected into the cluster. Our results suggest that the inclusion of the kinetic energy provided by the main sequence stellar winds can dramatically alter the gas dynamics in these systems. However, the ability of stellar winds from different populations to mix and effectively thermalize remains uncertain and a clear understanding of their combined effects will require detailed multidimensional simulations, which are currently beyond the scope of this work.

The effects additional kinetic energy injection by main sequence stars in star clusters can be mitigated by the larger densities and thus enhanced cooling rates present in models where gas retention is allowed to proceed unimpeded throughout the cluster's evolution. Figure 5.8 depicts the effects of gas retention with memory on the central mass accumulations and star formation histories of a $M_c = 10^7\,M_\odot$ cluster for a variety of velocity dispersions. Note that our rudimentary treatment of star formation prevents us from following the gas evolution once star formation has been triggered, resulting in an incomplete coverage of the M_c-σ_v plane in Figure 5.8. In Figure 5.8, the largest mass accumulation coincides with the lower σ_v bound of the star formation region. The continuous accumulation of gas also produces larger central gas masses, with a gas mass of up to 9% of the cluster's mass retained. A comparison between the mass accumulation contours in Figure 5.8 with those in the left panel of Figure 5.6 should provide the reader with some understanding of the importance of gas retention memory although such comparison should be done with care, as the assumption of a non-evolving potential in Figure 5.8 is certainly not a good approximation.

While the assumed wind prescription can alter the total amount of gas retained which can create new stars, the contours in Figures 5.6 - 5.8 suggest that a stellar cluster with favorable

potential parameters, $[M_c, \sigma_v]$, can trigger star formation over a large span of time. In reality, an episode of star formation will trigger subsequent supernova outbursts which can drive gas away from the central regions of the cluster, deterring further star formation. We simulate the effects of supernova explosions on gas retention by adding thermal energy to the central region of a typical cluster once star formation has been triggered. To maximize the effects of feedback in our cluster, we assume a large star formation efficiency of 90%, creating $M_\star \approx 10^6\,M_\odot$ in second generation stars for a model from the left panel of Figure 5.6 with a 6.4% retention rate. Following the method of D'Ercole *et al.* (2008), we add in $E_{SN} = 10^{51}\,\mathrm{ergss}^{-1}$ in the central regions of our simulation at a rate of $2 \times 10^{-6}\mathrm{yr}^{-1}$. This has been scaled from their supernova type Ia rate of $2 \times 10^{-5}\,\mathrm{yr}^{-1}$ for a $M_c = 10^7\,M_\odot$ population (Marcolini *et al.*, 2006). After a period of 100 Myrs the supernova energy injection is halted and the gas is once again allowed accumulate in the central regions of the cluster, starting the cycle over. Figure 5.9 shows this cycle of mass accumulation, star formation and supernova feedback for a simulation at $t_{age} \approx 2000\,\mathrm{Myrs}$ for a model with $M_c = 10^7\,M_\odot$, $\sigma_v = 26\,\mathrm{km/s}$, and $M_{\mathrm{acc}}/M_{\mathrm{c}} = 6.4\%$. Here, it takes approximately 2000 Myrs for the cluster to re-trigger star formation once gas has been removed by 100 Myrs of type Ia supernova feedback. Furthermore, once new stars are form they will loose mass, altering the population averaged mass loss rates and wind velocities. Extended episodes of star formation, as are likely to taken place in clusters with large velocity dispersions, would lead to an increase in the mass loss rates and wind velocities at later times from those shown in Figure 5.2.

In estimating the effects of star formation episodes in Figures 5.6 - 5.8, we assume

that such events do not effect the average stellar mass loss parameters dramatically. This approximation will hold true provided that number of stars form during these episodes is small, as suggested by our work. In such cases, the shaded regions depicted in Figures 5.6 - 5.8 provide valid constraints on the star formation ages and masses expected from stellar wind retention.

5.4 Discussion

Throughout this work, we have used simplified models to determine how effective a star cluster of a particular age is at retaining gas emanating from its stellar members, under the assumption that its potential remains unaltered during the simulated phase. We have further assumed a single metallicity for all clusters and have disregarded any heating sources besides supernova feedback and the stellar winds themselves. In this section we relax both of these assumptions.

5.4.1 Metallicity

Cluster to cluster variations in light element abundances are commonly observed (Caldwell *et al.*, 2011; Beasley *et al.*, 2005). These variations may cause changes in the mass loss histories of the individual stellar members and the cooling properties of the shocked gas. As the stellar mass loss prescription are mostly independent of metallicity during the evolutionary time periods that are conducive to star formation ($0.1\,\mathrm{Gyrs} \lesssim t_i \lesssim 100\,\mathrm{Gyrs}$) (Bloecker, 1995), we account for the effects of varying metallicity solely in the cooling function. Figure 5.10 shows the effects of changing metallicity for a typical star forming cluster, described here

by $M_c = 10^7\,M_\odot$, $\sigma_v = 50\,\mathrm{km/s}$, and $t_i = 212\,\mathrm{Myrs}$. As the metallicity is decreased, the cooling becomes less efficient and more material is allowed to flow into the center of the cluster before catastrophic cooling occurs. This enables relatively more massive star forming episodes to be triggered. Interestingly, when metallicity is decreased beyond $Z < 10^{-1}$, the cooling becomes weak enough to prevent catastrophic cooling at times $\leq t_i$. These results suggest that the range of cluster parameters over which large central densities will persist before catastrophic cooling takes place (Figures 5.6 - 5.8) will depend on the metallicity of the emanating stellar winds, though, as illustrated in Figure 5.10, the differences are not marked.

5.4.2 Intercluster Heating Sources

In addition to altering the cooling curves, the inclusion of additional cluster heating sources may prevent effective gas retention in our simulations. We address this problem here by artificially increasing the energy input rate: $q_{\epsilon,\mathrm{new}} = (1+H)q_\epsilon = (1+H)\frac{1}{2}q_m(r)v_w^2$. Under this assumption, the additional heating sources follow the potential's stellar distribution. Figure 5.11 shows the effects of the additional heat input in one of our otherwise star forming simulations. For $H < 2.0$, the gas in the simulation still collapses, triggering star formation. For larger values, on the other hand, the cluster is unable to effectively retain the gas and, as a result, star formation never ensues. By integrating $q_{\epsilon,\mathrm{new}}$ over the cluster's core for $H = 2.0$, we derive the total energy input rate required to overturn the central mass build up, which for this simulation is about $10^{35}\,\mathrm{ergs}^{-1}$.

In many cases, the additional energy injection sources might not follow the stellar distribution. As an example, let's compare the heat distribution expected from accreting neutron

stars under the assumption that the accretion feedback is proportional to the Bondi accretion rate: $q_{\epsilon,\mathrm{ns}} \propto \dot{M} \propto \rho(r)T(r)^{-3/2}$ (Bondi and Hoyle, 1944). Using the volume-averaged density and temperature in the cluster core, $\bar{\rho} \approx 10^{-22}\,\mathrm{g\,cm^{-3}}$ and $\bar{T} \approx 10^{4}\mathrm{K}$, we derive the average luminosity of a single, accreting neutron star: $L_{NS} \approx 10^{33}\,\mathrm{ergs\,s^{-1}}$. This implies that $\gtrsim 100$ accreting neutron stars are required to reside in the cluster's core in order to significantly offset its cooling properties. However, to accurately test this phenomena a multi-dimensional approach would be required as feedback would not necessarily act as a simple heating prescription.

In this work, we have also tried to minimize the effect of external mass inflow by considering star clusters in isolation. This is certainly not the case for clusters moving through cold, dense environments, as they can potentially amass a significant amount of gas from their surroundings (Naiman *et al.*, 2009, 2011), or clusters moving quickly though hot halo gas or the galactic disk (Priestley *et al.*, 2011). If the proto-globular clusters reside within cold gas, stellar winds and exterior inflows in such clusters could combine to create even larger central density enhancements (Naiman *et al.*, 2009, 2011; Conroy and Spergel, 2011; Pflamm-Altenburg and Kroupa, 2009). However, if the young clusters obtain their current orbital trajectories early in their lifetimes, a significant fraction of their accumulated mass can be removed by ram pressure stripping. A self consistent treatment of both interior and exterior gas accumulation in multi-dimensional simulations, which includes the effects of compact object accretion, tidal stripping, photoionization, and pulsar heating will be presented elsewhere.

While previous work has estimated the ability of star clusters to retain stellar winds (D'Ercole *et al.*, 2008, 2010; Conroy, 2012; Conroy and Spergel, 2011), calculations have so far been restricted to a small range of cluster properties and stellar ages. Motivated by this, we

have calculated gas retention in star clusters of various ages, stellar mass and compactness. In agreement with previous studies we find that before star formation is triggered about $\leq$10% of the total cluster mass is comprised of retained stellar wind gas, naively implying that the original proto-GCs had to be more massive than what is observed today (Conroy, 2012; D'Ercole *et al.*, 2008). However, we show that multiple episodes of star formation can in fact take place during the lifetime of a cluster in particular between $\sim$ 1 and $\sim$ 10 Gyrs, thus suggesting a sizable enhancement in star formation. The overlap of this time range with the AGB phase further strengthens the case for stellar wind retention as a critical component in the formation of subsequent generations of stars in GCs.

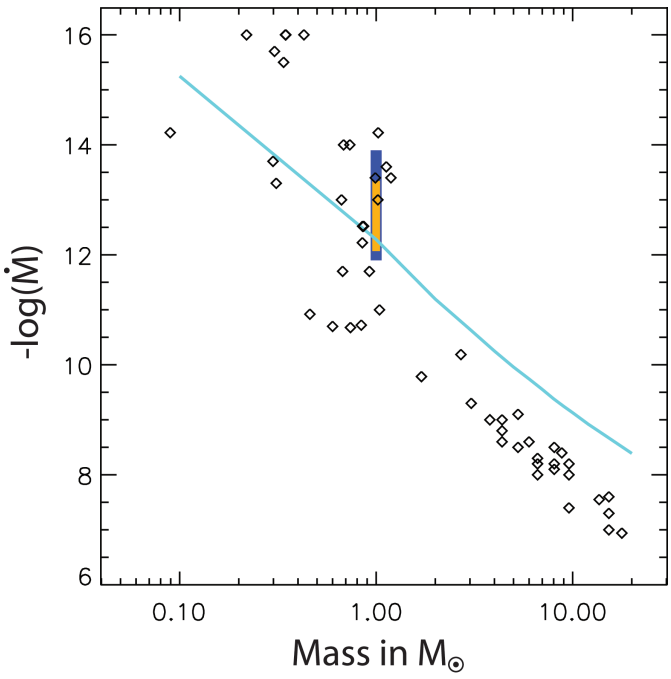

Figure 5.1: Mass loss rate estimates along the main sequence as a function of initial stellar mass. Observational estimates are plotted as black diamonds Cranmer and Saar (2011); de Jager *et al.* (1988); Searle *et al.* (2008); Waters *et al.* (1987); Debes (2006); Badalyan and Livshits (1992); Morin *et al.* (2008). The blue rectangle denotes the estimated variations in the solar mass loss rate Wood *et al.* (2005), and the yellow rectangle shows the observed variations in the mass loss rate of the Sun as a function of its X-ray activity Cohen (2011). The blue line shows the main sequence mass loss rate prescription used by MESA.

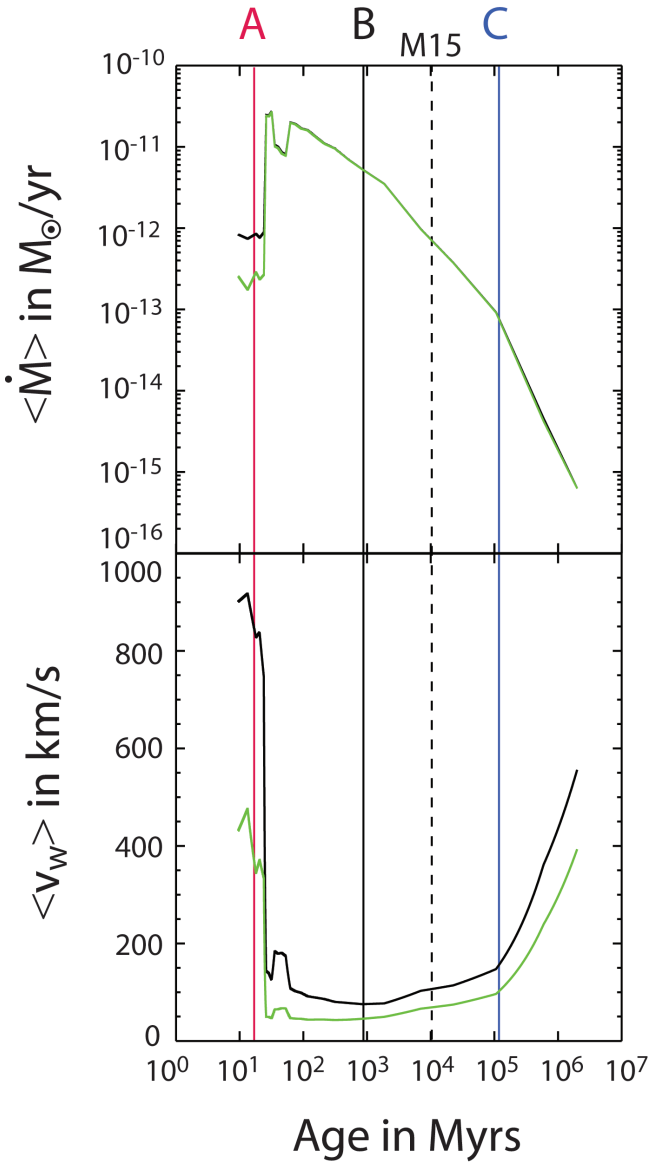

Figure 5.2: Average cluster mass loss rates and wind velocities as a function of time for $Z = 1/10Z_\odot$. Green lines assume gas dynamics are dominated by the wind properties of the turn off stars (§6.3.2.1), black lines show the population averaged values (§6.3.2.2). Three representative times in the clusters age are denoted by the solid vertical lines. The current age of M15 is denoted by the vertical dashed line. Note that while the turn off stars contribute the majority of the mass (top panel), the main sequence stars dominate the energy injection (bottom panel) as a result of their higher effective wind velocities.

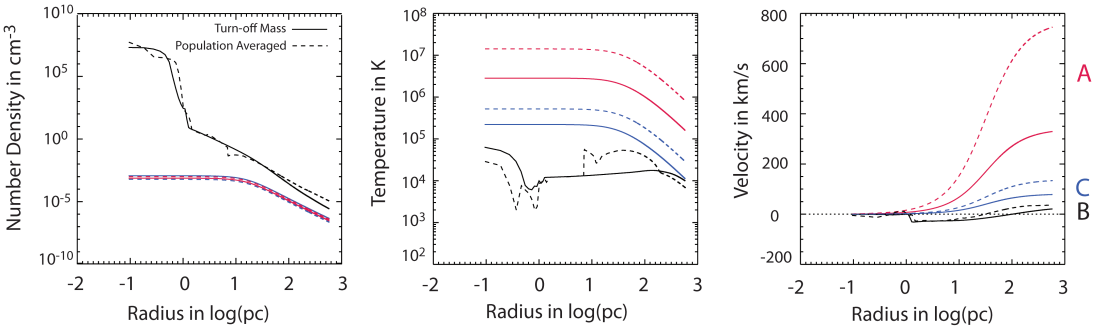

Figure 5.3: Hydrodynamic profiles for the three representative times denoted in Figure 5.2. These three plots are the density, temperature and velocity profiles at three representative times for a $M_c = 10^7\,M_\odot$, $\sigma_v = 30\,\mathrm{km/s}$ model. Solid and dashed lines represent the turn off mass and population averaged prescriptions for models without memory, respectively.

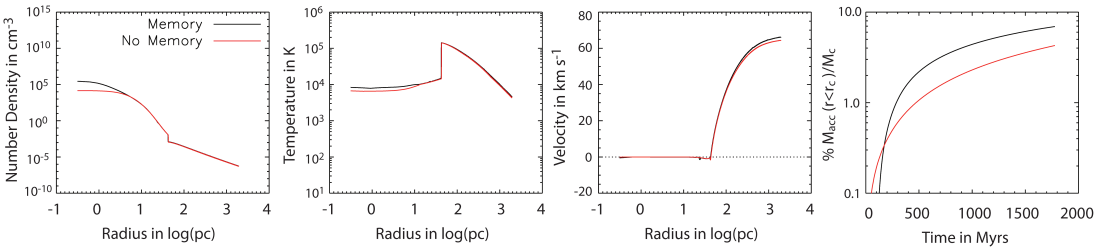

Figure 5.4: Hydrodynamic profiles and gas accumulation for a $t_i = 2000\,\mathrm{Myrs}$ cluster with $M_c = 10^7\,M_\odot$ and $\sigma_v = 27\,\mathrm{km/s}$. When the cluster is allowed to retain gas throughout its evolution (black line) it can accumulate significantly more mass (6.9% instead of 4.3%) by the time star formation is triggered than when the cluster is assumed to have no retention memory.

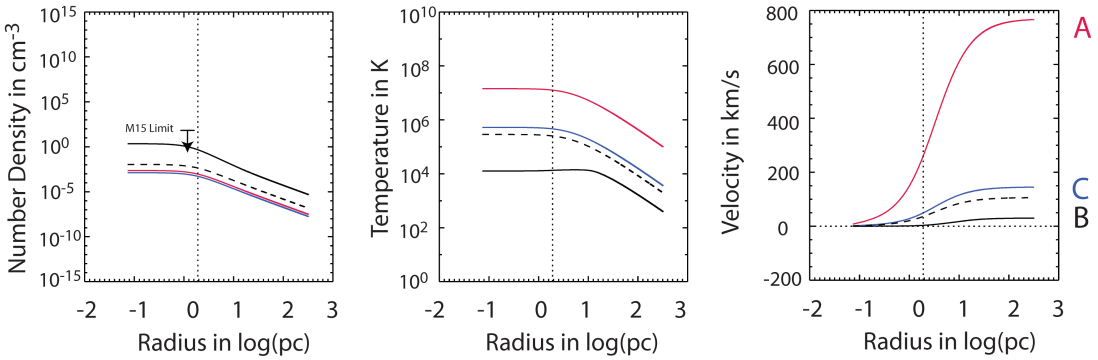

Figure 5.5: Hydrodynamic profiles for M15 with $M_c = 4.5 \times 10^5\,M_\odot$ and $\sigma_v = 14\,\mathrm{km/s}$ (McNamara *et al.*, 2004; Gerssen *et al.*, 2002) at the three representative times in Figure 5.2, including the predicted profiles for its current age (dashed lines). Here, the population averaged prescription is used and we assume the cluster has no gas retention memory.

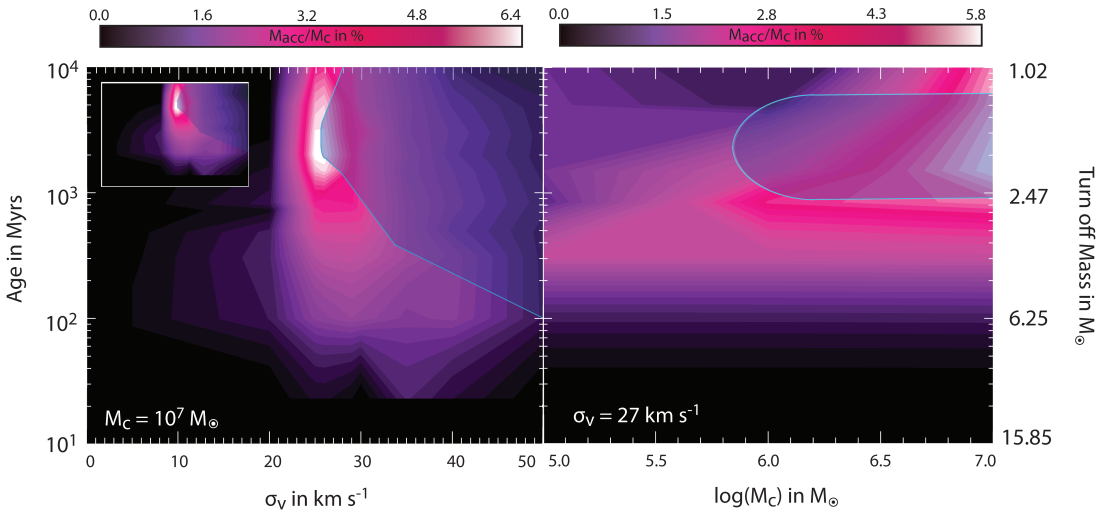

Figure 5.6: Mass accumulation, $M_{\rm acc}$, as a function of the potential parameters $M_{\rm c}$ and σ for the turn off mass prescription. The blue shaded regions delimit the boundaries for which our models collapse and trigger star formation. *Left:* Contours of $M_{\rm acc}/M_{\rm c}$ for a fixed cluster core mass of $M_{\rm c} = 10^7\,M_\odot$ and a varying velocity dispersion. *Inset Panel:* Modifications to these contours when the velocity dispersion of the potential is included in the calculation of the total wind kinetic energy (the wind velocity and the velocity dispersion are added in quadrature). *Right:* Contours of $M_{\rm acc}/M_{\rm c}$ for a fixed velocity dispersion of $\sigma_v = 27\,{\rm km/s}$ and varying cluster mass. Here we assume the cluster has no gas retention memory.

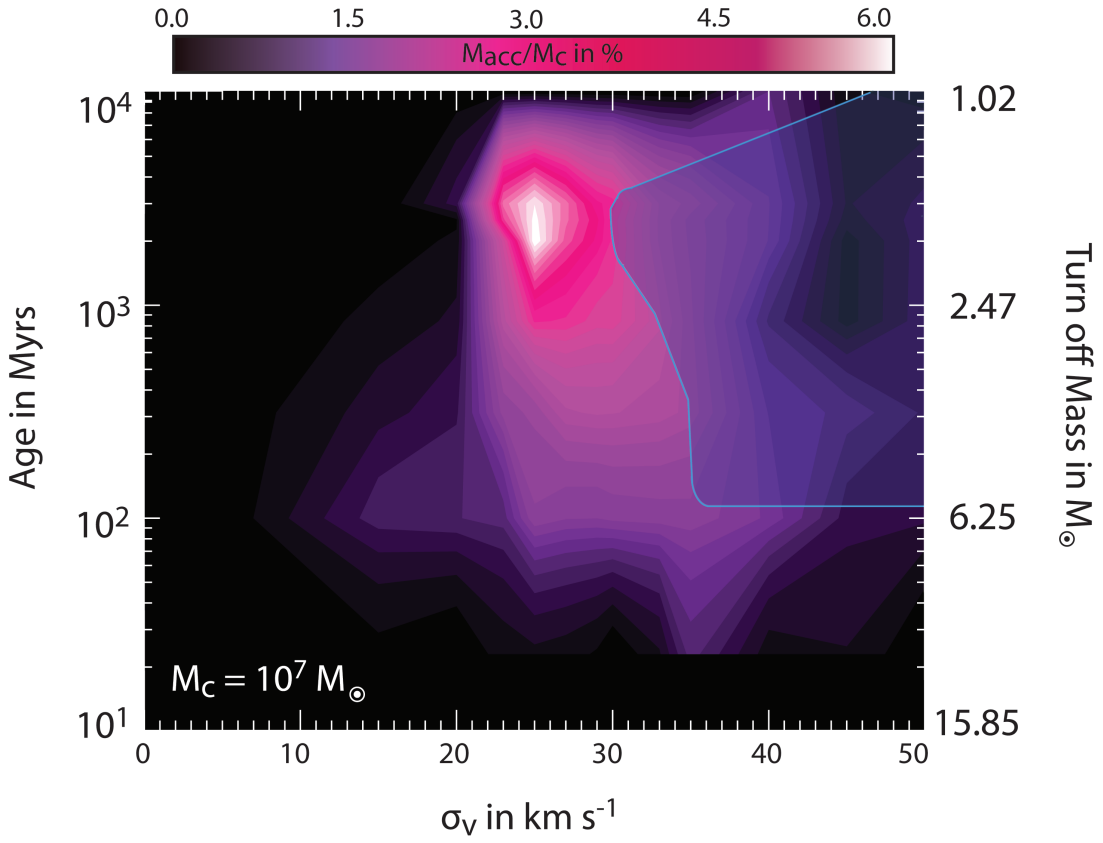

Figure 5.7: Mass accumulation, $M_{\rm acc}$, as a function of σ for a fixed cluster core mass of $M_{\rm c}$ = $10^7\,M_{\odot}$, calculated using the population averaged prescription. The blue shaded region delimits the boundaries for which our models collapse and trigger star formation. Here we assume the cluster has no gas retention memory. The additional thermalized high velocity winds from main sequence stars add appreciable heat to the central regions of the cluster, thus inhibiting star formation at lower cluster velocity dispersions.

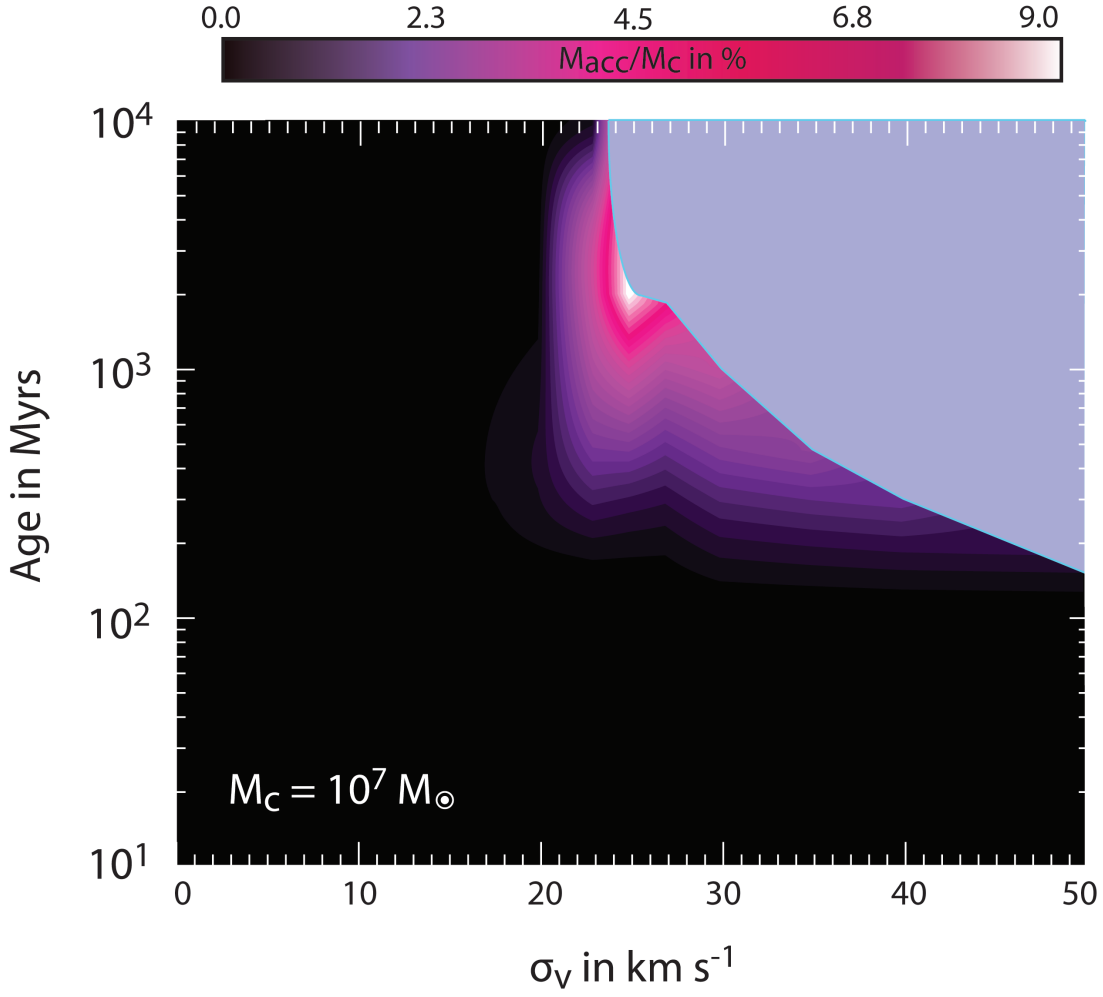

Figure 5.8: Mass accumulation, $M_{\rm acc}$, as a function of σ for a fixed cluster core mass of $M_{\rm c} = 10^7\,M_{\odot}$, calculated using the population averaged prescription. The blue shaded region delimits the boundaries for which our models collapse and trigger star formation. Here we assume the cluster has gas retention memory. After star formation is triggered we expect the subsequent gas accumulation after supernova energy injection (Figure 5.9) to initially proceed as in Figure 5.6. Here, the additional mass input increases the cooling capacity of the cluster gas when compared to that in Figure 5.7 and, as found previously, the star forming contours overlap with the largest central mass accumulation regions, as in Figure 5.6.

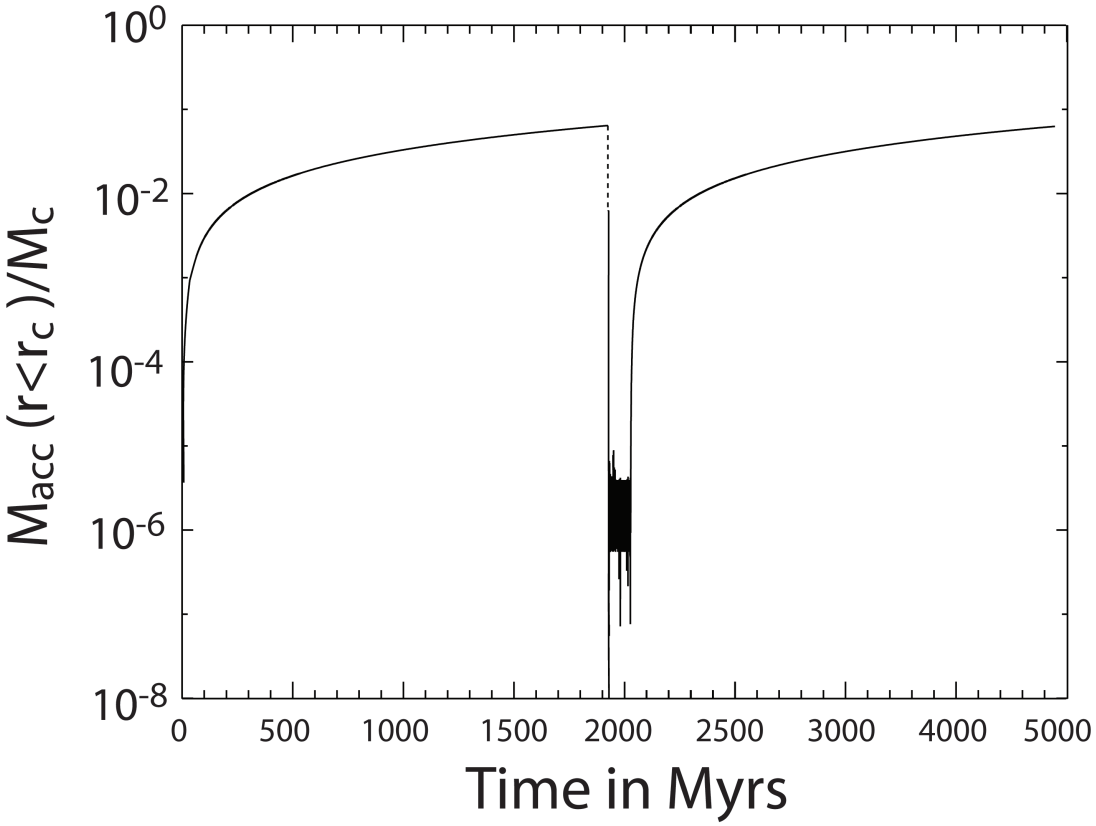

Figure 5.9: Cycles of mass accumulation in a potential with $M_c = 10^7\,M_\odot$, $\sigma_v = 26\,\mathrm{km/s}$ and $t_i = 2000\,\mathrm{Myrs}$ including star formation, and supernovae explosions. Mass accumulates till star formation is triggered, then 90% of this mass is assumed to form stars, removing the gas from the simulation (dashed lines). Supernovae persist for 100 Myrs at a rate of $2 \times 10^{-6}\,\mathrm{yr}^{-1}$ further stripping mass from the system. For simplicity, we have assumed the mass injection properties to be steady during the simulation and that the cluster has no gas retention memory.

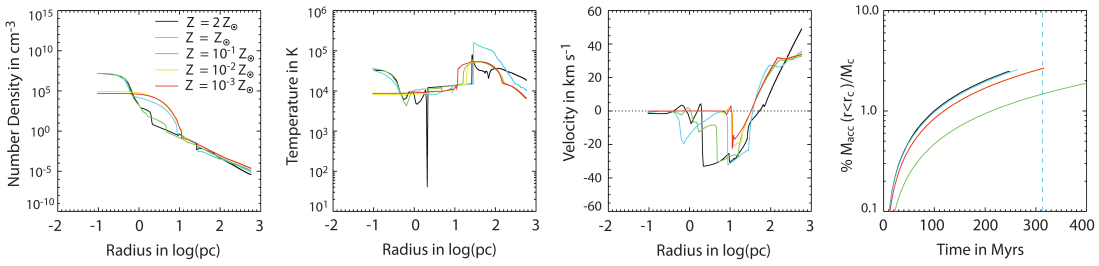

Figure 5.10: Gas properties for $M_c = 10^7\,M_\odot$, $\sigma_v = 30\,\mathrm{km/s}$ cluster at $t_i = 313\,\mathrm{Myrs}$ for different metallicities. Here, we use the population averaged values of the wind parameters and assume the cluster has no gas retention memory.

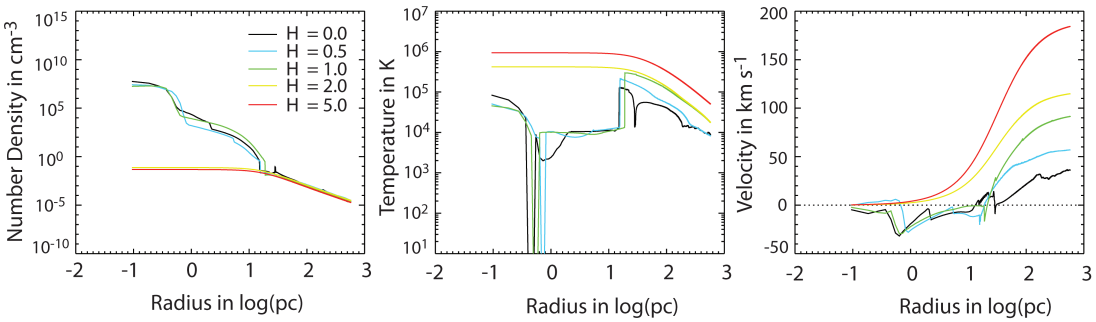

Figure 5.11: *Left 3 Plots:* Gas properties for $M_c = 10^7\,M_\odot$, $\sigma_v = 30\,\mathrm{km/s}$ cluster at $t_i = 1860\,\mathrm{Myrs}$ with added heat in the form of thermal energy: $e_{int,new} = (1+H)e_{int,old}$. Here, we use the population averaged values of the wind parameters and assume the cluster has no gas retention memory.

Chapter 6

Modeling the Tenuous Intracluster Medium in Globular Clusters

6.1 Introduction

For over half a century, globular cluster observations have revealed a paucity of intracluster dust and gas. Given the abundance of evolved stellar ejecta and the extensive timescales between galactic disk crossing events, these observations are at odds with theoretical expectations. Orbiting in the Galactic halo, globular clusters traverse through the plane of the galaxy on timescales of 10^8 years, expelling the intracluster medium with each passage (Odenkirchen *et al.*, 1997). Between galactic disk crossing events, the evolving stellar members continuously fill the cluster with stellar ejecta. These stars are about $0.8 M_{\odot}$ at the main sequence turn-off and, during the evolution to the white dwarf stage, 10-100 $M_{\odot}$ of material is predicted to have been accumulated (Tayler and Wood, 1975). The hunt for this elusive intracluster medium has been

extensive, yet the majority of observations have been fruitless. Searches for dust and atomic, molecular, and ionized gas have been carried out, resulting in upper limits and detections that are generally much lower than the values expected if the mass was effectively retained.

Submillimeter and infrared (IR) searches for dust in globular clusters (Lynch and Rossano, 1990; Knapp *et al.*, 1995; Origlia *et al.*, 1996; Hopwood *et al.*, 1999) have predominately resulted in low dust mass content upper limits on the order of $\leq 4 \times 10^{-4} M_{\odot}$ (Barmby *et al.*, 2009), as compared to predicted dust masses ranging from $10^{-0.8} - 10^{-3.6} M_{\odot}$. Tentative evidence for excess IR emission from cool dust in the metal-rich globular cluster NGC 6356 was found nearly two decades ago (Hopwood *et al.*, 1998), although the lack of a 90 μm excess casts doubt on this detection (Barmby *et al.*, 2009). Only the Galactic globular cluster M15 (NGC 7078) depicts clear evidence for an IR excess (Evans *et al.*, 2003; Boyer *et al.*, 2006), revealing a cluster dust mass of $9 \pm 2 \times 10^{-4} M_{\odot}$, which is at least one order of magnitude below the predicted value. The lack of intracluster dust might suggest that evolved stars produce less dust than predicted, although evidence to the contrary has been found in M15 and NGC 5139, where some of the dustiest, most mass expelling stars have been found (Boyer *et al.*, 2006, 2008).

Troland *et al.* (1978) led the first search for 2.6 mm CO emission in globular clusters, which resulted in a non-detection, but lacked sufficient sensitivity to rule out the presence of molecular gas. Since then, upper limits have been placed on the molecular gas content in globular clusters, constraining the mass to about 0.1 $M_{\odot}$ (Smith *et al.*, 1995b; Leon and Combes, 1996). The most promising search lead to a tentative detection of two CO lines in the direction of globular cluster 47 Tucanae (NGC 104), which was interpreted to be the result of the bow

shock interaction generated as the cluster traverses through the Galactic halo (Origlia *et al.*, 1997). Other searches, including attempts to measure OH and H_2O maser emission, have been unsuccessful (Knapp and Kerr, 1973; Kerr *et al.*, 1976; Frail and Beasley, 1994; Cohen and Malkan, 1979; Dickey and Malkan, 1980; van Loon *et al.*, 2006).

Neutral hydrogen (HI) at 21-cm was detected in NGC 2808, measuring $200M_{\odot}$ of gas (Faulkner *et al.*, 1991). This is not beyond dispute, however, since there is known to be a foreground 21-cm extended region around the cluster. Most other attempts to detect HI in globular clusters have been unsuccessful or resulted in upper limits on the order of a few solar masses (Heiles and Henry, 1966; Robinson, 1967; Kerr and Knapp, 1972; Knapp *et al.*, 1973; Bowers *et al.*, 1979; Birkinshaw *et al.*, 1983; Lynch *et al.*, 1989; Smith *et al.*, 1990; van Loon *et al.*, 2006, 2009). A tentative HI detection of $0.3M_{\odot}$ in M15 was presented by van Loon *et al.* (2006) using 21-cm Arecibo observations.

The most reliable constraints on the presence of intracluster material have been derived from radio dispersion measurements of known millisecond pulsars in 47 Tucanae (Camilo *et al.*, 2000), which resulted in the first detection of ionized gas with a density of $n_e = 0.067 \pm 0.015$ cm^{-3} (Freire *et al.*, 2001b). This ionized gas measurement, as well as the upper limits placed on ionized gas in other clusters (Smith *et al.*, 1976; Faulkner and Freeman, 1977; Knapp *et al.*, 1996c), correspond to a deficiency of gas by two or three orders of magnitude when compared to the amount predicted by the effective accumulation of evolved stellar ejecta within the observed clusters.

The paucity of intracluster gas hints at the desirability for a common mechanism that acts to constantly remove gas from the cluster. Potential gas evacuation processes may be

external or internal to the globular cluster itself. One external process is ram pressure stripping of the intracluster medium as the globular cluster traverses through the surrounding hot galactic halo. This mechanism has been investigated both analytically and numerically in the past. Frank and Gisler (1976) found that the interstellar medium of the Galactic halo was one order of magnitude too low in density to account for the stripping of the cluster. Priestley *et al.* (2011), aided by the use of three-dimensional hydrodynamical simulations, revisited this problem and concluded that halo sweeping was only an effective gas evacuation mechanism for globular clusters $\leq 10^5 M_{\odot}$. This is further compounded by the fact that the majority of the globular clusters reside in low density regions of the halo.

Internal evacuation mechanisms are more varied in scope with some being impulsive and others being continuous in nature. Vandenberg and Faulkner (1977) suggested the possibility that UV heating from the horizontal branch (HB) stellar population might provide sufficient energy input to explain the low gas densities in clusters, however not all clusters contain hot HB stars. Umbreit *et al.* (2008) argues that the energy injected by stellar collisions could be significant, in particular in clusters with high encounter rates. Coleman and Worden (1977) investigated the possibility that flaring M-dwarf stars might supply the energy injection required to evacuate the cluster, however the number and distribution of M-dwarf stars in clusters is highly uncertain. The energy injection from hydrogen rich novae explosions is another possible gas evacuation mechanism, which was investigated early on by Scott and Durisen (1978) and more recently by Moore and Bildsten (2011). However, it is highly uncertain whether these explosions occur with enough frequency (Bode and Evans, 2008) and if the beamed structure of the emanating outflows will lead to significantly lower gas removal efficiencies (O'Brien *et al.*,

2006). Finally, the presence of millisecond pulsars in many of these systems not only enables the placement of stringent intracluster density constraints, but also provides globular clusters with yet another mechanism of energy injection (Spergel, 1991).

Several mechanisms for gas removal have been discussed above, with internal energy injection processes being favored over ram pressure stripping, however the contribution of the discussed internal processes is expected to vary significantly between clusters such that, individually, they would be unable to explain the universality of low gas densities seen across all globular clusters. Mass and energy injection from stellar winds, on the other hand, are a common feedback ingredient in all clusters. In the past, it has been argued that the evolved stellar ejecta does not posses sufficient energy to escape the cluster potential (Vandenberg and Faulkner, 1977). This, however, has been called into question by observations of giant stars with wind velocities exceeding the typical cluster escape velocity (Smith *et al.*, 2004). What is more, energy injection from the usually neglected, although vast, main sequence stellar population could play a decisive role in mediating mass retention in these systems (Smith, 1999).

Motivated by this line of reasoning, we present a systematic investigation of the impact of outflows emanating from both evolved and non-evolved stellar members on the intracluster gas evolution. To aid in our interpretation of the data, we compare observational constraints with the results of hydrodynamical simulations that include radiative cooling as well as mass and energy injection from the cluster members, which we derive using stellar evolution models. It is shown that the observational constraints of intracluster gas can be successfully explained in models where the expulsion of evolved stellar ejecta is caused by the efficient thermalization of the energy emanating from the main sequence stellar population. In globular clusters with

stringent gas density constraints, such as 47 Tucanae, M15, NGC 6440, and NGC 6752, we argue that energy output from the main sequence stellar population alone is capable of efficiently clearing out the evolved stellar ejecta. Since the majority of clusters with stringent gas content constraints host millisecond pulsars, we extend our calculations to include the energy injection supplied by their winds. The detection of ionized gas in 47 Tucanae, in particular, allows us to place strict limits on the pulsar wind thermalization efficiency within these systems.

6.2 Modeling Gas in Globular Clusters

We begin with a simple calculation to estimate the intracluster gas density (Pfahl and Rappaport, 2001b), considering a cluster comprised of $N = 10^6 N_6$ stars with masses of $0.9 M_\odot$ at the main sequence turn-off. The ratio of evolved stars to the total number of stars within the cluster is roughly $N_{\rm to}/N \approx 0.01$, resulting in an average separation of

$$r_\perp = 6.4 \times 10^{17} \left(\frac{N_{\rm to}}{10^2}\right)^{-1/3} \left(\frac{r_{\rm h}}{1{\rm pc}}\right) \ {\rm cm}, \tag{6.1}$$

where $r_{\rm h}$ represents the cluster half-light radius. Making the assumption that the wind from each evolved stellar member extends only to its nearest neighbors, a lower limit on the cluster gas density may be obtained. Under this assumption, the cluster gas density is found to be

$$n_\perp = 0.1 \left(\frac{N_{\rm to}}{10^2}\right)^{2/3} \left(\frac{r_{\rm h}}{1{\rm pc}}\right)^{-2} \left(\frac{v_{\rm w,to}}{70 \ {\rm km \ s^{-1}}}\right)^{-1} \left(\frac{\dot{M}_{\rm w,to}}{10^{-7} M_\odot \ {\rm yr^{-1}}}\right) \ {\rm cm^{-3}}, \tag{6.2}$$

where $\dot{M}_{\rm w,to}$ and $v_{\rm w,to}$ correspond to the mass loss rate and wind velocity of the evolved stellar members (Section 6.3.2 contains a more detailed description of stellar evolution models). This lower limit may then be contrasted with a second case, where evolved stellar winds extend to fill the volume of the entire cluster. The density for this second scenario is found to be

$$n_{\rm h} = 1.5 \left(\frac{N_{\rm to}}{10^2}\right) \left(\frac{r_{\rm h}}{1{\rm pc}}\right)^{-2} \left(\frac{v_{\rm w,to}}{70\ {\rm km\ s^{-1}}}\right)^{-1} \left(\frac{\dot{M}_{\rm w,to}}{10^{-7} M_{\odot}\ {\rm yr^{-1}}}\right) {\rm cm^{-3}}. \tag{6.3}$$

In fact, we suspect that the gas density may exceed $n_{\rm h}$ if $v_{\rm w,to} \lesssim \sigma$, where σ is the velocity dispersion of the cluster, when the gravitational effects of the cluster are taken into consideration (Pflamm-Altenburg and Kroupa, 2009) . On the other hand, if significant energy injection takes place within the cluster, the gas density is expected to be lower than the lower gas density limit $n_{\perp}$. The impact of energy injection on the intracluster gas content is presented in Figure 6.1 for two illustrative cases: the emanation of hot winds from an abundant main sequence population alone (panel *b*) and from the combined effort of the main sequence stellar winds and millisecond pulsar winds (panel *c*). Much of our effort in this Chapter will be dedicated to determining the state of the intracluster gas in various globular clusters, and describing how the expected energy injection from main sequence and millisecond pulsar populations may affect mass retention in these systems.

6.3 Numerical Methods and Initial Setup

6.3.1 Hydrodynamics

Our investigation of evolved stellar ejecta retention within globular clusters is mediated by hydrodynamical simulations incorporating energy and mass injection. For the purpose of simplicity, spherical symmetry is assumed (Quataert, 2004; Hueyotl-Zahuantitla *et al.*, 2010). `FLASH`, a parallel, adaptive-mesh hydrodynamical code (Fryxell *et al.*, 2000c), is employed to solve the hydrodynamical equations in one-dimension. Within the cluster, emanating winds from the dense stellar population and millisecond pulsars, when present, are assumed to shock and thermalize and, as such, the mass and energy contributions are implemented as source terms in the hydrodynamical equations. In spherical symmetry, the hydrodynamical equations may be written in the following form:

$$\frac{\partial \rho}{\partial t} + \frac{1}{r^2}\frac{\partial}{\partial r}\left(\rho u r^2\right) = q_{m,\star}(r,t) \tag{6.4}$$

$$\frac{\partial u}{\partial t} + u\frac{\partial u}{\partial r} + \frac{1}{\rho}\frac{\partial P}{\partial r} = -\frac{d\Phi_g}{dr} - q_{m,\star}(r,t)u \tag{6.5}$$

$$\frac{\partial \varepsilon}{\partial t} + \frac{1}{r^2}\frac{\partial}{\partial r}\left(\varepsilon u r^2\right) + P\frac{\partial u}{\partial r} = q_{\varepsilon,\star}(r,t) + q_{\varepsilon,\Omega}(r,t) - Q(r), \tag{6.6}$$

where $P = P(r)$, $\rho = \rho(r)$, $u = u(r)$ and $\varepsilon = \varepsilon(r)$ correspond to the gas pressure, density, radial velocity and internal energy density, respectively (Holzer and Axford, 1970; Hueyotl-Zahuantitla

et al., 2010). $Q(r) = n_{\rm i}(r) n_{\rm e}(r) \Lambda(T,Z)$ is the cooling rate for a gas consisting of ion and electron number densities, $n_{\rm i}(r)$ and $n_{\rm e}(r)$, and the cooling function for gas of temperature T with metallicity Z is represented by $\Lambda(T,Z)$. Cooling functions are taken from Gnat and Sternberg (2007) for $T > 10^4$ K and from Dalgarno and McCray (1972) for $10 \leq T \leq 10^4$ K.

In equations (6.4)-(6.6), the terms $q_{{\rm m},\star}(r,t)$ and $q_{\varepsilon,\star}(r,t)$ respectively represent the rates of mass and energy injection produced by the evolved stellar ejecta at a time t in a cluster's history. Stellar winds dominate cluster mass injection, and, as a result, the hydrodynamical influence of the millisecond pulsars is restricted to the energy injection term: $q_{\varepsilon,\Omega}(r,t)$. Given N stars, each with an average mass loss rate (at a particular evolutionary time t) of $\langle \dot{M}(t) \rangle$ and a wind energy injection rate $\frac{1}{2} \langle \dot{M}(t) \rangle \langle v_{\rm w}(t)^2 \rangle$, we find a total mass loss of

$$\dot{M}(t)_{\rm w,total} = N \langle \dot{M}(t) \rangle = \int 4\pi r^2 q_{\rm m}(r,t) dr \tag{6.7}$$

and a total wind energy injection of

$$\dot{E}(t)_{\rm w,\star,total} = \frac{1}{2} N \langle \dot{M}(t) \rangle \langle v_{\rm w}(t)^2 \rangle = \int 4\pi r^2 q_{\varepsilon,\star}(r,t) dr, \tag{6.8}$$

where $q_{\varepsilon,\star}(r,t) = \frac{1}{2} q_{\rm m}(r,t) \langle v_{\rm w}(t)^2 \rangle$. In order to preserve simplicity, we have ignored the effects of mass segregation. In addition, we assume $q_{\rm m}(r,t) \propto n_\star(r)$, such that $q_m(r,t) = A(t) r^{-2} \frac{d}{dr} \left(r^2 \frac{d\Phi_g}{dr} \right)$, where $A(t) = \langle \dot{M}(t) \rangle / (4\pi G \langle M_\star \rangle)$ and $\langle M_\star \rangle$ corresponds to the average mass of a star.

The stellar cluster gravitational potentials are simulated with a Plummer model, which

takes the form

$$\Phi_g = -\frac{GM_c}{\left[r^2 + r_c^2(\sigma_v)\right]^{1/2}} \tag{6.9}$$

for a total cluster of mass M_c with velocity dispersion $\sigma_v = \left(3^{3/4}/\sqrt{2}\right)^{-1} \sqrt{GM_c/r_c}$ (Brüns *et al.*, 2009b; Pflamm-Altenburg and Kroupa, 2009). It should be noted that while the shape of the potential can impact the radial distribution of gas within the core (Naiman *et al.*, 2011), the total amount of gas accumulated within the cluster is relatively unaffected by the shape of the potential. In addition, to account for the gas dynamics under the influence of Φ_g, the self gravity of the gas is computed using `FLASH`'s multipole module. The resolution is fixed to 6400 radial cells for each model. The core radius, r_c, sets the resolution within the computational domain, ensuring that we adequately resolve the core and setting a cluster potential of effectively zero at the outer boundary.

6.3.2 Stellar Evolution

Our simulations are highly dependent upon two key parameters: the time dependent average stellar mass loss rate and stellar wind velocity. The average stellar mass loss rate and stellar wind velocity then directly determine the mass and energy injection rates, $q_{m,\star}$ and $q_{\varepsilon,\star}$. These rates must encompass the average mass loss properties of the stellar population as a whole, since we are employing spherically symmetric simulations.

6.3.2.1 The Turn Off Approximation

To approximate the total mass loss and mean thermal velocities of the colliding winds within the cluster, we employ the formalism developed by Pooley and Rappaport (2006). In the relations

$$\langle v_{\mathrm{w,to}}^2 \rangle \approx \frac{2\Delta E_K}{\Delta M} \tag{6.10}$$

and

$$\langle \dot{M}_{\mathrm{to}} \rangle \approx \frac{\Delta M}{\Delta t}, \tag{6.11}$$

the integrated kinetic energy of the stellar winds and mass loss by the stellar population's turn off stars has been used as a proxy for the average values. The kinetic energy of the winds is given by $\Delta E_K = \frac{1}{2}\int_{t_0}^{t_1} \dot{M}_{\mathrm{to}} v_{\mathrm{w,to}}^2 dt$ and $\Delta M = \int_{t_0}^{t_1} \dot{M}_{\mathrm{to}} dt$ denotes the mass loss input rate integrated over the lifetime of the turn-off stars, $\Delta t = t_1 - t_0$, where t_0 is the zero age main sequence (ZAMS) and t_1 is the onset of the white dwarf stage. While this approximation provides a reasonable estimate for the overall supply of wind mass and energy to the cluster, it fails to capture realistic stellar wind variability, which is currently not well constrained (Marigo, 2012b; Wood *et al.*, 2005; Cohen, 2011).

6.3.2.2 The Population Averaged Approximation

Neglected in the formalism outline above are the effects from the addition of mass and kinetic energy input from stars with $M_\star < M_{\mathrm{to}}$. These effects may be included by convolving the given definitions of the average mass loss rate and stellar wind velocity with an initial mass function (IMF) and a star formation history. Following the logic of Kroupa *et al.* (2013b), the

average number of stars in a mass interval $[M_\star, M_\star + dM_\star]$ evolving between a span of time $[t, t+dt]$ is given by the relation $dN = \zeta(M_\star, t) N_\star b(t) dM_\star dt$ where $\zeta(M_\star, t)$ denotes the IMF, assumed to be accurately described by the Kroupa (2001) IMF, the normalized star formation history is given by $b(t)$, and $N_\star$ is the total number of stars within the cluster. For a non-evolving IMF, $\zeta(M_\star, t) = \zeta(M_\star)$, comprised of a mass distribution extending from masses M_L to M_H, the normalized star formation history is given by $1/t_{\rm age}(M_L) \int_0^{t_{\rm age}(M_L)} b(t) dt = 1$, where $t_{\rm age}(M_\star)$ denotes the lifetime of a star of a given $M_\star$ and $b(t) = \delta(t - t_0)$ for a population of coeval stars forming at t_0.

The average mass $\langle \Delta M(t_i) \rangle$ and kinetic energy $\langle \Delta E_K(t_i) \rangle$ injection within the cluster at a time t_i, by a population of stars of $M_\star \epsilon\, [M_{\rm L}, M_{\rm H}]$ whose birth rate is regulated by $b(t)$, may then be formalized as

$$\langle \Delta M(t_i) \rangle = \int_{t_0}^{t_i} b(t) \int_{M_{\rm L}}^{M_{\rm H}} \zeta(M_\star) \dot{M}(M_\star, t) dM_\star dt \tag{6.12}$$

and

$$\langle \Delta E_K(t_i) \rangle = \frac{1}{2} \int_{t_0}^{t_i} b(t) \int_{M_{\rm L}}^{M_{\rm H}} \zeta(M_\star) \dot{M}(M_\star, t) v_w^2(M_\star, t) dM_\star dt, \tag{6.13}$$

respectively. Stars with lifetimes $t_{\rm age}(M_\star) < t_i$ abandon the stellar population and are not included in the averaging. For any given time $t_i = t_{\rm to}$, $M_{\rm H} = M_{\rm to}$, permitting us to split these equations into their corresponding turn off and main sequence components. These are given by

$$\langle \Delta M(t_i) \rangle = \langle \Delta M_{\rm to} \rangle + f_{\rm ms} \langle \Delta M_{\rm ms} \rangle \tag{6.14}$$

such that

$$\langle \Delta M(t_i) \rangle = \zeta(M_{\rm to}) \int_{t_0}^{t_i} b(t) \dot{M}(M_{\rm to}, t) dt + f_{\rm ms} \int_{t_0}^{t_i} b(t) \int_{M_{\rm L}}^{M_{\rm H}<M_{\rm to}} \zeta(M_\star) \dot{M}(M_\star, t) dM_\star dt \tag{6.15}$$

and

$$\langle \Delta E_K(t_i) \rangle = \langle \Delta E_{K,{\rm to}} \rangle + f_{\rm ms} \langle \Delta E_{K,{\rm ms}} \rangle$$

$$= \frac{1}{2} \zeta(M_{\rm to}) \int_{t_0}^{t_i} b(t) \dot{M}(M_{\rm to}, t) v_w^2(M_{\rm to}, t) dt + \frac{f_{\rm MS}}{2} \int_{t_0}^{t_i} b(t) \int_{M_{\rm L}}^{M_{\rm H}<M_{\rm to}} \zeta(M_\star) \dot{M}(M_\star, t) v_w^2(M_\star, t) dM_\star dt, \tag{6.16}$$

where the fraction of the main sequence stellar winds that is effectively thermalized and mixed within the cluster environment is denoted by $f_{\rm ms}$. After leaving the main sequence branch, the majority of a star's mass is lost and, as such, we approximate $\langle \Delta M(t_i) \rangle \approx \langle \Delta M_{\rm to} \rangle$. As a result, equations (6.10) and (6.11), representing the average stellar wind velocity and average stellar mass loss rate, may then be cast into the more general form

$$\langle v_w^2(t_i) \rangle = \frac{2 \langle \Delta E_K(t_i) \rangle}{\langle \Delta M(t_i) \rangle} \approx \frac{2(\langle \Delta E_{K,{\rm to}} \rangle + f_{\rm ms} \langle \Delta E_{K,{\rm ms}} \rangle)}{\langle \Delta M(t_{\rm to}) \rangle}$$

$$= \frac{\int_{t_0}^{t_i} b(t) \dot{M}(M_{\rm to}, t) v_w^2(M_{\rm to}, t) dt}{\int_{t_0}^{t_i} b(t) \dot{M}(M_{\rm to}, t) dt} + f_{\rm ms} \frac{\int_{t_0}^{t_i} b(t) \int_{M_{\rm L}}^{M_{\rm H}<M_{\rm to}} \zeta(M_\star) \dot{M}(M_\star, t) v_w^2(M_\star, t) dM_\star dt}{\zeta(M_{\rm to}) \int_{t_0}^{t_i} b(t) \dot{M}(M_{\rm to}, t) dt}. \tag{6.17}$$

and

$$\langle \dot{M}(t_i) \rangle \approx \frac{\langle \Delta M_{\rm to} \rangle}{t_i} = \frac{1}{t_i} \zeta(M_{\rm to}) \int_{t_0}^{t_i} b(t) \dot{M}(M_{\rm to}, t) dt, \tag{6.18}$$

for a given stellar population lifetime t_i.

Individual mass loss rates $\dot{M}(M_\star, t)$ and wind velocities $v_w(M_\star, t)$ are calculated with MESA stellar evolution models (Paxton *et al.*, 2011). MESA follows the evolution of a grid of stellar models with $M_\star = 0.6\,M_\odot$ - $8\,M_\odot$ from ZAMS to the white dwarf stage. The wind velocity is approximated to be equal to the escape velocity, accurate within a factor of a few across a wide range of masses and life stages (Abbott, 1978; Evans *et al.*, 2004; Schaerer *et al.*, 1996; Nyman *et al.*, 1992; Vassiliadis and Wood, 1993; Loup *et al.*, 1993; Dupree and Reimers, 1987; Debes, 2006; Badalyan and Livshits, 1992). MESA uses the Reimers (1975) prescription, given by $\dot{M}_R = 4 \times 10^{-13} \eta_R (M/M_\odot)^{-1} (L/L_\odot)(R/R_\odot) M_\odot \mathrm{yr}^{-1}$, where $\eta_R = 1.0$, to estimate the stellar mass loss over the RGB branch and main sequence lifetime. As illustrated in Figure 6.2, this prescription provides a reasonable estimate for the stellar mass loss rates of low mass main sequence stars, which can be also approximated by $\dot{M}_{\mathrm{ms}} \approx 10^{-12} (M/M_\odot)^3 M_\odot \mathrm{yr}^{-1}$. Also shown in Figure 6.2 are the values expected for the injected luminosity and average wind velocity per star as a function of the stellar population's turn-off mass and metallicity. The different contributions to the mass and energy arising from the evolved stars alone (M_{to}) as well as from both evolved stars and main sequence stars together (M_{ms}) are compared in the figure. To highlight their importance, we have assumed that the main sequence stellar winds are effectively thermalized and mixed within the cluster (i.e., $f_{\mathrm{ms}} = 1$). While there is observational evidence that metallicity does not strongly impact the mass loss rate of main sequence stars (McDonald and van Loon, 2007; Sloan *et al.*, 2008), stellar wind velocities are found to scale with metallicity (Marshall *et al.*, 2004). This explains the Z-dependence observed in Figure 6.2.

6.4 The Role of Stellar Wind Heating

Within a cluster, main sequence stellar members are far more prevalent than evolved stars and, as a result, their contribution to the heating of the intracluster environment should be taken into account (Smith, 1999). Employing spherically symmetric one-dimensional hydrodynamical simulations, we investigate the state of the intracluster gas, whose evolution is mediated by energy and mass injection by both the main sequence and evolved stellar populations. The injection of energy by a much less abundant, yet more individually energetic, population of millisecond pulsars will not be examined until Section 6.5. The thermalization and mixing of the main sequence stellar winds is regulated in our simulations by the efficiency $f_{\rm ms}$, with a range of $[0, 1]$, where 0 represents a complete lack of thermalization and mixing, while 1 denotes a perfectly thermalized, mixed wind contribution from the main sequence stars. Modeling the cluster masses, core radii, and velocity dispersions for specific clusters, we are able to compare our computational results to density constraints determined by observation.

The simulation results for cluster parameters set to match that of the Galactic globular clusters M15 are shown in Figure 6.3. A cluster mass of $M_{\rm c} = 4.4 \times 10^5 \, M_{\odot}$ (McNamara *et al.*, 2004) and a cluster velocity dispersion of $\sigma_v = 28$ km s^{-1} (Harris, 1996) was employed. Figure 6.3 displays the free electron density, neutral hydrogen density, temperature, and wind flow velocity profiles, where dashed lines indicate the electron and neutral hydrogen upper limits from Freire *et al.* (2001b) and Anderson (1993), respectively. Here, electron and neutral hydrogen fractions are determined with the assumption that the gas is in collisional equilibrium, and thus, the electron gas fraction is dependent upon the temperature alone. This amounts to solving for $n_{\rm e}$

and $n_{\rm H} = n_{\rm H_{tot}} + n_{\rm H+}$ in the collisional equilibrium equation $\alpha_{\rm rec}(T) n_{\rm e} n_{\rm H+} = C_{\rm ci}(T) n_{\rm e} n_{\rm H_{tot}}$, where the recombination coefficient, $\alpha_{\rm rec}(T)$, and the collisional ionization coefficient, $C_{\rm ci}(T)$ are functions of the temperature of the gas, T (Hummer and Storey, 1987; Padmanabhan, 2000). The black region in this figure illustrates the parameter space for models where with $0 \lesssim f_{\rm ms} < 0.15$, while the pink region depicts the parameter space where $0.15 < {\rm f_{ms}} \lesssim 1$. The figure shows that only models with $f_{\rm ms} > 0.15$ provide results that are consistent with observational constraints. Consequently, the low gas and dust levels observed in this cluster can be explained solely by the main sequence star heating if at least 15% of their emanating stellar winds are effectively thermalized and mixed with those of the evolved population.

Similarly, the simulation results for a cluster created to match the characteristics of 47 Tucanae are shown in Figure 6.4. We employed a cluster mass of $M_{\rm c} = 6.4 \times 10^5\, M_{\odot}$ (Marks and Kroupa, 2010) and cluster velocity dispersion $\sigma_{\rm v} = 27\,{\rm km\,s^{-1}}$ (Bianchini *et al.*, 2013). The resulting free electron density, neutral hydrogen density, temperature, and wind flow velocity profiles for the state of the intracluster gas in Galactic globular cluster 47 Tucanae are shown in Figure 6.4, where dashed lines represent the free electron and neutral hydrogen upper limits taken from Freire *et al.* (2001b) and Smith *et al.* (1990), respectively. The black region in this figure illustrates the parameter space for models where with $0 \lesssim f_{\rm ms} < 0.20$, while the pink region depicts the parameter space where $0.20 < f_{\rm ms} \lesssim 1$. It is evident that only heating models with $f_{\rm ms} > 0.20$ provide results that are consistent with current observational constraints. Thus, in order to explain the low gas and dust levels observed in this cluster solely by the heating supplied from main sequence members, a minimum of 20% of the stellar winds must be effectively thermalized and mixed into the cluster environment. Modeling 47 Tucane is of

significant importance, since after nearly half a century of searching, the first ever detection of ionized intracluster gas took place here. This constraint strongly limits the allowed values of $f_{\rm ms}$.

In Figures 6.3 and 6.4 we have examined the free electron density $n_{\rm e}$ profiles, however we will be shifting our focus to the average density within the cluster's core $\bar{n}_{\rm e}$ as we compare the observationally allowed values of $f_{\rm ms}$ among different globular clusters. We have discussed the results of 47 Tucanae and M15, which happen to have similar velocity dispersions despite 47 Tucanae being about 1.45 times more massive. Comparing the four clusters in our sample we see that the velocity dispersion has a larger spread in values, while the masses are more similar. Additionally, Naiman *et al.* (2011) found that the cluster mass was less critical for gas retention when compared to the impact arising from changes in the velocity dispersion. Motivated by this, we have chosen to fix the cluster mass in an effort to systematically explore the effects of changing the velocity dispersion on the average free electron density $\bar{n}_{\rm e}$ and the average neutral hydrogen density $\bar{n}_{\rm H}$.

Figure 6.5 displays the results of our effort to illustrate in more general terms how $\bar{n}_{\rm e}$ and $\bar{n}_{\rm H}$ change with velocity dispersion and $f_{\rm ms}$ for a cluster of fixed mass. As expected, we see that in general a larger cluster velocity dispersion results in an increase in density for both $\bar{n}_{\rm e}$ and $\bar{n}_{\rm H}$. Figure 6.5 also indicates that the average free electron density is relatively independent of the stellar wind thermalization and mixing fraction, while the average neutral hydrogen density is more sensitive to changes in $f_{\rm ms}$. At low velocity dispersions, the majority of the gas is easily removed from the cluster's potential regardless of the amount of main sequence heating, leading to the low electron and hydrogen number densities for $\sigma \lesssim 30\,{\rm km\ s^{-1}}$. As the velocity

dispersion increases, more material is funneled toward the central regions of the cluster, and for high enough dispersions, this gas effectively cools as it collects in the cluster's core. Because in this approximation the electron fraction is a function of temperature alone, the large central density enhancements which lead to large neutral hydrogen enhancements in the center result in relatively low electron fractions.

In Figure 6.6, we model the four clusters 47 Tucanae, M15, NGC 6440, and NGC 6752, where cluster masses and velocity dispersions are taken from Marks and Kroupa (2010) and Bianchini *et al.* (2013) for 47 Tucanae, McNamara *et al.* (2004) and Harris (1996) for M15, and Gnedin *et al.* (2002) for NGC 6440 and NGC 6752. With these parameters, we can explore the dependence of the free electron density and neutral hydrogen density, both averaged over the cluster core, on the stellar wind thermalization and mixing fraction. The density constraints shown in Figure 6.6 are from Anderson (1993), Freire *et al.* (2001b), Smith *et al.* (1990), Hui *et al.* (2009) and D'Amico *et al.* (2002). The density profiles from each of the four clusters are consistent with the strictest wind thermalization and mixing constraint, $f_{\rm ms} \gtrsim 0.5$, determined by the detection of ionized gas in 47 Tucanae, and displayed as the *shaded green* region in Figure 6.6 (Freire *et al.*, 2001b).

In summary, our models indicate that heating from the evolved and main sequence winds is essential in explaining the low density gas and dust observed in globular clusters and that a minimum of about $2/5$ of the total stellar wind luminosity must effectively be thermalized and mixed into the cluster environment to provide an accurate description of current observational constraints. It is important to recognize that $f_{\rm ms}$ is the fraction of the total amount of energy injected by the main sequence stellar members, which has been calculated here using

MESA. Consequently, the constraints we have derived on $f_{\rm ms}$ are relative in the sense that their definition depends on the exact value of the total injected energy, which is uncertain (Figure 6.2).

6.5 The role of pulsar Heating: The case of 47 Tucanae

The role of pulsar heating in the evacuation of gas and dust in globular clusters was first discussed by Spergel (1991). At that time the total number of detected millisecond pulsars residing in globular clusters was about two dozen. We now know of over 140 millisecond pulsars in 28 separate globular clusters (Freire, 2013). In some of these clusters the population of millisecond pulsars is considerable. Globular cluster Terzan 5 is known to harbor 34 millisecond pulsars and 47 Tucanae contains 23 detected pulsars[1]. In our hydrodynamical models, 47 Tucanae is used as a proxy to explore the physics of gas retention in clusters hosting a population of millisecond pulsars. This cluster was chosen because of the detection of ionized intracluster material (Freire *et al.*, 2001b), which allows for strict constraints on the efficiency of pulsar heating to be placed.

The hydrodynamical influence of millisecond pulsars in our simulations is restricted to energy injection, $q_{\varepsilon,\Omega}(r,t)$, as the stellar winds dominate the mass supply. For simplicity we assume that $q_{\varepsilon,\Omega}(r) \propto n_{\rm p}(r)$. As pulsar energy is predominately supplied as Poynting flux, the thermalization and mixing efficiency within the cluster core remains highly uncertain. In addition, also uncertain is the total amount of energy, $\dot{E}_{\Omega}$, injected into the cluster. This uncertainty is largely due to unreliable timing solutions. For this reason, the total energy injected by the pulsars that is effectively thermalized and mixed into the cluster gas, $\dot{E}_{\rm p}$, is treated as a free

[1] http://www.naic.edu/~pfreire/GCpsr.html

parameter and is parameterized here as $\dot{E}_{\rm p} = f_{\rm p}\dot{E}_{\rm ms}$.

There are currently 16 millisecond pulsars within 47 Tucanae with known timing solutions. If we, for example, take the timing solutions at face value (Manchester *et al.*, 1990, 1991; Robinson *et al.*, 1995; Camilo *et al.*, 2000; Edmonds *et al.*, 2001; Freire *et al.*, 2001a; Edmonds *et al.*, 2002; Freire *et al.*, 2003; Lorimer *et al.*, 2003; Bogdanov *et al.*, 2005), ignoring the likely possibility that they might be corrupted by cluster motions, we find a total spin-down luminosity of $\dot{E}_{\Omega} = 5.4 \times 10^{35}$ erg s^{-1}, which corresponds to $f_{\rm p} = 24.4$ under the assumption that all of the spin down luminosity is effectively thermalized (i.e., $\dot{E}_{\rm p} = \dot{E}_{\Omega}$). This would indicate an energy injection by the pulsar population that is 24.4 times larger than that added by the main sequence stellar winds. If, on the other hand, we assume that the luminosity distribution of millisecond pulsars residing in the cluster is well described by the luminosity function of Galactic field pulsars (Manchester *et al.*, 2005), we obtain $\dot{E}_{\Omega} = 5 \times 10^{34}$ erg s^{-1}, which is an order of magnitude smaller than the total power estimated using 47 Tucanae's pulsar timing parameters.

Figure 6.7 shows the free electron density, neutral hydrogen density, temperature, and flow velocity radial profiles for a cluster modeled after 47 Tucanae when heating from the millisecond pulsar population is included. In this figure, heating from the main sequence winds is not considered. Contrasting the resulting density profiles to the upper limits for 47 Tucanae, we can determine the critical level of heating required to account for the observed gas densities, assuming this evacuation mechanism worked in isolation. The pulsar heating fraction $f_{\rm p}$ is normalized here to the main sequence heating rate, where $f_{\rm p} = 1$ corresponds to the total amount of heating from the millisecond pulsar winds being equal to that expected to

be supplied by main sequence stars. Models with $f_{\rm p} \approx 4.1 \times 10^{-2}$ are consistent with the free electron and neutral hydrogen density constraints. Other models shown in Figure 6.7 result in gas that is either too cold and dense (*black* line) or too hot and diffuse (*red* line) when compare to observations. We conclude that the pulsar energy injection needs to be much lower than the stellar wind contribution and, as a result, the currently poorly understood pulsar wind thermalization efficiency within the cluster's core must be small. This can be clearly seen in Figure 6.8 by comparing the thermodynamical profiles generated by models that include pulsar heating with those that use main sequence stellar winds as the dominant energy injection mechanism. On the condition that the millisecond pulsars inject 5×10^{34}erg s^{-1}, as inferred from the Galactic field population, the thermalization efficiency needs to be $\lesssim 1.7\%$. If the thermalization efficiency within the cluster's core was larger than this value, the observational constraints will be violated.

In Figure 6.9 we consider a more realistic scenario in which heating from both the main sequence stars and the millisecond pulsar populations is included. In this case, we search for models that produce thermodynamical profiles with average central electron and neutral hydrogen densities that are consistent with observational constraints when energy injection from both pulsars and stellar winds is taken into account. The blue-grey shaded regions in Figure 6.9 denote the parameter space that fall within the density constraints for 47 Tucanae. It is important to note the low levels of millisecond pulsar energy thermalization needed to explain the density limits even when the heating from the main sequence stellar winds is negligible. This is because of the overabundance of millisecond pulsars residing in the core of 47 Tucanae, which helps prevent the intracluster gas from being effectively retained in the cluster. As such, we conclude

that current observations place strong constraints on the ability of pulsar winds to effectively thermalize and mix within cluster's cores.

6.6 Discussion

In this Chapter, we examine tenable gas evacuation mechanisms in an effort to account for the paucity of gas and dust in globular clusters. The tenuity of the intracluster medium is observed consistently from cluster to cluster and, as such, we aim to distinguish a mechanism that is universal in scope and not specific to variable cluster properties, such as, for example, UV heating from the HB stars (Vandenberg and Faulkner, 1977) or stellar collisions (Umbreit *et al.*, 2008). Energy injection by main sequence stellar members within a cluster is generally dismissed, primarily due to the fact that the energy contribution per star is low when compared to explosive processes, such hydrogen rich novae (Scott and Durisen, 1978; Moore and Bildsten, 2011), and the heat input from individual evolved stars. We argue that the sheer abundance of the main sequence stellar members warrants this mechanism worthy of consideration. To this end, we construct one dimensional hydrodynamical models to study the properties of the gas in globular clusters with mass and energy injection provided by both the evolved and main sequence stellar populations. Choosing our initial conditions to match the cluster masses and core radii of globular clusters 47 Tucanae, M15, NGC 6440, and NGC 6752, we are able to compare our simulation results with observational density constraints. We find that a minimum of approximately 2/5 of the total stellar wind luminosity, which we calculate using `MESA` stellar evolution models, must be effectively thermalized and mixed into the cluster medium in order

to generate results that are in agreement with current limits. We conclude that the energy output from the main sequence stellar population alone is capable of effectively sweeping out the evolved stellar ejecta in all the systems we have modeled. Specifically, we argue this result distinguishes a viable ubiquitous gas and dust evacuation mechanism for globular clusters. It is important to note that given current mass-loss uncertainties it is difficult to precisely quantify the fraction of effectively thermalized and mixed hot main sequence winds. However, it is clear that on the basis of commonly used mass-loss rate prescriptions, we expect energy injection from main sequence stars to play a vital role in regulating gas retention in globular clusters.

We extend our computational analysis to investigate the efficiency of pulsar wind feedback in a simulation modeled after the globular cluster 47 Tucanae, which is known to harbor 23 millisecond pulsars. The detection of intracluster ionized intracluster gas within 47 Tucanae allows for a detailed comparison between simulated results and the strict observational density constraints. The millisecond pulsar energy injection is known to be rather significant and, as such, we conclude that the pulsar wind thermalization efficiency must be extremely low in order to maintain the low density constraints for this cluster. Other clusters of interest in our analysis, M15, NGC 6440, and NGC 6752, are known to a host smaller populations of 8, 6, and 5 millisecond pulsars, respectively. While there is a high variability in the total pulsar energy injection per cluster, all observations indicate a tenuous intracluster medium. We argue that, when present, the millisecond pulsar population is rather ineffective at clearing gas within the cluster's core. The heat supplied by millisecond pulsars within a globular cluster is difficult to estimate, mainly due to the highly uncertain thermalization and mixing efficiency of the emanating Poynting flux within the core of the cluster. What needs to be demonstrated, perhaps

by means of three dimensional, magneto-hydrodynamical simulations, is that pulsar outflows are not efficiently *poisoned* by the baryons emanating from the evolved stars by the time that they reach the edge of the cluster. We suspect, based on current observational constraints, that the pulsar wind energy is only efficiently thermalized at much larger radii. Observations of globular clusters with accompanying X-ray haloes support this idea (Mirabal, 2010). In addition, it has been suggested by Hui *et al.* (2009) that while the luminous X-ray pulsar wind nebulae have been detected from pulsars in the Galaxy, there is no evidence of a contribution to the diffuse X-ray emission by pulsar wind nebulae within globular clusters. Searching for low and high energy diffuse emission within and around pulsar-hosting globular clusters could, in principle, help uncovered the heating structures from these objects and provide a much clearer understanding of the underlying processes at work.

Our understanding of the intracluster medium has come a long way since observations revealed a dearth of gas within clusters over half a century ago, yet these gas-deficient systems continue to offer major puzzles and challenges. The modeling of mass retention in such dense stellar systems continues to be a formidable challenge to theorists and to computational techniques. The best prospects probably lie with performing three-dimensional (magneto)hydrodynamical simulations of the interaction of main sequence winds, evolved stellar winds and, when present in sizable numbers, pulsar winds. It is also a challenge for observers, in their quest for detecting the signatures of gas in extremely diffuse environments. Forthcoming space- and ground-based observations should provide the evidence necessary to unveil the detailed nature of the intracluster gas.

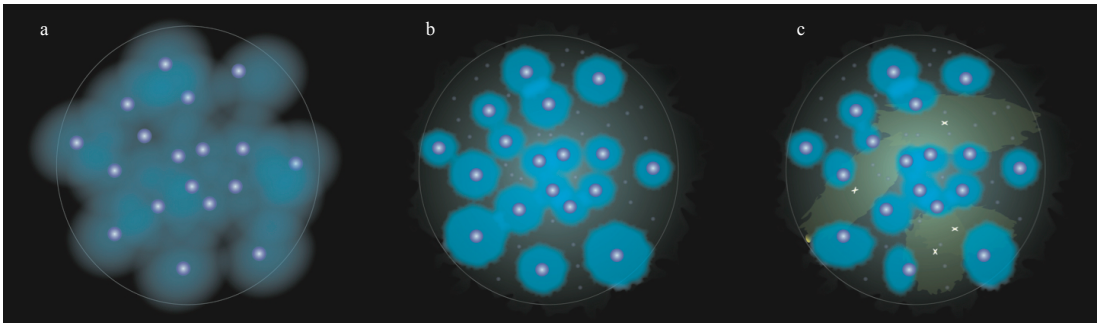

Figure 6.1: Diagram illustrating the different mass and energy contributions arising from main sequence stars, evolved stars and pulsar winds. If evolved stars dominate the mass and energy injection, a lower limit on the gas density can be calculated by assuming that their emanating winds extend only to their closest neighbors (panel *a*). While the evolved stellar members are expected to dominate the mass injection, despite comprising a small subset of the stellar cluster population, the energy injection is likely to be dominated by the more abundant main sequence stars (panel *b*) and, in some clusters, by millisecond pulsar winds (panel *c*). A significant amount of energy injection could prevent the winds from the evolved stellar members from effectively expanding between closest neighbors, resulting in lower gas content. This is illustrated in panels *b* and *c* when the energy injection is dominated by main sequence stars and pulsar winds, respectively.

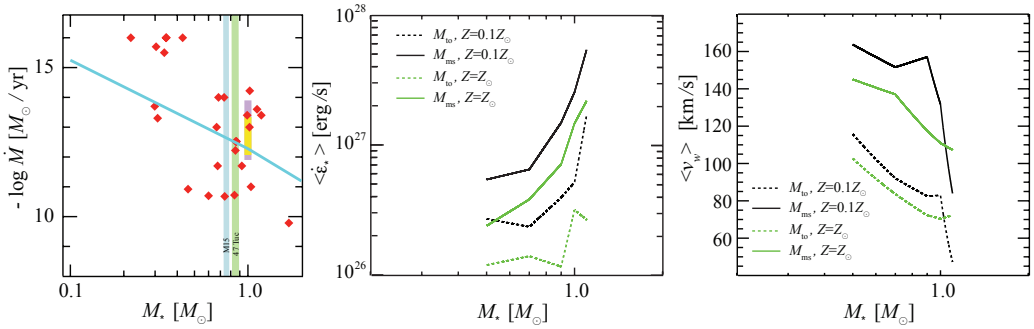

Figure 6.2: The relationship between stellar mass loss rates and energy injection in globular clusters as a function of the population's turn-off mass. *Left Panel*: The mass loss rate estimates along the main sequence are plotted as a function of the turn-off mass of the stellar population. The *light blue* line shows our model inputs from MESA, while the *diamond* symbols show a compilation of observed mass loss rates (Cranmer and Saar, 2011; de Jager *et al.*, 1988; Searle *et al.*, 2008; Waters *et al.*, 1987; Debes, 2006; Badalyan and Livshits, 1992; Morin *et al.*, 2008). The *yellow* rectangular region shows the estimated changes in the mass loss rate of the Sun over the past 1-5 Gyrs while the *purple* rectangular region illustrates the variability in the mass loss rate as derived by the solar X-ray activity (Wood *et al.*, 2005; Cohen, 2011). It is important to note that not only do different stars demonstrate variability in mass loss rates, but this rate can also vary in individual stars themselves. This motivates the need for a normalized mass loss prescription, as it would not be possible to accurately model the variability in our cluster sample. The *blue* and *green* vertical shaded regions shows the approximate age range estimated for M15 and 47 Tucanae, respectively. *Middle Panel:* The injected luminosities per star are plotted as a function of the stellar population's turn-off mass and metallicity. The energy injection has been calculated using the contribution of the turn-off mass stars alone ($M_{\rm to}$) as well as adding the main sequence stellar contribution ($M_{\rm ms}$) for which we have assumed perfect thermalization and mixing, $f_{\rm ms} = 1$. *Right Panel:* The corresponding average stellar wind velocity per star is shown as a function of the stellar population's turn-off mass and metallicity. In both *middle* and *right* panels the *dotted green* lines represents stars with solar metallicity $Z = Z_\odot$ and the *dotted black* lines denote stars with $Z = Z_\odot/10$.

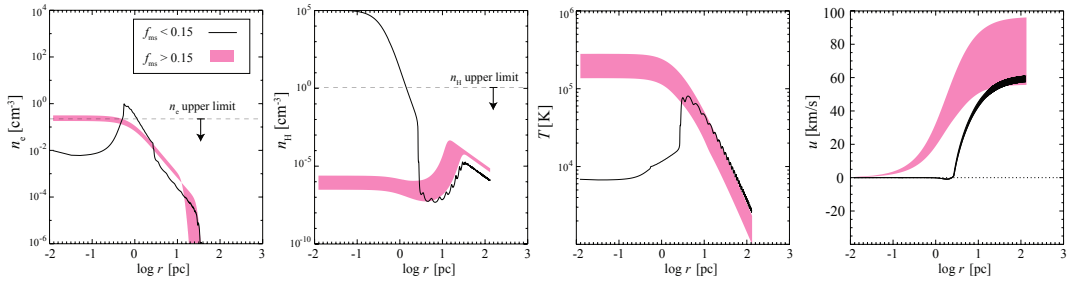

Figure 6.3: The state of the intracluster gas in the globular cluster M15 calculated using one-dimensional hydrodynamical simulations. Shown are the radial profiles of the electron n_e and neutral hydrogen n_H densities, the temperature T and the flow velocity u. The simulation assumes energy and mass injection is determined solely by main sequence and evolved stars. The main sequence stellar wind thermalization and mixing efficiency within the cluster is regulated by f_{ms}, whose range is $[0,1]$. The dashed lines show the electron and neutral hydrogen upper limits from Freire *et al.* (2001b) and Anderson (1993), respectively. To model M15 we employ $M_c = 4.4 \times 10^5 M_\odot$ (McNamara *et al.*, 2004) and $\sigma_v = 28$ km s^{-1} (Harris, 1996). *Thin black* regions display models with $0 \lesssim f_{ms} < 0.15$, while *pink* regions depict models with $0.15 < f_{ms} \lesssim 1$. We find that only heating models with $f_{ms} > 0.15$ give results consistent with current observational constraints.

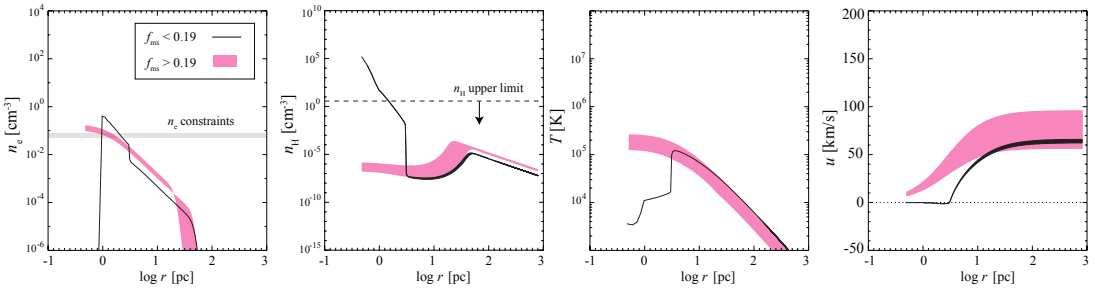

Figure 6.4: The state of the intracluster gas in the globular cluster 47 Tucanae calculated using one-dimensional hydrodynamical simulations. The radial profiles of the electron n_e and neutral hydrogen n_H densities, the temperature T and the flow velocity u assumes energy and mass injection is determined solely by main sequence and solved stars. The main sequence stellar wind thermalization and mixing efficiency within the cluster is regulated by f_{ms}, whose range is $[0,1]$. Electron and neutral hydrogen upper limits are denoted by the dashed line and are taken from Freire *et al.* (2001b) and Smith *et al.* (1990), respectively. To model 47 Tucanae we employ $M_c = 6.4 \times 10^5 M_\odot$ (Marks and Kroupa, 2010) and $\sigma_v = 27$ km s^{-1} (Bianchini *et al.*, 2013). *Thin black* regions depict models with $0 \lesssim f_{ms} < 0.20$, while *pink* regions depict models with $0.20 < f_{ms} \lesssim 1$. We find that results are consistent with current observations only in heating models with $f_{ms} > 0.20$.

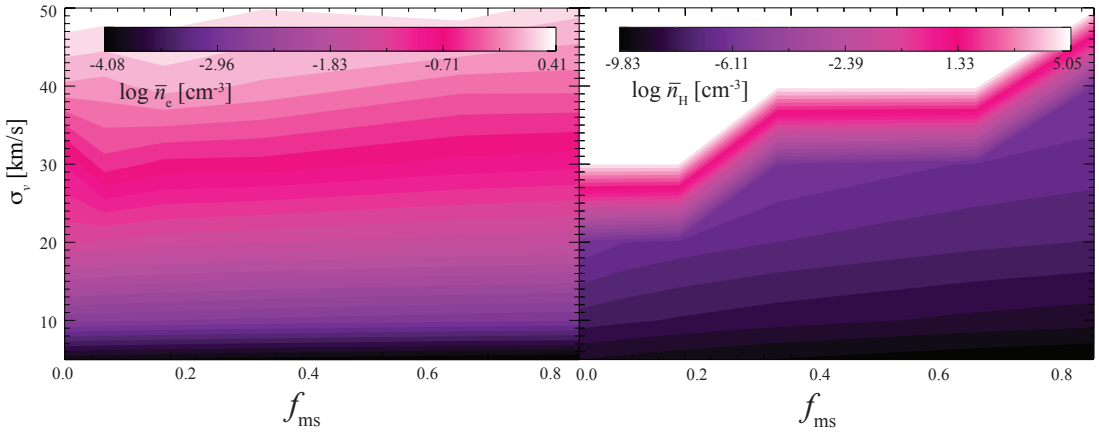

Figure 6.5: The relationship between a changing main sequence wind thermalization and mixing fraction $f_{\rm ms}$ and cluster velocity dispersion σ_v on the free electron density $n_{\rm e}$ (*left panel*) and $n_{\rm H}$ (*right panel*) averaged over the core. In both panels, the cluster mass was held at a constant value, $M_{\rm c} = 5 \times 10^5\, M_\odot$.

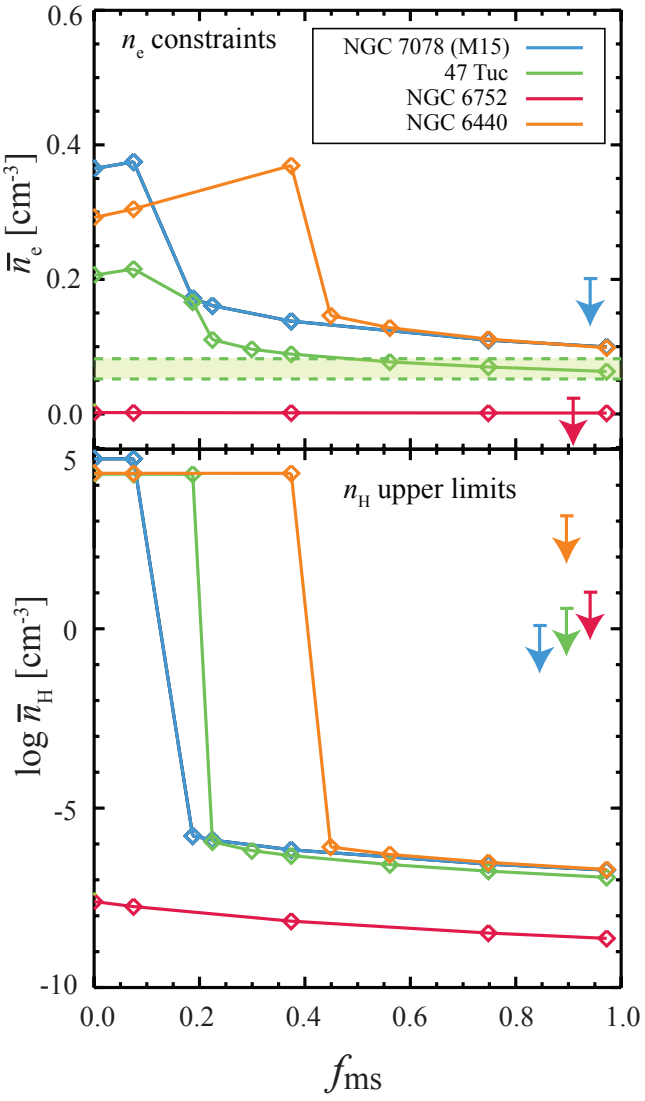

Figure 6.6: Free electron and neutral hydrogen densities, averaged over the cluster core, as a function of main sequence wind thermalization and mixing fraction for globular clusters 47 Tucanae, M15, NGC 6440, and NGC 6752. Upper limits are taken from Anderson (1993), Freire *et al.* (2001b), Smith *et al.* (1990), Hui *et al.* (2009), D'Amico *et al.* (2002). All of the profiles are consistent with the tightest stellar wind thermalization and mixing constraint of $f_{ms} \gtrsim 0.5$, provided by the 47 Tucanae electron density limits, and denoted in the figure by the *shaded green* region (Freire *et al.*, 2001b). The cluster mass and velocity dispersion values are taken from Marks and Kroupa (2010) and Bianchini *et al.* (2013) for 47 Tucanae, McNamara *et al.* (2004) and Harris (1996) for M15, and Gnedin *et al.* (2002) for NGC 6440 and NGC 6752.

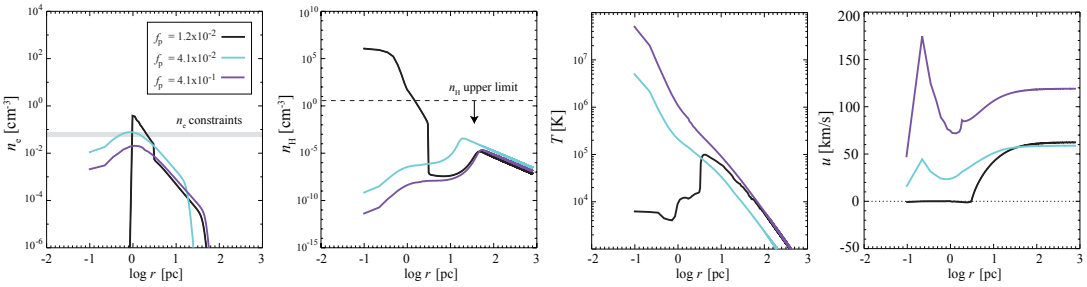

Figure 6.7: The state of the intracluster gas in the globular cluster 47 Tucanae, when only heating from the millisecond pulsar population is included. Shown are the radial profiles of the free electron density n_e, neutral hydrogen density n_H, temperature T, and flow velocity u, calculated using one-dimensional hydrodynamical simulations. Free electron and neutral hydrogen density limits are taken from Freire *et al.* (2001b) and Smith *et al.* (1990). The pulsar heating, represented by $\dot{E}_p = f_p \dot{E}_{ms}$, is normalized to the main sequence heating rate. Only models with $f_p \approx 4.1 \times 10^{-2}$ are consistent with the density constraints. The other models produce gas that is either too cool and dense (*black line*) or too hot and diffuse (*red line*) when compare with the observational limits.

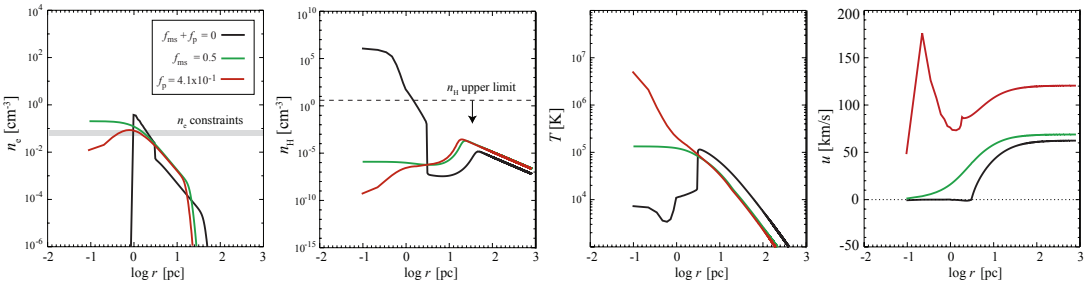

Figure 6.8: The state of the intracluster gas in the globular cluster 47 Tucanae as modified by heating from either the main sequence or the millisecond pulsar population. Shown are the radial profiles of the free electron density n_e, neutral hydrogen density n_H, temperature T, and flow velocity u, calculated using one-dimensional hydrodynamical simulations. Free electron and neutral hydrogen density limits are taken from Freire *et al.* (2001b) and Smith *et al.* (1990). The pulsar heating fractions, represented by f_p, are normalized to the main sequence heating rate.

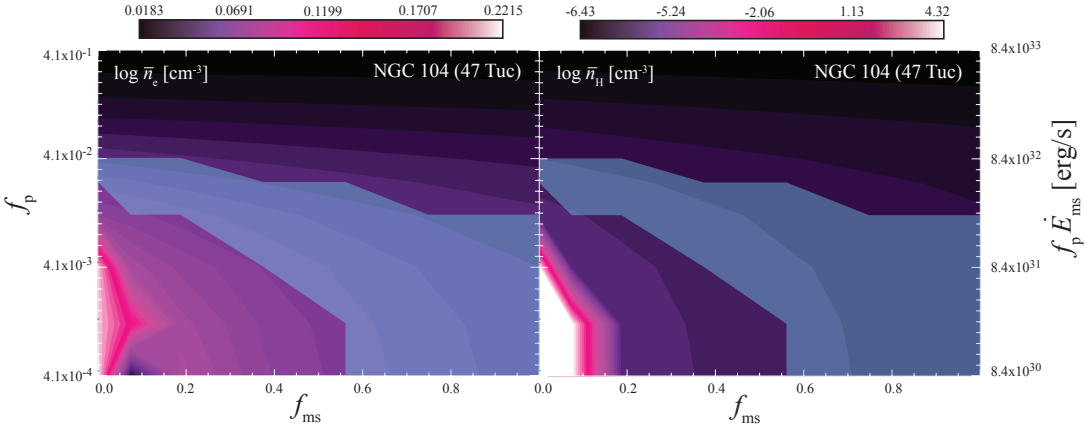

Figure 6.9: The state of the free electron density n_e and neutral hydrogen density n_H averaged over the core of the cluster as a function of millisecond pulsar heating and energy injection from the stellar winds for globular cluster 47 Tucanae. The *blue-grey* shaded denotes regions where our model is within the density constraints found by Freire *et al.* (2001b) and Smith *et al.* (1990). Note that our model places stringent constraints on the thermalization efficiency of pulsar winds in the core of 47 Tucanae.

Bibliography

Abbott, D. C. The terminal velocities of stellar winds from early-type stars. ApJ **225**, 893 (1978).

Adén, D.; Wilkinson, M. I.; Read, J. I.; Feltzing, S.; Koch, A.; Gilmore, G. F.; Grebel, E. K. and Lundström, I. A New Low Mass for the Hercules dSph: The End of a Common Mass Scale for the Dwarfs? ApJ **706**, L150 (2009).

Anderson, J. and van der Marel, R. P. New Limits on an Intermediate Mass Black Hole in Omega Centauri: I. Hubble Space Telescope Photometry and Proper Motions. *ArXiv e-prints* (2009).

Anderson, S. B. *A study of recycled pulsars in globular clusters*. Ph.D. thesis, California Institute of Technology, Pasadena. (1993).

Anglés-Alcázar, D.; Özel, F. and Davé, R. Black Hole-Galaxy Correlations without Self-regulation. ApJ **770**, 5 (2013).

Badalyan, O. G. and Livshits, M. A. Mass loss by active late-type stars. AZh **69**, 138 (1992).

Barai, P.; Viel, M.; Murante, G.; Gaspari, M. and Borgani, S. Kinetic or thermal AGN feedback in simulations of isolated and merging disc galaxies calibrated by the M-σ relation. MNRAS **437**, 1456 (2014).

Barmby, P.; Boyer, M. L.; Woodward, C. E.; Gehrz, R. D.; van Loon, J. T.; Fazio, G. G.; Marengo, M. and Polomski, E. A Spitzer Search for Cold Dust Within Globular Clusters. AJ **137**, 207 (2009).

Baumgardt, H.; Hut, P.; Makino, J.; McMillan, S. and Portegies Zwart, S. On the Central Structure of M15. ApJ **582**, L21 (2003a).

Baumgardt, H.; Hut, P.; Makino, J.; McMillan, S. and Portegies Zwart, S. On the Central Structure of M15. ApJ **582**, L21 (2003b).

Baumgardt, H.; Makino, J.; Hut, P.; McMillan, S. and Portegies Zwart, S. A Dynamical Model for the Globular Cluster G1. ApJ **589**, L25 (2003c).

Beasley, M. A.; Brodie, J. P.; Strader, J.; Forbes, D. A.; Proctor, R. N.; Barmby, P. and Huchra, J. P. The Chemical Properties of Milky Way and M31 Globular Clusters. II. Stellar Population Model Predictions. AJ **129**, 1412 (2005).

Bianchini, P.; Varri, A. L.; Bertin, G. and Zocchi, A. Rotating Globular Clusters. ApJ **772**, 67 (2013).

Birkinshaw, M.; Ho, P. T. P. and Baud, B. A search for neutral hydrogen near nine globular clusters. A&A **125**, 271 (1983).

Blecha, L.; Loeb, A. and Narayan, R. Double-peaked narrow-line signatures of dual supermassive black holes in galaxy merger simulations. MNRAS **429**, 2594 (2013).

Bloecker, T. Stellar evolution of low and intermediate-mass stars. I. Mass loss on the AGB and its consequences for stellar evolution. A&A **297**, 727 (1995).

Blondin, J. M. and Pope, T. C. Revisiting the "Flip-Flop" Instability of Hoyle-Lyttleton Accretion. ApJ **700**, 95 (2009).

Bode, M. F. and Evans, A. *Classical Novae* (2008).

Bogdanov, S.; Grindlay, J. E. and van den Berg, M. An X-Ray Variable Millisecond Pulsar in the Globular Cluster 47 Tucanae: Closing the Link to Low-Mass X-Ray Binaries. ApJ **630**, 1029 (2005).

Böker, T. The HST Census of Nuclear Star Clusters in Late-type Spirals. In Geisler, D. P.; Grebel, E. K. and Minniti, D., eds., *Extragalactic Star Clusters* (2002), vol. 207 of *IAU Symposium*, p. 706.

Böker, T. Nuclear star clusters. In de Grijs, R. and Lépine, J. R. D., eds., *IAU Symposium* (2010), vol. 266 of *IAU Symposium*, pp. 58–63.

Böker, T.; Sarzi, M.; McLaughlin, D. E.; van der Marel, R. P.; Rix, H.-W.; Ho, L. C. and Shields, J. C. A Hubble Space Telescope Census of Nuclear Star Clusters in Late-Type Spiral Galaxies. II. Cluster Sizes and Structural Parameter Correlations. AJ **127**, 105 (2004).

Bondi, H. On spherically symmetrical accretion. MNRAS **112**, 195 (1952).

Bondi, H. and Hoyle, F. On the mechanism of accretion by stars. MNRAS **104**, 273 (1944).

Booth, C. M. and Schaye, J. Cosmological simulations of the growth of supermassive black holes and feedback from active galactic nuclei: method and tests. MNRAS **398**, 53 (2009).

Bowers, P. F.; Kerr, F. J.; Knapp, G. R.; Gallagher, J. S. and Hunter, D. A. Upper limits on the gas content of southern globular clusters. ApJ **233**, 553 (1979).

Boyer, M. L.; McDonald, I.; Loon, J. T.; Woodward, C. E.; Gehrz, R. D.; Evans, A. and Dupree, A. K. A Spitzer Space Telescope Atlas of ω Centauri: The Stellar Population, Mass Loss, and the Intracluster Medium. AJ **135**, 1395 (2008).

Boyer, M. L.; Woodward, C. E.; van Loon, J. T.; Gordon, K. D.; Evans, A.; Gehrz, R. D.; Helton, L. A. and Polomski, E. F. Stellar Populations and Mass Loss in M15: A Spitzer Space Telescope Detection of Dust in the Intracluster Medium. AJ **132**, 1415 (2006).

Brandl, B. R.; Clark, D. M.; Eikenberry, S. S.; Wilson, J. C.; Henderson, C. P.; Barry, D. J.; Houck, J. R.; Carson, J. C. and Hayward, T. L. Deep Near-Infrared Imaging and Photometry of the Antennae Galaxies with WIRC. ApJ **635**, 280 (2005a).

Brandl, B. R.; Clark, D. M.; Eikenberry, S. S.; Wilson, J. C.; Henderson, C. P.; Barry, D. J.; Houck, J. R.; Carson, J. C. and Hayward, T. L. Deep Near-Infrared Imaging and Photometry of the Antennae Galaxies with WIRC. ApJ **635**, 280 (2005b).

Brüns, R. C.; Kroupa, P. and Fellhauer, M. Faint Fuzzy Star Clusters in NGC 1023 as Remnants of Merged Star Cluster Complexes. ApJ **702**, 1268 (2009a).

Brüns, R. C.; Kroupa, P. and Fellhauer, M. Faint Fuzzy Star Clusters in NGC 1023 as Remnants of Merged Star Cluster Complexes. ApJ **702**, 1268 (2009b).

Caldwell, N.; Schiavon, R.; Morrison, H.; Rose, J. A. and Harding, P. Star Clusters in M31. II. Old Cluster Metallicities and Ages from Hectospec Data. AJ **141**, 61 (2011).

Caloi, V. and D'Antona, F. NGC 6441: another indication of very high helium content in globular cluster stars. A&A **463**, 949 (2007).

Camilo, F.; Lorimer, D. R.; Freire, P.; Lyne, A. G. and Manchester, R. N. Observations of 20 Millisecond Pulsars in 47 Tucanae at 20 Centimeters. ApJ **535**, 975 (2000).

Carretta, E.; Bragaglia, A.; Gratton, R. G.; Recio-Blanco, A.; Lucatello, S.; D'Orazi, V. and Cassisi, S. Properties of stellar generations in globular clusters and relations with global parameters. A&A **516**, A55 (2010a).

Carretta, E.; Bragaglia, A.; Gratton, R. G.; Recio-Blanco, A.; Lucatello, S.; D'Orazi, V. and Cassisi, S. Properties of stellar generations in globular clusters and relations with global parameters. A&A **516**, A55 (2010b).

Choi, E.; Naab, T.; Ostriker, J. P.; Johansson, P. H. and Moster, B. P. Consequences of Mechanical and Radiative Feedback from Black Holes in Disc Galaxy Mergers. *ArXiv e-prints* (2013).

Choi, E.; Ostriker, J. P.; Naab, T. and Johansson, P. H. Radiative and Momentum-based Mechanical Active Galactic Nucleus Feedback in a Three-dimensional Galaxy Evolution Code. ApJ **754**, 125 (2012).

Cohen, N. L. and Malkan, M. A. A search for H2O maser emission from globular clusters. AJ **84**, 74 (1979).

Cohen, O. The independency of stellar mass-loss rates on stellar X-ray luminosity and activity level based on solar X-ray flux and solar wind observations. MNRAS **417**, 2592 (2011).

Coleman, G. D. and Worden, S. P. Large-scale winds driven by flare-star mass loss. ApJ **218**, 792 (1977).

Conroy, C. On the Birth Masses of the Ancient Globular Clusters. ApJ **758**, 21 (2012).

Conroy, C. and Spergel, D. N. On the Formation of Multiple Stellar Populations in Globular Clusters. ApJ **726**, 36 (2011).

Cottrell, P. L. and Da Costa, G. S. Correlated cyanogen and sodium anomalies in the globular clusters 47 TUC and NGC 6752. ApJ **245**, L79 (1981).

Cranmer, S. R. and Saar, S. H. Testing a Predictive Theoretical Model for the Mass Loss Rates of Cool Stars. ApJ **741**, 54 (2011).

Crivellari, E.; Wolter, A. and Trinchieri, G. The Cartwheel galaxy with XMM-Newton. A&A **501**, 445 (2009).

Croton, D. J.; Springel, V.; White, S. D. M.; De Lucia, G.; Frenk, C. S.; Gao, L.; Jenkins, A.; Kauffmann, G.; Navarro, J. F. and Yoshida, N. The many lives of active galactic nuclei: cooling flows, black holes and the luminosities and colours of galaxies. MNRAS **365**, 11 (2006).

Dalgarno, A. and McCray, R. A. Heating and Ionization of HI Regions. ARA&A **10**, 375 (1972).

D'Amico, N.; Possenti, A.; Fici, L.; Manchester, R. N.; Lyne, A. G.; Camilo, F. and Sarkissian, J. Timing of Millisecond Pulsars in NGC 6752: Evidence for a High Mass-to-Light Ratio in the Cluster Core. ApJ **570**, L89 (2002).

D'Antona, F. and Caloi, V. The fraction of second generation stars in globular clusters from the analysis of the horizontal branch. MNRAS **390**, 693 (2008).

de Jager, C.; Nieuwenhuijzen, H. and van der Hucht, K. A. Mass loss rates in the Hertzsprung-Russell diagram. A&AS **72**, 259 (1988).

de Silva, G. M.; Gibson, B. K.; Lattanzio, J. and Asplund, M. On and Na abundance patterns in open clusters of the Galactic disk. A&A **500**, L25 (2009).

Debes, J. H. Measuring M Dwarf Winds with DAZ White Dwarfs. ApJ **652**, 636 (2006).

Debuhr, J.; Quataert, E. and Ma, C.-P. The growth of massive black holes in galaxy merger simulations with feedback by radiation pressure. MNRAS **412**, 1341 (2011).

Debuhr, J.; Quataert, E. and Ma, C.-P. Galaxy-scale outflows driven by active galactic nuclei. MNRAS **420**, 2221 (2012).

D'Ercole, A.; D'Antona, F.; Ventura, P.; Vesperini, E. and McMillan, S. L. W. Abundance patterns of multiple populations in globular clusters: a chemical evolution model based on yields from AGB ejecta. MNRAS **407**, 854 (2010).

D'Ercole, A.; Vesperini, E.; D'Antona, F.; McMillan, S. L. W. and Recchi, S. Formation and dynamical evolution of multiple stellar generations in globular clusters. MNRAS **391**, 825 (2008).

Di Matteo, T.; Colberg, J.; Springel, V.; Hernquist, L. and Sijacki, D. Direct Cosmological Simulations of the Growth of Black Holes and Galaxies. ApJ **676**, 33 (2008).

Dickey, J. M. and Malkan, M. A. A high sensitivity search for main-line OH emission from globular clusters. AJ **85**, 145 (1980).

Diemand, J.; Kuhlen, M. and Madau, P. Formation and Evolution of Galaxy Dark Matter Halos and Their Substructure. ApJ **667**, 859 (2007).

Diemand, J.; Kuhlen, M.; Madau, P.; Zemp, M.; Moore, B.; Potter, D. and Stadel, J. Clumps and streams in the local dark matter distribution. Nature **454**, 735 (2008).

Dinescu, D. I.; Girard, T. M.; van Altena, W. F.; Mendez, R. A. and Lopez, C. E. Space velocities of southern globular clusters. I. Astrometric techniques and first results. AJ **114**, 1014 (1997).

Dull, J. D.; Cohn, H. N.; Lugger, P. M.; Murphy, B. W.; Seitzer, P. O.; Callanan, P. J.; Rutten, R. G. M. and Charles, P. A. The Dynamics of M15: Observations of the Velocity Dispersion Profile and Fokker-Planck Models. ApJ **481**, 267 (1997a).

Dull, J. D.; Cohn, H. N.; Lugger, P. M.; Murphy, B. W.; Seitzer, P. O.; Callanan, P. J.; Rutten, R. G. M. and Charles, P. A. The Dynamics of M15: Observations of the Velocity Dispersion Profile and Fokker-Planck Models. ApJ **481**, 267 (1997b).

Dull, J. D.; Cohn, H. N.; Lugger, P. M.; Murphy, B. W.; Seitzer, P. O.; Callanan, P. J.; Rutten, R. G. M. and Charles, P. A. Addendum: "The Dynamics of M15: Observations of the Velocity Dispersion Profile and Fokker-Planck Models" (<A href="/abs/1997ApJ...481..267D">ApJ, 481, 267 [1997]</A>). ApJ **585**, 598 (2003).

Dupree, A. K. and Reimers, D. Mass loss from cool stars. In Kondo, Y., ed., *Exploring the Universe with the IUE Satellite* (1987), vol. 129 of *Astrophysics and Space Science Library*, pp. 321–353.

Edgar, R. A review of Bondi-Hoyle-Lyttleton accretion. *New Astronomy Review* **48**, 843 (2004).

Edmonds, P. D.; Gilliland, R. L.; Camilo, F.; Heinke, C. O. and Grindlay, J. E. A Millisecond Pulsar Optical Counterpart with Large-Amplitude Variability in the Globular Cluster 47 Tucanae. ApJ **579**, 741 (2002).

Edmonds, P. D.; Gilliland, R. L.; Heinke, C. O.; Grindlay, J. E. and Camilo, F. Optical Detection of a Variable Millisecond Pulsar Companion in 47 Tucanae. ApJ **557**, L57 (2001).

Evans, A.; Stickel, M.; van Loon, J. T.; Eyres, S. P. S.; Hopwood, M. E. L. and Penny, A. J. Far infra-red emission from NGC 7078: First detection of intra-cluster dust in a globular cluster. A&A **408**, L9 (2003).

Evans, C. J.; Lennon, D. J.; Trundle, C.; Heap, S. R. and Lindler, D. J. Terminal Velocities of Luminous, Early-Type Stars in the Small Magellanic Cloud. ApJ **607**, 451 (2004).

Fabbiano, G.; Zezas, A. and Murray, S. S. Chandra Observations of "The Antennae" Galaxies (NGC 4038/9). ApJ **554**, 1035 (2001).

Fabjan, D.; Borgani, S.; Tornatore, L.; Saro, A.; Murante, G. and Dolag, K. Simulating the effect of active galactic nuclei feedback on the metal enrichment of galaxy clusters. MNRAS **401**, 1670 (2010).

Falocco, S.; Carrera, F. J.; Corral, A.; Laird, E.; Nandra, K.; Barcons, X.; Page, M. J. and Digby-North, J. Averaging the AGN X-ray spectra from deep Chandra fields. A&A **538**, A83 (2012).

Faulkner, D. J. and Freeman, K. C. Gas in globular clusters. I - Time-independent flow models. ApJ **211**, 77 (1977).

Faulkner, D. J.; Scott, T. R.; Wood, P. R. and Wright, A. E. Observation of neutral hydrogen in the globular cluster NGC 2808. ApJ **374**, L45 (1991).

Ferrarese, L.; Côté, P.; Dalla Bontà, E.; Peng, E. W.; Merritt, D.; Jordán, A.; Blakeslee, J. P.; Haşegan, M.; Mei, S.; Piatek, S.; Tonry, J. L. and West, M. J. A Fundamental Relation between Compact Stellar Nuclei, Supermassive Black Holes, and Their Host Galaxies. ApJ **644**, L21 (2006).

Frail, D. A. and Beasley, A. J. Stellar OH masers toward globular clusters. A&A **290**, 796 (1994).

Frank, J. and Gisler, G. The fate of gas in globular clusters. MNRAS **176**, 533 (1976).

Freire, P. C.; Camilo, F.; Kramer, M.; Lorimer, D. R.; Lyne, A. G.; Manchester, R. N. and D'Amico, N. Further results from the timing of the millisecond pulsars in 47 Tucanae. MNRAS **340**, 1359 (2003).

Freire, P. C.; Camilo, F.; Lorimer, D. R.; Lyne, A. G.; Manchester, R. N. and D'Amico, N. Timing the millisecond pulsars in 47 Tucanae. MNRAS **326**, 901 (2001a).

Freire, P. C.; Kramer, M.; Lyne, A. G.; Camilo, F.; Manchester, R. N. and D'Amico, N. Detection of Ionized Gas in the Globular Cluster 47 Tucanae. ApJ **557**, L105 (2001b).

Freire, P. C. C. The pulsar population in Globular Clusters and in the Galaxy. In *IAU Symposium* (2013), vol. 291 of *IAU Symposium*, pp. 243–250.

Fryxell, B.; Olson, K.; Ricker, P.; Timmes, F. X.; Zingale, M.; Lamb, D. Q.; MacNeice, P.; Rosner, R.; Truran, J. W. and Tufo, H. FLASH: An Adaptive Mesh Hydrodynamics Code for Modeling Astrophysical Thermonuclear Flashes. ApJS **131**, 273 (2000a).

Fryxell, B.; Olson, K.; Ricker, P.; Timmes, F. X.; Zingale, M.; Lamb, D. Q.; MacNeice, P.; Rosner, R.; Truran, J. W. and Tufo, H. FLASH: An Adaptive Mesh Hydrodynamics Code for Modeling Astrophysical Thermonuclear Flashes. ApJS **131**, 273 (2000b).

Fryxell, B.; Olson, K.; Ricker, P.; Timmes, F. X.; Zingale, M.; Lamb, D. Q.; MacNeice, P.; Rosner, R.; Truran, J. W. and Tufo, H. FLASH: An Adaptive Mesh Hydrodynamics Code for Modeling Astrophysical Thermonuclear Flashes. ApJS **131**, 273 (2000c).

Gabor, J. M. and Bournaud, F. Active galactic nuclei-driven outflows without immediate quenching in simulations of high-redshift disc galaxies. MNRAS **441**, 1615 (2014).

Gebhardt, K.; Rich, R. M. and Ho, L. C. An Intermediate-Mass Black Hole in the Globular Cluster G1: Improved Significance from New Keck and Hubble Space Telescope Observations. ApJ **634**, 1093 (2005a).

Gebhardt, K.; Rich, R. M. and Ho, L. C. An Intermediate-Mass Black Hole in the Globular Cluster G1: Improved Significance from New Keck and Hubble Space Telescope Observations. ApJ **634**, 1093 (2005b).

Gerssen, J.; van der Marel, R. P.; Gebhardt, K.; Guhathakurta, P.; Peterson, R. C. and Pryor, C. Hubble Space Telescope Evidence for an Intermediate-Mass Black Hole in the Globular Cluster M15. II. Kinematic Analysis and Dynamical Modeling. AJ **124**, 3270 (2002).

Gilbert, A. M. and Graham, J. R. Feedback in the Antennae Galaxies (NGC 4038/9). I. High-Resolution Infrared Spectroscopy of Winds from Super Star Clusters. ApJ **668**, 168 (2007a).

Gilbert, A. M. and Graham, J. R. Feedback in the Antennae Galaxies (NGC 4038/9). I. High-Resolution Infrared Spectroscopy of Winds from Super Star Clusters. ApJ **668**, 168 (2007b).

Gnat, O. and Sternberg, A. Time-dependent Ionization in Radiatively Cooling Gas. ApJS **168**, 213 (2007).

Gnedin, O. Y.; Zhao, H.; Pringle, J. E.; Fall, S. M.; Livio, M. and Meylan, G. The Unique History of the Globular Cluster ω Centauri. ApJ **568**, L23 (2002).

Goudfrooij, P.; Puzia, T. H.; Kozhurina-Platais, V. and Chandar, R. Population Parameters of Intermediate-Age Star Clusters in the Large Magellanic Cloud. I. NGC 1846 and its Wide Main-Sequence Turnoff. AJ **137**, 4988 (2009).

Graham, A. W.; Onken, C. A.; Athanassoula, E. and Combes, F. An expanded M_{bh}-σ diagram, and a new calibration of active galactic nuclei masses. MNRAS **412**, 2211 (2011).

Graham, A. W. and Spitler, L. R. Quantifying the coexistence of massive black holes and dense nuclear star clusters. MNRAS **397**, 2148 (2009).

Gratton, R.; Sneden, C. and Carretta, E. Abundance Variations Within Globular Clusters. ARA&A **42**, 385 (2004).

Gültekin, K.; Richstone, D. O.; Gebhardt, K.; Lauer, T. R.; Pinkney, J.; Aller, M. C.; Bender, R.; Dressler, A.; Faber, S. M.; Filippenko, A. V.; Green, R.; Ho, L. C.; Kormendy, J. and Siopis, C. A Quintet of Black Hole Mass Determinations. ApJ **695**, 1577 (2009a).

Gültekin, K.; Richstone, D. O.; Gebhardt, K.; Lauer, T. R.; Tremaine, S.; Aller, M. C.; Bender, R.; Dressler, A.; Faber, S. M.; Filippenko, A. V.; Green, R.; Ho, L. C.; Kormendy, J.; Magorrian, J.; Pinkney, J. and Siopis, C. The M-σ and M-L Relations in Galactic Bulges, and Determinations of Their Intrinsic Scatter. ApJ **698**, 198 (2009b).

Haehnelt, M. G. and Rees, M. J. The formation of nuclei in newly formed galaxies and the evolution of the quasar population. MNRAS **263**, 168 (1993).

Harris, W. E. Globular cluster systems in galaxies beyond the Local Group. ARA&A **29**, 543 (1991).

Harris, W. E. A Catalog of Parameters for Globular Clusters in the Milky Way. AJ **112**, 1487 (1996).

Heiles, C. and Henry, R. C. The Lack of Neutral Hydrogen in m5 and M14. ApJ **146**, 953 (1966).

Hernanz, M. and Sala, G. X-ray observations of classical novae: Theoretical implications. *Astronomische Nachrichten* **331**, 169 (2010).

Hernquist, L. An analytical model for spherical galaxies and bulges. ApJ **356**, 359 (1990).

Hirschmann, M.; Dolag, K.; Saro, A.; Borgani, S. and Burkert, A. Cosmological simulations of black hole growth: AGN luminosities and downsizing. *ArXiv e-prints* (2013).

Holzer, T. E. and Axford, W. I. The Theory of Stellar Winds and Related Flows. ARA&A **8**, 31 (1970).

Hopkins, P. F.; Hernquist, L.; Cox, T. J.; Robertson, B. and Krause, E. A Theoretical Interpretation of the Black Hole Fundamental Plane. ApJ **669**, 45 (2007).

Hopwood, M. E. L.; Evans, A.; Penny, A. and Eyres, S. P. S. Dust in the core of the metal-rich globular cluster NGC6356. MNRAS **301**, L30 (1998).

Hopwood, M. E. L.; Eyres, S. P. S.; Evans, A.; Penny, A. and Odenkirchen, M. ISO observations of globular clusters. A&A **350**, 49 (1999).

Hueyotl-Zahuantitla, F.; Tenorio-Tagle, G.; Wünsch, R.; Silich, S. and Palouš, J. On the Hydrodynamic Interplay Between a Young Nuclear Starburst and a Central Supermassive Black Hole. ApJ **716**, 324 (2010).

Hui, C. Y.; Cheng, K. S. and Taam, R. E. Diffuse X-ray Emission in Globular Cluster Cores. ApJ **700**, 1233 (2009).

Hummer, D. G. and Storey, P. J. Recombination-line intensities for hydrogenic ions. I - Case B calculations for H I and He II. MNRAS **224**, 801 (1987).

Hwang, H. S. and Lee, M. G. Galaxy Orbits for Galaxy Clusters in the Sloan Digital Sky Survey and Two Degree Field Galaxy Redshift Survey. ApJ **676**, 218 (2008).

Jeon, M.; Pawlik, A. H.; Greif, T. H.; Glover, S. C. O.; Bromm, V.; Milosavljević, M. and Klessen, R. S. The First Galaxies: Assembly with Black Hole Feedback. ApJ **754**, 34 (2012).

Johansson, P. H.; Burkert, A. and Naab, T. The Evolution of Black Hole Scaling Relations in Galaxy Mergers. ApJ **707**, L184 (2009).

Kalogera, V.; King, A. R. and Rasio, F. A. Could Black Hole X-Ray Binaries Be Detected in Globular Clusters? ApJ **601**, L171 (2004).

Karakas, A. and Lattanzio, J. C. Stellar Models and Yields of Asymptotic Giant Branch Stars. PASA **24**, 103 (2007).

Karl, S. J.; Naab, T.; Johansson, P. H.; Kotarba, H.; Boily, C. M.; Renaud, F. and Theis, C. One Moment in Time - Modeling Star Formation in the Antennae. ApJ **715**, L88 (2010).

Kennicutt, Jr., R. C. The Global Schmidt Law in Star-forming Galaxies. ApJ **498**, 541 (1998).

Kerr, F. J.; Bowers, P. F. and Knapp, G. R. A Search for HI and OH in Southern Globular Clusters. In *Bulletin of the American Astronomical Society* (1976), vol. 8 of *Bulletin of the American Astronomical Society*, p. 537.

Kerr, F. J. and Knapp, G. R. Upper Limits on the Atomic Hydrogen Abundance in 12 Globular Clusters. AJ **77**, 573 (1972).

King, A. Black Holes, Galaxy Formation, and the M_{BH}-σ Relation. ApJ **596**, L27 (2003).

Knapp, G. R.; Gunn, J. E.; Bowers, P. F. and Vasquez Poritz, J. F. Limits on Ionized Gas in Globular Clusters. ApJ **462**, 231 (1996a).

Knapp, G. R.; Gunn, J. E.; Bowers, P. F. and Vasquez Poritz, J. F. Limits on Ionized Gas in Globular Clusters. ApJ **462**, 231 (1996b).

Knapp, G. R.; Gunn, J. E.; Bowers, P. F. and Vasquez Poritz, J. F. Limits on Ionized Gas in Globular Clusters. ApJ **462**, 231 (1996c).

Knapp, G. R.; Gunn, J. E. and Connolly, A. J. Infrared Emission from Globular Clusters: Limits on Stellar Mass Loss and Interstellar Dust. ApJ **448**, 195 (1995).

Knapp, G. R. and Kerr, F. J. A search for OH/IR stars in globular clusters. AJ **78**, 458 (1973).

Knapp, G. R.; Rose, W. K. and Kerr, F. J. Neutral Hydrogen Observations of Eight Globular Clusters. ApJ **186**, 831 (1973).

Komossa, S.; Burwitz, V.; Hasinger, G.; Predehl, P.; Kaastra, J. S. and Ikebe, Y. Discovery of a Binary Active Galactic Nucleus in the Ultraluminous Infrared Galaxy NGC 6240 Using Chandra. ApJ **582**, L15 (2003).

Kormendy, J. and Richstone, D. Inward Bound—The Search For Supermassive Black Holes In Galactic Nuclei. ARA&A **33**, 581 (1995).

Koss, M.; Mushotzky, R.; Treister, E.; Veilleux, S.; Vasudevan, R. and Trippe, M. Understanding Dual Active Galactic Nucleus Activation in the nearby Universe. ApJ **746**, L22 (2012).

Kroupa, P. On the variation of the initial mass function. MNRAS **322**, 231 (2001).

Kroupa, P.; Weidner, C.; Pflamm-Altenburg, J.; Thies, I.; Dabringhausen, J.; Marks, M. and Maschberger, T. *The Stellar and Sub-Stellar Initial Mass Function of Simple and Composite Populations*, p. 115 (2013a).

Kroupa, P.; Weidner, C.; Pflamm-Altenburg, J.; Thies, I.; Dabringhausen, J.; Marks, M. and Maschberger, T. *The Stellar and Sub-Stellar Initial Mass Function of Simple and Composite Populations*, p. 115 (2013b).

Kurosawa, R.; Proga, D. and Nagamine, K. On the Feedback Efficiency of Active Galactic Nuclei. ApJ **707**, 823 (2009).

Laor, A. Optical, UV, and X-ray clues to the nature of narrow-line AGNs. New A Rev. **44**, 503 (2000).

Leon, S. and Combes, F. Search for CO emission in globular clusters. A&A **309**, 123 (1996).

Li, L.-X. Accretion, growth of supermassive black holes, and feedback in galaxy mergers. MNRAS **424**, 1461 (2012).

Lin, D. N. C. and Murray, S. D. Gas Accretion by Globular Clusters and Nucleated Dwarf Galaxies and the Formation of the Arches and Quintuplet Clusters. ApJ **661**, 779 (2007).

Liu, X.; Civano, F.; Shen, Y.; Green, P.; Greene, J. E. and Strauss, M. A. Chandra X-Ray and Hubble Space Telescope Imaging of Optically Selected Kiloparsec-scale Binary Active Galactic Nuclei. I. Nature of the Nuclear Ionizing Sources. ApJ **762**, 110 (2013).

Lorimer, D. R.; Camilo, F.; Freire, P.; Kramer, M.; Lyne, A. G.; Manchester, R. N. and D'Amico, N. Millisecond Radio Pulsars in 47 Tucanae. In Bailes, M.; Nice, D. J. and Thorsett, S. E., eds., *Radio Pulsars* (2003), vol. 302 of *Astronomical Society of the Pacific Conference Series*, p. 363.

Loup, C.; Forveille, T.; Omont, A. and Paul, J. F. CO and HCN observations of circumstellar envelopes. A catalogue - Mass loss rates and distributions. A&AS **99**, 291 (1993).

Lynch, D. K.; Bowers, P. F. and Whiteoak, J. B. A deep search for 21 CM neutral hydrogen emission in the tightly bound globular cluster NGC 6388. AJ **97**, 1708 (1989).

Lynch, D. K. and Rossano, G. S. An IRAS search for dust in globular clusters. AJ **100**, 719 (1990).

Maccarone, T. J.; Kundu, A.; Zepf, S. E. and Rhode, K. L. A black hole in a globular cluster. Nature **445**, 183 (2007).

Mackey, A. D.; Broby Nielsen, P.; Ferguson, A. M. N. and Richardson, J. C. Multiple Stellar Populations in Three Rich Large Magellanic Cloud Star Clusters. ApJ **681**, L17 (2008).

Magorrian, J.; Tremaine, S.; Richstone, D.; Bender, R.; Bower, G.; Dressler, A.; Faber, S. M.; Gebhardt, K.; Green, R.; Grillmair, C.; Kormendy, J. and Lauer, T. The Demography of Massive Dark Objects in Galaxy Centers. AJ **115**, 2285 (1998a).

Magorrian, J.; Tremaine, S.; Richstone, D.; Bender, R.; Bower, G.; Dressler, A.; Faber, S. M.; Gebhardt, K.; Green, R.; Grillmair, C.; Kormendy, J. and Lauer, T. The Demography of Massive Dark Objects in Galaxy Centers. AJ **115**, 2285 (1998b).

Manchester, R. N.; Hobbs, G. B.; Teoh, A. and Hobbs, M. ATNF Pulsar Catalog (Manchester+, 2005). *VizieR Online Data Catalog* **7245**, 0 (2005).

Manchester, R. N.; Lyne, A. G.; Johnston, S.; D'Amico, N.; Lim, J. and Kniffen, D. A. A 5.75-millisecond pulsar in the globular cluster 47 Tucanae. Nature **345**, 598 (1990).

Manchester, R. N.; Lyne, A. G.; Robinson, C.; Bailes, M. and D'Amico, N. Discovery of ten millisecond pulsars in the globular cluster 47 Tucanae. Nature **352**, 219 (1991).

Marcolini, A.; D'Ercole, A.; Brighenti, F. and Recchi, S. Star formation feedback and metal enrichment by Types Ia and II supernovae in dwarf spheroidal galaxies: the case of Draco. MNRAS **371**, 643 (2006).

Marigo, P. Asymptotic giant branch evolution: Where do we stand? In *IAU Symposium* (2012a), vol. 283 of *IAU Symposium*, pp. 87–94.

Marigo, P. Asymptotic giant branch evolution: Where do we stand? In *IAU Symposium* (2012b), vol. 283 of *IAU Symposium*, pp. 87–94.

Markevitch, M. Chandra Observation of the Most Interesting Cluster in the Universe. In Wilson, A., ed., *The X-ray Universe 2005* (2006), vol. 604 of *ESA Special Publication*, p. 723.

Markevitch, M.; Gonzalez, A. H.; David, L.; Vikhlinin, A.; Murray, S.; Forman, W.; Jones, C. and Tucker, W. A Textbook Example of a Bow Shock in the Merging Galaxy Cluster 1E 0657-56. ApJ **567**, L27 (2002).

Marks, M. and Kroupa, P. Initial conditions for globular clusters and assembly of the old globular cluster population of the Milky Way. MNRAS **406**, 2000 (2010).

Marshall, J. R.; van Loon, J. T.; Matsuura, M.; Wood, P. R.; Zijlstra, A. A. and Whitelock, P. A. Asymptotic giant branch superwind speed at low metallicity. MNRAS **355**, 1348 (2004).

Martell, S. L. and Smith, G. H. CN Variations in High-Metallicity Globular and Open Clusters. PASP **121**, 577 (2009).

Mateo, M. L. Dwarf Galaxies of the Local Group. ARA&A **36**, 435 (1998).

McClintock, J. E. and Remillard, R. A. *Black hole binaries*, Compact stellar X-ray sources, pp. 157–213 (2006).

McCrady, N. and Graham, J. R. Super Star Cluster Velocity Dispersions and Virial Masses in the M82 Nuclear Starburst. ApJ **663**, 844 (2007).

McDonald, I. and van Loon, J. T. Dust, pulsation, chromospheres and their rôle in driving mass loss from red giants in Galactic globular clusters. A&A **476**, 1261 (2007).

McNamara, B. J.; Harrison, T. E. and Baumgardt, H. The Dynamical Distance to M15: Estimates of the Cluster's Age and Mass and of the Absolute Magnitude of Its RR Lyrae Stars. ApJ **602**, 264 (2004).

Menou, K.; Esin, A. A.; Narayan, R.; Garcia, M. R.; Lasota, J.-P. and McClintock, J. E. Black Hole and Neutron Star Transients in Quiescence. ApJ **520**, 276 (1999).

Mestel, L. On the theory of white dwarf stars. I. The energy sources of white dwarfs. MNRAS **112**, 583 (1952).

Miller, J. M.; Fabian, A. C. and Lewin, W. H. G. The XMM-Newton Spectrum of 4U 1543-475 in the Low/Hard State and a Comment on Accretion Flow Constraints in this Regime. *The Astronomer's Telegram* **212**, 1 (2003).

Milosavljević, M.; Koda, J.; Nagai, D.; Nakar, E. and Shapiro, P. R. The Cluster-Merger Shock in 1E 0657-56: Faster than a Speeding Bullet? ApJ **661**, L131 (2007).

Mirabal, N. A curious source of extended X-ray emission in the outskirts of globular cluster GLIMPSE-C01. MNRAS **402**, 1391 (2010).

Moore, K. and Bildsten, L. Clearing the Gas from Globular Clusters and Dwarf Spheroidals with Classical Novae. ApJ **728**, 81 (2011).

Morin, J.; Donati, J.-F.; Petit, P.; Delfosse, X.; Forveille, T.; Albert, L.; Aurière, M.; Cabanac, R.; Dintrans, B.; Fares, R.; Gastine, T.; Jardine, M. M.; Lignières, F.; Paletou, F.; Ramirez Velez, J. C. and Théado, S. Large-scale magnetic topologies of mid M dwarfs. MNRAS **390**, 567 (2008).

Naiman, J. P.; Ramirez-Ruiz, E. and Lin, D. N. C. Gas Accretion by Star Clusters and the Formation of Ultraluminous X-Ray Sources from Cusps of Compact Remnants. ApJ **705**, L153 (2009).

Naiman, J. P.; Ramirez-Ruiz, E. and Lin, D. N. C. External Mass Accumulation onto Core Potentials: Implications for Star Clusters, Galaxies, and Galaxy Clusters. ApJ **735**, 25 (2011).

Neumayer, N. Nuclear Star Clusters - Structure and Stellar Populations. *ArXiv e-prints* (2012).

Newton, R. D. A. and Kay, S. T. A study of AGN and supernova feedback in simulations of isolated and merging disc galaxies. MNRAS **434**, 3606 (2013).

Nomoto, K.; Saio, H.; Kato, M. and Hachisu, I. Thermal Stability of White Dwarfs Accreting Hydrogen-rich Matter and Progenitors of Type Ia Supernovae. ApJ **663**, 1269 (2007).

Noyola, E.; Gebhardt, K. and Bergmann, M. Gemini and Hubble Space Telescope Evidence for an Intermediate-Mass Black Hole in ω Centauri. ApJ **676**, 1008 (2008).

Nyman, L.-A.; Booth, R. S.; Carlstrom, U.; Habing, H. J.; Heske, A.; Sahai, R.; Stark, R.; van der Veen, W. E. J. C. and Winnberg, A. A survey of circumstellar CO emission from a sample of IRAS point sources. A&AS **93**, 121 (1992).

O'Brien, T. J.; Bode, M. F.; Porcas, R. W.; Muxlow, T. W. B.; Eyres, S. P. S.; Beswick, R. J.; Garrington, S. T.; Davis, R. J. and Evans, A. An asymmetric shock wave in the 2006 outburst of the recurrent nova RS Ophiuchi. Nature **442**, 279 (2006).

Odenkirchen, M.; Brosche, P.; Geffert, M. and Tucholke, H.-J. Globular cluster orbits based on Hipparcos proper motions. New A **2**, 477 (1997).

Origlia, L.; Ferraro, F. R. and Pecci, F. F. Mid-infrared properties of globular clusters using the IRAS data base. MNRAS **280**, 572 (1996).

Origlia, L.; Gredel, R.; Ferraro, F. R. and Fusi Pecci, F. CO mapping of the central regions of the globular clusters omicronCen and 47Tuc. MNRAS **289**, 948 (1997).

Padmanabhan, T. *Theoretical Astrophysics - Volume 1, Astrophysical Processes* (2000).

Paxton, B.; Bildsten, L.; Dotter, A.; Herwig, F.; Lesaffre, P. and Timmes, F. Modules for Experiments in Stellar Astrophysics (MESA). ApJS **192**, 3 (2011).

Peres, G.; Serio, S.; Vaiana, G. S. and Rosner, R. Coronal closed structures. IV - Hydrodynamical stability and response to heating perturbations. ApJ **252**, 791 (1982).

Pfahl, E. and Rappaport, S. Bondi-Hoyle-Lyttleton Accretion Model for Low-Luminosity X-Ray Sources in Globular Clusters. ApJ **550**, 172 (2001a).

Pfahl, E. and Rappaport, S. Bondi-Hoyle-Lyttleton Accretion Model for Low-Luminosity X-Ray Sources in Globular Clusters. ApJ **550**, 172 (2001b).

Pflamm-Altenburg, J. and Kroupa, P. Recurrent gas accretion by massive star clusters, multiple stellar populations and mass thresholds for spheroidal stellar systems. MNRAS **397**, 488 (2009).

Piotto, G. Observations of multiple populations in star clusters. In Mamajek, E. E.; Soderblom, D. R. and Wyse, R. F. G., eds., *IAU Symposium* (2009a), vol. 258 of *IAU Symposium*, pp. 233–244.

Piotto, G. Observations of multiple populations in star clusters. In Mamajek, E. E.; Soderblom, D. R. and Wyse, R. F. G., eds., *IAU Symposium* (2009b), vol. 258 of *IAU Symposium*, pp. 233–244.

Plummer, H. C. On the problem of distribution in globular star clusters. MNRAS **71**, 460 (1911).

Pooley, D. and Rappaport, S. X-Rays from the Globular Cluster G1: Intermediate-Mass Black Hole or Low-Mass X-Ray Binary? ApJ **644**, L45 (2006).

Priestley, W.; Ruffert, M. and Salaris, M. On the evolution of intracluster gas within Galactic globular clusters. MNRAS **411**, 1935 (2011).

Primack, J. R.; Gilmore, R. C. and Somerville, R. S. Diffuse Extragalactic Background Radiation. In Aharonian, F. A.; Hofmann, W. and Rieger, F., eds., *American Institute of Physics Conference Series* (2008), vol. 1085 of *American Institute of Physics Conference Series*, pp. 71–82.

Quataert, E. A Dynamical Model for Hot Gas in the Galactic Center. ApJ **613**, 322 (2004).

Reimers, D. Circumstellar absorption lines and mass loss from red giants. *Memoires of the Societe Royale des Sciences de Liege* **8**, 369 (1975).

Renzini, A. and Voli, M. Advanced evolutionary stages of intermediate-mass stars. I - Evolution of surface compositions. A&A **94**, 175 (1981).

Robaina, A. R.; Bell, E. F.; van der Wel, A.; Somerville, R. S.; Skelton, R. E.; McIntosh, D. H.; Meisenheimer, K. and Wolf, C. The Merger-driven Evolution of Massive Galaxies. ApJ **719**, 844 (2010).

Robinson, B. J. Limits to the Neutral Hydrogen Content of ω Centauri and 47 Tucanae. Astrophys. Lett. **1**, 21 (1967).

Robinson, C.; Lyne, A. G.; Manchester, R. N.; Bailes, M.; D'Amico, N. and Johnston, S. Millisecond pulsars in the globular cluster 47 Tucanae. MNRAS **274**, 547 (1995).

Rosner, R.; Tucker, W. H. and Vaiana, G. S. Dynamics of the quiescent solar corona. ApJ **220**, 643 (1978).

Ruffert, M. Three-dimensional hydrodynamic Bondi-Hoyle accretion. 1: Code validation and stationary accretors. ApJ **427**, 342 (1994a).

Ruffert, M. Three-dimensional hydrodynamic Bondi-Hoyle accretion. III. Mach 0.6, 1.4 and 10; γ=5/3. A&AS **106**, 505 (1994b).

Ruffert, M. and Arnett, D. Three-dimensional hydrodynamic Bondi-Hoyle accretion. 2: Homogeneous medium at Mach 3 with gamma = 5/3. ApJ **427**, 351 (1994).

Sawala, T.; Guo, Q.; Scannapieco, C.; Jenkins, A. and White, S. What is the (dark) matter with dwarf galaxies? MNRAS **413**, 659 (2011).

Schaerer, D.; de Koter, A.; Schmutz, W. and Maeder, A. Combined stellar structure and atmosphere models for massive stars. I. Interior evolution and wind properties on the main sequence. A&A **310**, 837 (1996).

Scott, E. H. and Durisen, R. H. Nova-driven winds in globular clusters. ApJ **222**, 612 (1978).

Scott, N.; Cappellari, M.; Davies, R. L.; Bacon, R.; de Zeeuw, P. T.; Emsellem, E.; Falcón-Barroso, J.; Krajnović, D.; Kuntschner, H.; McDermid, R. M.; Peletier, R. F.; Pipino, A.; Sarzi, M.; van den Bosch, R. C. E.; van de Ven, G. and van Scherpenzeel, E. The SAURON

Project - XIV. No escape from V_{esc}: a global and local parameter in early-type galaxy evolution. MNRAS **398**, 1835 (2009).

Searle, S. C.; Prinja, R. K.; Massa, D. and Ryans, R. Quantitative studies of the optical and UV spectra of Galactic early B supergiants. I. Fundamental parameters. A&A **481**, 777 (2008).

Seth, A.; Cappellari, M.; Neumayer, N.; Caldwell, N.; Bastian, N.; Olsen, K.; Blum, R.; Debattista, V. P.; McDermid, R.; Puzia, T. and Stephens, A. Nuclear Star Clusters & Black Holes. In Debattista, V. P. and Popescu, C. C., eds., *American Institute of Physics Conference Series* (2010), vol. 1240 of *American Institute of Physics Conference Series*, pp. 227–230.

Shankar, F. The demography of supermassive black holes: Growing monsters at the heart of galaxies. New A Rev. **53**, 57 (2009).

Sijacki, D.; Springel, V.; Di Matteo, T. and Hernquist, L. A unified model for AGN feedback in cosmological simulations of structure formation. MNRAS **380**, 877 (2007).

Silk, J. and Rees, M. J. Quasars and galaxy formation. A&A **331**, L1 (1998).

Sloan, G. C.; Kraemer, K. E.; Wood, P. R.; Zijlstra, A. A.; Bernard-Salas, J.; Devost, D. and Houck, J. R. The Magellanic Zoo: Mid-Infrared Spitzer Spectroscopy of Evolved Stars and Circumstellar Dust in the Magellanic Clouds. ApJ **686**, 1056 (2008).

Smith, G. H. The chemical inhomogeneity of globular clusters. PASP **99**, 67 (1987).

Smith, G. H. Globular Cluster Winds Driven by Main-Sequence Stars. PASP **111**, 980 (1999).

Smith, G. H.; Dupree, A. K. and Strader, J. He I λ10830 Absorption in Metal-Poor Red Giants: Probing Fast Chromospheric Outflows. PASP **116**, 819 (2004).

Smith, G. H.; Wood, P. R.; Faulkner, D. J. and Wright, A. E. Parkes H I observations of southern globular clusters - Implications for stellar mass loss. ApJ **353**, 168 (1990).

Smith, G. H.; Woodsworth, A. W. and Hesser, J. E. A search for CO(2-1) emission from the globular cluster M15. MNRAS **273**, 632 (1995a).

Smith, G. H.; Woodsworth, A. W. and Hesser, J. E. A search for CO(2-1) emission from the globular cluster M15. MNRAS **273**, 632 (1995b).

Smith, M. G.; Hesser, J. E. and Shawl, S. J. An optical search for ionized hydrogen in globular clusters. ApJ **206**, 66 (1976).

Spergel, D. N. Evacuation of gas from globular clusters by winds from millisecond pulsars. Nature **352**, 221 (1991).

Springel, V.; Di Matteo, T. and Hernquist, L. Modelling feedback from stars and black holes in galaxy mergers. MNRAS **361**, 776 (2005).

Starrfield, S.; Sparks, W. M. and Truran, J. W. Recurrent novae as a consequence of the accretion of solar material onto a 1.38 solar mass white dwarf. ApJ **291**, 136 (1985).

Tayler, R. J. and Wood, P. R. The gas and horizontal branch star content of globular clusters. MNRAS **171**, 467 (1975).

Tremaine, S.; Gebhardt, K.; Bender, R.; Bower, G.; Dressler, A.; Faber, S. M.; Filippenko, A. V.; Green, R.; Grillmair, C.; Ho, L. C.; Kormendy, J.; Lauer, T. R.; Magorrian, J.; Pinkney, J. and Richstone, D. The Slope of the Black Hole Mass versus Velocity Dispersion Correlation. ApJ **574**, 740 (2002).

Trinchieri, G.; Wolter, A. and Crivellari, E. The ULX Population in the Cartwheel Galaxy. In Bandyopadhyay, R. M.; Wachter, S.; Gelino, D. and Gelino, C. R., eds., *A Population Explosion: The Nature & Evolution of X-ray Binaries in Diverse Environments* (2008), vol. 1010 of *American Institute of Physics Conference Series*, pp. 357–359.

Troland, T. H.; Hesser, J. E. and Heiles, C. An unsuccessful search for carbon monoxide in globular clusters. ApJ **219**, 873 (1978).

Truelove, J. K.; Klein, R. I.; McKee, C. F.; Holliman, II, J. H.; Howell, L. H. and Greenough, J. A. The Jeans Condition: A New Constraint on Spatial Resolution in Simulations of Isothermal Self-gravitational Hydrodynamics. ApJ **489**, L179 (1997).

Ulvestad, J. S.; Greene, J. E. and Ho, L. C. Radio Emission from the Intermediate-Mass Black Hole in the Globular Cluster G1. ApJ **661**, L151 (2007a).

Ulvestad, J. S.; Greene, J. E. and Ho, L. C. Radio Emission from the Intermediate-Mass Black Hole in the Globular Cluster G1. ApJ **661**, L151 (2007b).

Umbreit, S.; Chatterjee, S. and Rasio, F. A. Clearing the Dust from Globular Clusters. ApJ **680**, L113 (2008).

van Loon, J. T.; Stanimirović, S.; Evans, A. and Muller, E. Stellar mass loss and the intracluster medium in Galactic globular clusters: a deep radio survey for HI and OH. MNRAS **365**, 1277 (2006).

van Loon, J. T.; Stanimirović, S.; Putman, M. E.; Peek, J. E. G.; Gibson, S. J.; Douglas, K. A. and Korpela, E. J. A peculiar HI cloud near the distant globular cluster Pal4. MNRAS **396**, 1096 (2009).

Vandenberg, D. A. and Faulkner, D. J. Gas in globular clusters. II - Time-dependent flow models. ApJ **218**, 415 (1977).

Vassiliadis, E. and Wood, P. R. Evolution of low- and intermediate-mass stars to the end of the asymptotic giant branch with mass loss. ApJ **413**, 641 (1993).

Ventura, P. and D'Antona, F. The self-enrichment scenario in intermediate metallicity globular clusters. A&A **479**, 805 (2008).

Ventura, P.; D'Antona, F. and Mazzitelli, I. Lithium and mass loss in massive AGB stars in the Large Magellanic Cloud. A&A **363**, 605 (2000).

Vesperini, E.; McMillan, S. L. W.; D'Antona, F. and D'Ercole, A. The Fraction of Globular Cluster Second-generation Stars in the Galactic Halo. ApJ **718**, L112 (2010).

Walcher, C. J.; van der Marel, R. P.; McLaughlin, D.; Rix, H.-W.; Böker, T.; Häring, N.; Ho, L. C.; Sarzi, M. and Shields, J. C. Masses of Star Clusters in the Nuclei of Bulgeless Spiral Galaxies. ApJ **618**, 237 (2005).

Waters, L. B. F. M.; Cote, J. and Lamers, H. J. G. L. M. IRAS observations of Be stars. II - Far-IR characteristics and mass loss rates. A&A **185**, 206 (1987).

Whitmore, B. C.; Gilmore, D.; Leitherer, C.; Fall, S. M.; Chandar, R.; Blair, W. P.; Schweizer, F.; Zhang, Q. and Miller, B. W. Space Telescope Imaging Spectrograph Observations of Young Star Clusters in the Antennae Galaxies (NGC 4038/4039). AJ **130**, 2104 (2005).

Whitmore, B. C.; Zhang, Q.; Leitherer, C.; Fall, S. M.; Schweizer, F. and Miller, B. W. The Luminosity Function of Young Star Clusters in "the Antennae" Galaxies (NGC 4038-4039). AJ **118**, 1551 (1999a).

Whitmore, B. C.; Zhang, Q.; Leitherer, C.; Fall, S. M.; Schweizer, F. and Miller, B. W. The Luminosity Function of Young Star Clusters in "the Antennae" Galaxies (NGC 4038-4039). AJ **118**, 1551 (1999b).

Wilkin, F. P. Exact Analytic Solutions for Stellar Wind Bow Shocks. ApJ **459**, L31 (1996).

Wolfson, R. Axisymmetric accretion near compact objects. ApJ **213**, 200 (1977).

Wood, B. E.; Müller, H.-R.; Zank, G. P.; Linsky, J. L. and Redfield, S. New Mass-Loss Measurements from Astrospheric Lyα Absorption. ApJ **628**, L143 (2005).

Zezas, A.; Fabbiano, G.; Baldi, A.; Schweizer, F.; King, A. R.; Ponman, T. J. and Rots, A. H. Chandra Monitoring Observations of The Antennae Galaxies. I. Catalog of Source Properties. ApJS **166**, 211 (2006).

Zezas, A.; Fabbiano, G.; Baldi, A.; Schweizer, F.; King, A. R.; Rots, A. H. and Ponman, T. J. Chandra Monitoring Observations of the Antennae Galaxies. II. X-Ray Luminosity Functions. ApJ **661**, 135 (2007).

Zezas, A.; Fabbiano, G.; Rots, A. H. and Murray, S. S. Chandra Observations of "The Antennae" Galaxies (NGC 4038/4039). III. X-Ray Properties and Multiwavelength Associations of the X-Ray Source Population. ApJ **577**, 710 (2002).

Zhang, Q. and Fall, S. M. The Mass Function of Young Star Clusters in the "Antennae" Galaxies. In *Bulletin of the American Astronomical Society* (1999), vol. 31 of *Bulletin of the American Astronomical Society*, pp. 1443–+.

Zhu, M.; Seaquist, E. R. and Kuno, N. A Multitransition CO Study of the Antennae Galaxies NGC 4038/9. ApJ **588**, 243 (2003a).

Zhu, M.; Seaquist, E. R. and Kuno, N. A Multitransition CO Study of the Antennae Galaxies NGC 4038/9. ApJ **588**, 243 (2003b).